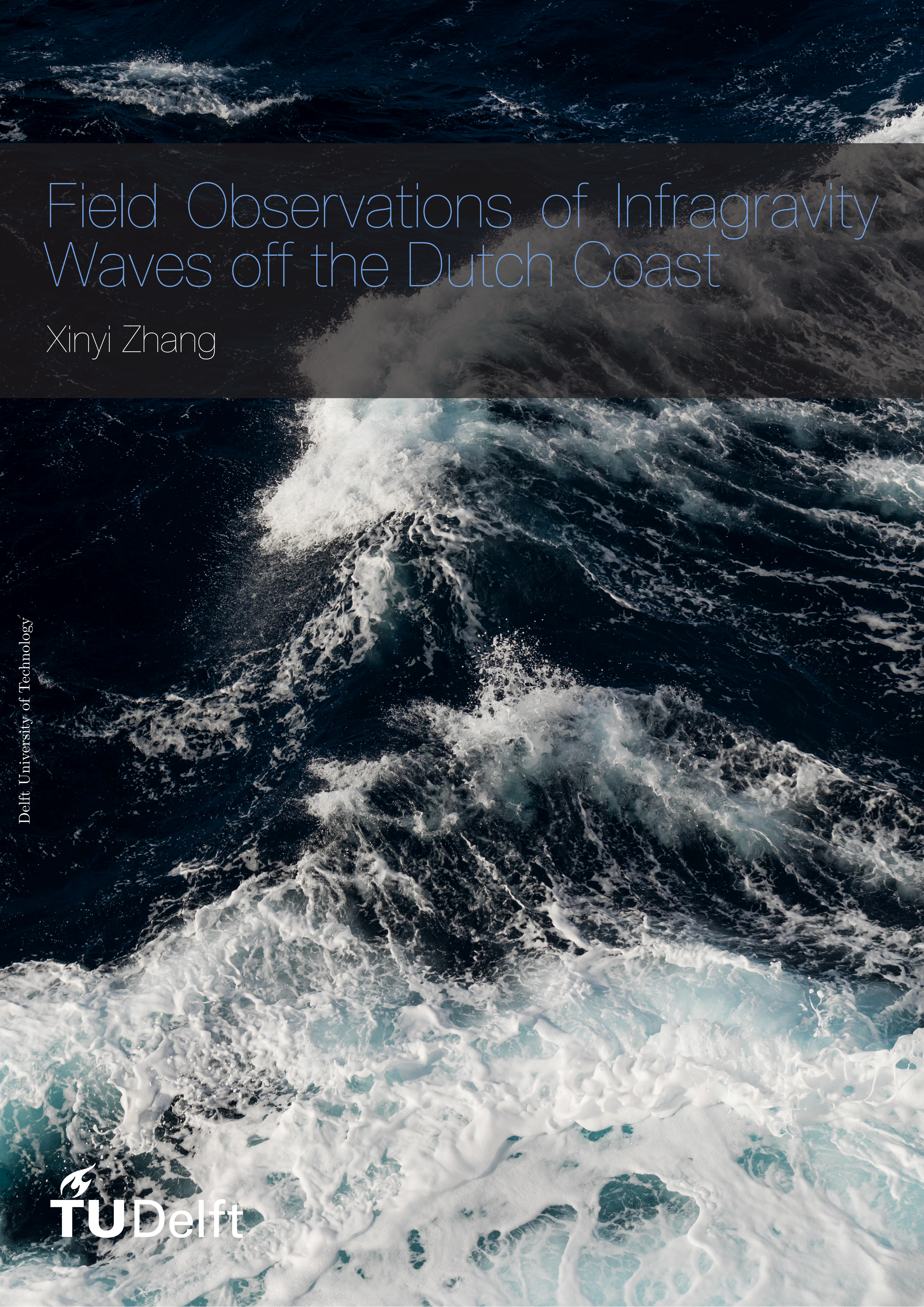

Field Observations of Infragravity Waves off the Dutch Coast

Xinyi Zhang

Delft University of Technology

Field Observations of Infragravity Waves off the Dutch Coast

by

Xinyi Zhang

November 2022

to obtain the degree of Master of Science
at the Delft University of Technology

Supervisors:	Dr. M. F. S. Tissier (Chair)	Delft University of Technology
	Dr. ir. J. Rutten (Daily supervisor)	Delft University of Technology
	Prof. dr. ir. A. J. H. M. Reniers	Delft University of Technology
	Dr. ir. S. de Vries	Delft University of Technology

Xinyi Zhang: Field Observations of Infragravity Waves off the Dutch Coast (2022)

Student Number: 5217903

An electronic version of this thesis is available at `https://repository.tudelft.nl`.

Acknowledgments

This thesis is the final part of my two-year's study to obtain a Master of Science degree at TU Delft. The research about ocean waves, and specifically the dynamics of infragravity waves, has always attracted me. Therefore, I feel lucky that my thesis topic falls within my interest, and it was my pleasure to work under the supervision of my graduation committee: Marion, Jantien, Ad, and Sierd.

First, I would like to thank Marion for providing the opportunity for me to analyze the newly collected field data of the REFLEX project. We spent lots of time together discussing my progress. Her wisdom, passion, and kindness made our meetings fun and creative, her detailed advice on my draft also helped me to write a clearer and more informative thesis. It was a true honor for me to work with Marion, I can hardly imagine a more supportive supervisor. Next, I would like to thank Jantien for her guidance, especially at the early stages of this study. The pre-processing work on the raw field data would be a lot harder with her help. I will never forget her patience and clear mind during our meetings, after which I could always go home with lots of solved questions and a clearer perspective. Of course, the advice and support from Ad and Sierd were valuable and essential. Many thanks to Ad for his guidance during our progress meetings, his expertise helped me find the core issues of my ongoing work. Many thanks to Sierd for his enthusiasm and creativity, which encouraged me and helped me present my results more easily.

Apart from my graduation committee, I would like to express my deep gratitude to Dr. Yoshinao Matsuba. The directional properties of infragravity waves, probably the most exciting part of this thesis, were investigated with his guidance. I admire his kindness and effectiveness in our communication. He shared many insightful ideas on directional spectra reconstruction during our discussions, and without applying his newly developed method on infragravity wave spectra reconstruction, this thesis would be no doubt less fruitful. I also want to thank Dr. ir. Dirk P. Rijnsdorp, for sharing the data from the ECMWF ERA5 re-analysis, which allowed me to check the short wave height distribution over the North Sea.

Finally, my utmost gratitude goes to my mother. Without her support throughout these years, both financially and mentally, I would not be able to start my study at TU Delft in the beginning.

Xinyi Zhang
Rotterdam, November 2022

Abstract

Infragravity (IG) waves (0.005-0.04 Hz) are surface waves that can dominate the nearshore hydrodynamics and can impact various coastal processes (e.g., run-up, overwash). A proper offshore description of incident IG waves is required for storm impact models, which generally assume a local equilibrium between sea-swell (SS) waves (0.04-0.33 Hz) and the resultant nonlinearly excited bound IG waves. The contribution of free incident IG waves and the directional properties of the IG wave field are neglected, though they play a critical role in IG wave variations. Various research focuses on IG wave dynamics in shallow waters, but a detailed understanding of IG wave variability in intermediate water depth is lacking. Furthermore, the directional spectra of bound and free IG waves in the field are usually unavailable since bound IG waves do not follow linear dispersion relations, which is assumed by commonly applied directional spectra reconstruction methods.

In-situ observation data (surface elevation, pressure, and velocity) of IG waves from November 2021 to April 2022 at three cross-shore locations in intermediate water depth ($\sim 6 - 14$ m) off the Dutch coast are analyzed to study generation, propagation, and directional properties of IG waves. The bispectral technique is applied to quantify the contribution of bound IG waves to the total IG wave field. A newly developed method is validated and used upon the offshore ($\sim$ 14 m) data to reconstruct directional spectra of bound and free IG waves separately during storms.

The results show that IG wave heights are best predicted (correlation coefficient R^2 up to 0.94) with an offshore forcing parameter that includes peak period $H_{SS}T_p^2$, which indicates SS wave energy flux. The growth rate of IG waves is in between the shallow water equilibrium solution (for bound waves) and Green's Law (for free waves), indicating the total IG wave field consists of bound and free components. The relative contribution of bound IG energy (up to 76%) is correlated to SS wave energy, whereas it decreases dramatically during intense storms when SS waves break. The bound IG waves that are assumed to follow the weakly nonlinear wave theory, have a similar peak direction and broader directional spreading to SS waves. In contrast, the directional spectra of free IG waves are nearly isotropic during calm conditions, but may have diverse peaks during storms, which incident IG waves from remote sources and edge waves can influence. A better understanding of the complex pattern of free IG waves requires more detailed observations and/ or modeling.

Contents

List of Figures

List of Tables

1 Introduction

1.1 Background

Infragravity (IG) waves are surface gravity waves with frequencies typically ranging between 0.005 to 0.05Hz. Since first observed in the field (Munk, 1949), the mechanism of generation, propagation and transformation of IG waves has drawn increasing attention in recent years (Bertin et al., 2018).

Though IG waves in the deep ocean are often in the order of several millimeters (Webb et al., 1991), the IG wave height may increase drastically, even to more than a meter, close to the shoreline (e.g., Fiedler et al., 2015; Matsuba et al., 2020). Since sea-swell (SS) waves (nominally 0.06-0.3Hz) would break and dissipate much in the surf zone, IG waves may dominate coastal zones. As a result, IG waves can play an essential role in various fields. For example, Ardhuin et al. (2014) highlighted that the IG waves could affect altimetry measurements. Van Dongeren et al. (2016) reviewed IG wave dynamics over reef systems and identified its importance in the operations in ports located behind reefs. IG waves are also shown to be influential on run-up and overwash (e.g., Lashley et al., 2019) and moored vessel motions (e.g., Waals, 2009).

1.2 Motivations

The motivation for this research is twofold. First, the cross-shore IG dynamics at intermediate water depth need more investigation. Second, in order to predict IG wave effects in nearshore areas, the knowledge of offshore IG directional wave fields should be improved.

1.2.1 IG Wave Dynamics at Intermediate Depth

Different explanations of IG wave generation exist. Predominantly, IG waves in the nearshore zone can be generated by incident bound waves (Longuet-Higgins and Stewart, 1962), or by time-variation of the breakpoint (Symonds et al., 1982). Both mechanisms are linked to the short-wave modulation on the wave group scale.

Longuet-Higgins and Stewart (1962) showed that nonlinear interaction between two primary short wave components excites a forced secondary wave component, whose frequency is the difference of the two primary waves. This forced wave is referred as a bound wave, which is in anti-phase with its forcing short wave group. Bound IG waves may be released and reflected at the shoreline in the surf zone. These waves may be subsequently trapped in the nearshore due to refraction or propagate towards the deeper sea.

Bound IG wave spectra can be estimated from incident SS wave field following Hasselmann (1962) and the coupling between SS waves and bound IG waves has been identified in various field observations (e.g., Elgar et al., 1992; Herbers et al., 1994). However, the nearshore IG wave field is a mixture of bound and free IG waves, and the estimated bound IG energy only contributes an insignificant part to total IG wave energy except for very energetic wave conditions (Sand, 1982). In contrast, free IG waves dominate the total IG wave field mostly. The origin of free IG waves is complex, they can be released from bound IG waves (Longuet-Higgins and Stewart, 1962), generated through the breakpoint mechanism (Symonds et al., 1982), or arrived from remote sources (e.g., Rijnsdorp et al., 2021).

Moreover, IG waves may experience various processes during propagation towards the coastline, including dissipation, reflection, and refraction. As a result, IG waves may transfer energy within the IG frequencies or with the short wave frequency band (e.g., De Bakker et al., 2015).

The complex nature of IG wave propagation and transformation complicates the study of nearshore IG wave dynamics, and motivates the observation of cross-shore spatial and temporal variation of IG waves. However, numerous studies focused on IG wave propagation in shallow waters, where intense short wave breaking occurs. The observations in intermediate depth waters are still limited. A more detailed understanding of IG wave variability in intermediate water depth may provide insights into the study of the generation and propagation of the IG waves.

1.2.2 IG Wave Dynamics at Offshore Boundary

Accurately predicting coastal IG wave fields can be challenging since no exact analytical solution exists. Alternatively, the impact of incident IG wave dynamics may be reproduced using numerical modeling techniques. To do this, an offshore boundary condition that describes the incident IG waves should be specified. This boundary condition is generally determined with a local equilibrium between bound IG waves and SS waves (Hasselmann, 1962).

However, this approach could be inappropriate since the equilibrium solution only considers incident bound waves, while incident free IG waves may arrive from another coast (e.g., Rijnsdorp et al., 2021). In addition, the equilibrium assumes uniform water depth, hence its validity is impaired when waves propagate over sloping beaches. Therefore, the equilibrium solution may underestimate or overestimate the incident IG waves, depending on coastal configurations, as pointed out in Reniers et al. (2021).

Furthermore, the directional properties of free IG waves are important when determining shoreward or seaward propagating wave components (e.g., Elgar et al., 1994), indicating the presence of edge waves (e.g., Reniers et al., 2010), and calculating IG runup (e.g., Guza and Feddersen, 2012). Omitting the directionality of IG waves in a numerical model may undermine its accuracy (e.g., Fiedler et al., 2018). To conclude, a better understanding of the IG wave field at offshore wave field is desired.

1.3 Research Project Outline

This study investigates cross-shore propagation and directional properties of IG waves in intermediate depth. In order to do this, field data collected from three Acoustic Doppler Current Profilers (ADCPs) and one Acoustic Doppler Velocimeter (ADV) implemented in intermediate depth (6.5m, 8.5m, 13.9m water depth, respectively) in the North Sea are analyzed. This project contributes to the study of IG wave dynamics in intermediate water depth and provides insights into coastal protection.

A literature review on IG waves is in Chapter 2. The research objectives and research questions are shown in Chapter 3. Chapter 4 describes the relevant methodology for this study, and Chapter 5 shows the research results, followed by several discussion points in Chapter 6. Finally, conclusions and recommendations for future research are given in Chapter 7.

2 Literature Review

2.1 Generation Mechanism of IG waves

Various mechanisms are responsible for IG wave generation. In nearshore zone, IG waves can be generated by incident bound waves (Longuet-Higgins and Stewart, 1962), depth variation (Molin, 1982), or breakpoint variation (Symonds et al., 1982). IG waves may also be initiated due to wind gusts (Vrećica et al., 2019) in deep water.

2.1.1 Bound Wave

Longuet-Higgins and Stewart (1962) found that a short wave group may force a secondary wave with a similar frequency. As Longuet-Higgins and Stewart (1962) showed, consider a bichromatic wave field with two short wave components, propagating with slightly different frequencies f and $f + \Delta f$. Theoretically, nonlinear interaction between two short waves excites a secondary wave with a relatively low frequency Δf. This low-frequency wave is anti-phase with the wave group and is therefore named a bound wave. In other words, the bound wave is 180° out of phase with the wave envelope, thus, the trough of the wave envelope coincides with the crest of the bound wave.

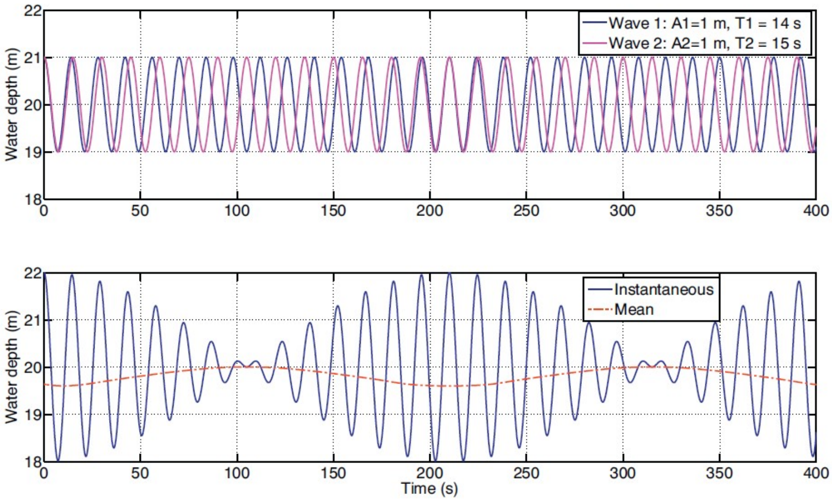

Figure 2.1: An illustration of a bound wave. Upper panel: Time series of two sinusoidal waves with two periods, 14 s (blue) and 15 s (pink), propagating over a flat bottom with 20m water depth. Lower panel: Resulting free surface elevation (blue) and bound wave (red) (Bertin et al., 2018).

Figure 2.1 gives an example of a bound wave, which is excited from a bichromatic short wave group (Bertin et al., 2018).

The bound wave generation can be derived from linearized shallow-water equations:

$$\frac{\partial \zeta}{\partial t} + h\frac{\partial U}{\partial x} = 0, \tag{2.1}$$

$$\frac{\partial U}{\partial t} + g\frac{\partial \zeta}{\partial x} = -\frac{1}{\rho h}\frac{S_{xx}}{\partial x}. \tag{2.2}$$

S_{xx} is the wave radiation stress, and it is expressed as

$$S_{xx} = \frac{1}{2}\rho g A_g^2(\frac{2c_g}{2} - \frac{1}{2}). \tag{2.3}$$

In these equations, x is the cross-shore coordinate with a positive direction to offshore and a origin at the shoreline, t is time, h is the still water depth, U is the depth averaged current velocity, ζ is the surface elevation relative to the still water surface level, ρ is the water density, g is the gravitational acceleration, c_g is the short wave group velocity, $c(x,t)$ is short wave celerity, and $A_g(x,t)$ is the wave group envelop. Cross-differentiating the above equations give

$$\frac{\partial}{\partial x}(gh\frac{\partial \zeta}{\partial x}) + \frac{\partial^2 \zeta}{\partial t^2} = -\frac{1}{\rho}\frac{\partial^2 S_{xx}}{\partial x^2}. \tag{2.4}$$

If the bottom is flat, then the analytical solution for the bound waves ζ_B is obtained:

$$\zeta_B = \frac{-S_{xx}(x,t)}{\rho(gh - c_g^2)} + constant. \tag{2.5}$$

Though the flat bottom assumption is hardly achieved, this equation has been validated in many studies (e.g., Baldock et al., 2000; Battjes et al., 2004; Van Dongeren et al., 2007).

Hasselmann (1962) generalized the above mechanism to two dimensions; the bound wave spectrum is a response of short waves and can be predicted as follows:

$$E_{forced}(\Delta f) = 2\int_{\Delta f}^{\infty} \mathrm{d}f \int_0^{2\pi} \mathrm{d}\theta_1 \int_0^{2\pi} \mathrm{d}\theta_2\, D^2(f+\Delta f, -f, \Delta\theta + \pi)E(f+\Delta f, \theta_1)E(f, \theta_2). \tag{2.6}$$

In this equation, $E(f,\theta)$ is the SS wave energy density directional spectrum. $D(f+\Delta f, -f, \Delta\theta + \pi)$ is the difference-interaction coefficient for two waves with frequencies f and $f+\Delta f$ and directional differences $\Delta\theta (= |\theta_1 - \theta_2|)$.

Numerous studies assumed that bound IG waves would release during short wave breaking, propagating shoreward as free IG waves, then reflected at the shoreline (e.g., Van Dongeren et al., 2003; Battjes et al., 2004; Dong et al., 2009), and they attributes this mechanism to Longuet-Higgins and Stewart (1962). However, Baldock (2012) argued that this assumption should not be attributed to Longuet-Higgins and Stewart (1962), who suggested that the bound IG wave amplitude may decrease following short wave breaking, but might not be released as a free wave. Baldock (2012) reviewed a set of laboratory data sets on IG waves and stated that bound IG waves are not released at breaking, but are still forced by the short wave amplitude and groupiness remaining after the breaking. Clear evidence of the release of bound IG waves due to short wave breaking is lacking.

2.1.2 Moving Breakpoint

Another IG wave generation mechanism was proposed by Symonds et al. (1982), where he considered linearized shallow-water equations with a sinusoidally varying breaking point. The excursion of the breakpoint was assumed to be small in the cross-shore direction. This model considered normally-incident waves with a constant beach slope, and a breaking index γ_b was applied:

$$\gamma_b = \frac{H_b}{h}. \tag{2.7}$$

Here, H_b is short wave height, and h is the water depth at initial wave breaking.

As a result, Symonds et al. (1982) proposed that a time-varying position of the breakpoint, induced by incident wave groupiness, radiates IG waves both shoreward and seaward at the group frequency. The outgoing waves outside the surf zone are the sum of seaward radiated IG waves and initially shoreward radiated IG waves that are reflected at the shoreline. Therefore, the pattern of the resultant outgoing IG waves is dependent on the relative phase between these two seaward propagating IG waves. Figure 2.2 gives a sketch explaining the breakpoint mechanism (Van Dongeren et al., 2016). The breakpoint mechanism has been confirmed through numerical modeling (Van Dongeren et al., 2007), field experiments (Contardo and Symonds, 2013) and laboratory experiments (Baldock et al., 2000).

IG waves may be generated through both bound wave and moving breakpoint mechanisms in the field. Battjes et al. (2004) studied the relative importance of the two mechanisms with laboratory data. They proposed a normalized bed slope β_b to distinguish which mechanism is dominant:

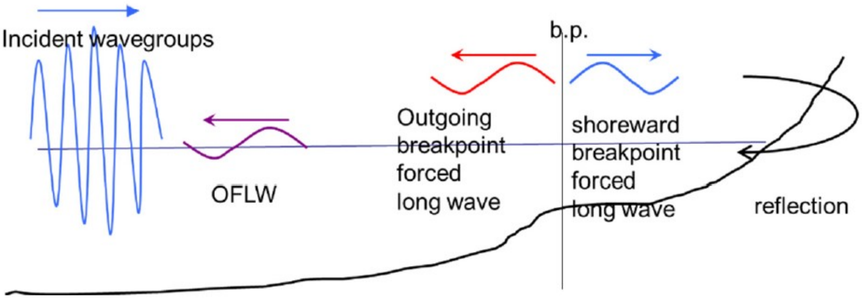

Figure 2.2: Schematic sketch of breakpoint mechanism: Seaward and shoreward propagating IG waves are produced around the breakpoint (b.p.), note the shoreward propagating IG waves are then reflected at the coast. OFLW indicates the resultant outgoing free long (IG) waves (Van Dongeren et al., 2016).

$$\beta_b = \frac{h_x}{\omega}\sqrt{\frac{g}{h_m}}. \tag{2.8}$$

In this equation, h_x is the bed slope, ω is the angular frequency, and h_m is the water depth at the mean breakpoint point. The bound wave mechanism governs if β_b is below 0.3 (mild-slope regime). In contrast, the breakpoint mechanism becomes dominant for typically $\beta_b \geq 1$ (steep-slope regime).

2.1.3 Depth Variation

Besides the two established mechanisms introduced above, an additional free IG wave generation mechanism has received increasing interest recently. Uniform depth was assumed in Longuet-Higgins and Stewart (1962), however, if the depth variation is significant enough to compare with wave group length, free IG waves may be induced.

If the depth variation is one-dimensional and localized in a limited region, then IG waves can radiate away from this region in a different direction from the short wave envelopes. Molin (1982) studied short wave group normally propagating over a 1D topography in deep water ($kh > 1$, where k is the characteristic wave number of the short waves and h is the water depth), while the group length scale is much larger than the water depth. IG waves were found to radiate away from the region with variable water depth, where their velocities are $\sqrt{gh}$. The work of Molin (1982) was later extended by Mei and Benmoussa (1984), who studied obliquely incident short waves at intermediate water depth ($kh = \mathcal{O}(1)$).

Contardo et al. (2021) highlighted the importance of this mechanism. They analytically showed that when short wave groups propagate over varying topography, the flat bottom solution (see Equation 2.5) is the only IG component bound to the short wave group with an anti-phase. The remaining part of the IG waves is the newly generated free IG waves. These free IG waves may influence the phase lag between bound IG waves and their forcing short wave groups, which has been observed in several field experiments (Elgar and Guza, 1985; Inch et al., 2017).

2.1.4 Wind Gusts

Recently, Vrećica et al. (2019) found evidence of deepwater IG wave generation due to offshore storms.

It is commonly assumed that deepwater IG waves are reflected from far coastlines. Ardhuin et al. (2014) treats all coastlines as IG wave sources in their numerical model, and their approach was capable of explaining the observed IG waves in most cases. In deep water, the dispersion relation of ocean surface waves is $(2\pi f)^2 = gk\tanh(kh)$. This makes it impossible for three waves reach resonant condition, i.e., $k_1 = k_2 \pm k_3$. However, inhomogeneities of the wave field may serve an additional component k_b to close the Bragg resonance condition $k_1 = k_2 \pm k3 + k_b$, which is one of the reasons for IG wave generation.

Using a wave action equation, Vrećica et al. (2019) argued that wind gusts could help close the Bragg resonance so that IG waves may be generated. Their results showed good agreements with observations at the East Mediterranean basin of Israel and Aogashima station 70km offshore Japan. They found that the wind gust source term played a minor role in the summer IG wave spectrum and a significant role in the winter IG wave spectrum, the reason for this was not fully understood. More evidence from the field is desired.

This mechanism may explain the IG waves arriving from remote sources, while no apparent storm happens at far coastlines. The wind gust generated IG waves may be one reason for the mismatch between observed and modeled free IG wave height in Rijnsdorp et al. (2021).

2.2 Propagation and Transformation of IG Waves

2.2.1 Energy Dependency

In the nearshore zone, two sources of IG wave energy are commonly identified: locally driven IG waves and IG waves traveling from afar coastlines. IG wave height has shown a positive correlation with offshore wave height (e.g., Herbers et al., 1995; De Bakker et al., 2014). Ruessink (1998b) confirmed this fact based on pressure data obtained from 4m to 10m water depth at Terschelling, the Netherlands. He further showed that IG wave height correlates more strongly with swell waves (0.04-0.14 Hz) than with sea waves (0.14-0.33 Hz). Specifically, the correlation coefficient r for swell waves was about 0.2 higher than for sea waves. Similar results can be found in Elgar et al. (1992), where their observation depth was up to 13m.

Offshore wave parameters that involve wave periods have been proposed to characterize IG wave energy in recent years. Ardhuin et al. (2014) found deepwater IG wave height is highly correlated with a parameter that involves both wave height and mean wave period. Later, Inch et al. (2017) conducted in situ observation at the intertidal zone of Perranporth Beach, UK, where data obtained from 33 consecutive tidal cycles with a large spring tidal range of 6.1m were analyzed. Various offshore parameters were tested, including $H_o^2 T_p$ and $(H_o L_o)^{1/2}$, where H_o is the offshore significant wave height, T_p is the spectral peak period, and L_o is the deepwater wavelength. The authors found that these parameters strongly correlate with the IG wave height, compared to H_o. In addition, Inch et al. (2017) stated that $H_o^2 T_p$ is proportional to the offshore energy flux, thus having a more practical physical meaning than $(H_o L_o)^{1/2}$. As a result, the correlation coefficient of $H_o^2 T_p$ reached 0.93, which excelled other parameters considered in their study (see Figure 2.3). However, the validity of this parameter in other nearshore regions lacks validation.

Furthermore, bound IG waves and free IG waves have different dependencies to swell wave (0.04-0.14 Hz) energy. As predicted by second-order theory for weakly nonlinear waves (Hasselmann, 1962), bound IG wave energy is quadratic related to SS wave energy. This quadratic dependency is confirmed by Herbers et al. (1995), where they observed this relation in 8m, 30m, and 204m depth at different coastal locations in the US (see Figure 2.4 (a)). The scatter of the results at different locations was explained as the difference in the swell directional spectrum and water depths (Herbers et al., 1995). The observed bound IG wave energy decrease with deeper depth is consistent with the theory (Longuet-Higgins and Stewart, 1962; Hasselmann, 1962).

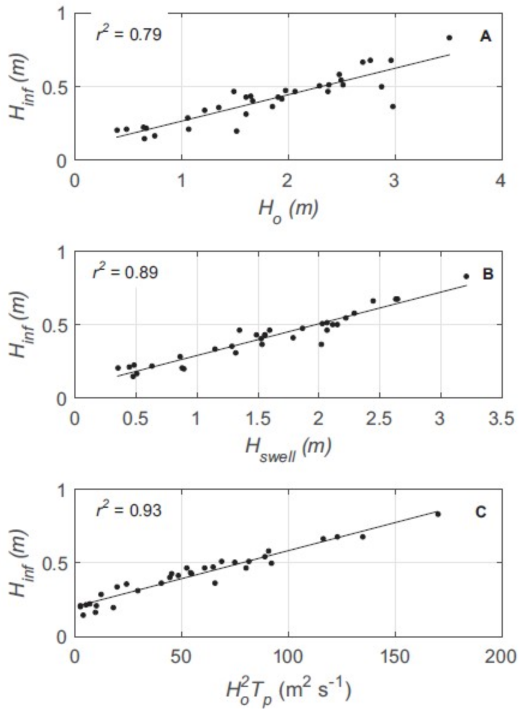

Figure 2.3: IG wave height H_{inf} over the inner one-third of the surf zone, versus (A) offshore significant wave height H_o, (B) offshore significant wave height in the swell frequency band H_{swell}, and (C) $H_o^2 T_p$. Black lines are best-fit linear regression lines with correlation coefficient r (Inch et al., 2017).

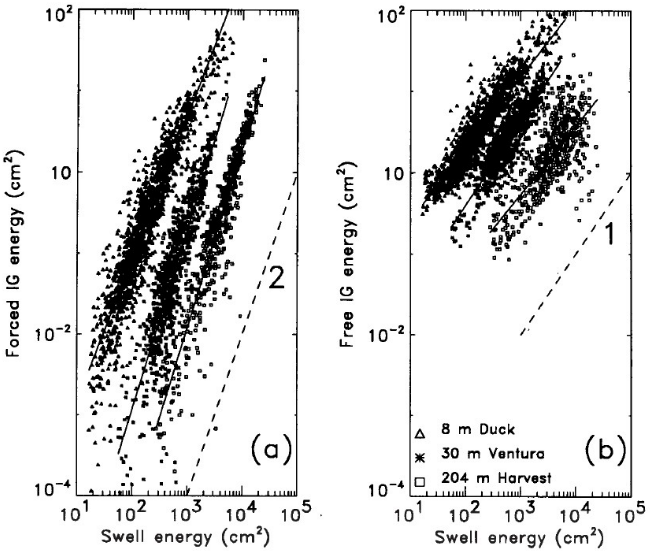

Figure 2.4: (a) Forced (bound) IG wave energy and (b) free IG wave energy versus swell wave energy. IG energies were integrated over the frequencies 0.004-0.05 Hz and 0.004-0.04 Hz in the Atlantic and Pacific, respectively. The solid lines are least-squares-fit curves to the observed energy. Dashed lines marked with 1 and 2 indicate linear and quadratic dependencies, respectively. The data were collected from 8m at Duck (triangles), 30m at Ventura (asterisks), and 204m at Harvest Platform (squares) (Herbers et al., 1995).

If free IG waves are released at a fixed location, they should comply with the quadratic dependency as bound IG waves. In contrast, free IG waves hold a nearly linear dependency on swell energy (see Figure 2.4 (b)). Herbers et al. (1995) argued that this weaker dependence is due to wave breaking. Higher swells break further offshore, and nonlinear energy transfer to IG frequencies is arrested during swell wave breaking. This leads to a weaker dependency on swell energy. An alternative explanation suggested by Herbers et al. (1995) is the effect of the break-point mechanism, where free IG wave energy has a weaker than quadratic dependency on the swell wave energy (Symonds et al., 1982). The scatter of results at different locations implies free IG waves are sensitive to the swell directional spectrum, as is the situation for bound IG waves (Figure 2.4 (b)).

2.2.2 Shoaling

IG waves experience amplitude growth when propagating into shallower waters. Based on IG waves observed in 8m and 13m water depth in Duck, North Carolina, USA, Elgar et al. (1992) showed that the growth rate of IG wave amplitude lies between the conservative shoaling law (Green's Law, amplitude increase proportional to $h^{-1/4}$, where h is the water depth), and the shallow water equilibrium solution (amplitude increase proportional to $h^{-5/2}$, see Longuet-Higgins and Stewart, 1962). Figure 2.5 shows the observed IG wave energy data at 8m and 13m water depth from Elgar et al. (1992). Note that they used IG wave energy instead of IG wave amplitude, so their exponent is doubled.

Van Dongeren et al. (2007) studied the IG wave growth in the shoaling zone based on physical experiments and numerical simulations with a 1:35 bed slope. They showed that milder normalized bed slope β_b (see Equation 2.8) results in IG wave growth trend closer to $h^{-2/5}$. But the water depth in their study was considered intermediate, so the exponent would be less than $2/5$ even if β_b reaches 0. The phenomenon that IG wave growth is more substantial than the conservative shoaling law predicted may come from the phase shift between bound IG waves and their forcing short-wave groups. As introduced earlier, bound IG wave travels in anti-phase with its forcing short-wave groups. However, this is only in the case of the flat bottom (Longuet-Higgins and Stewart, 1962). During short wave groups approaching shallower coastal waters, the phase difference between bound IG wave and wave groups shifts away from 180°. As a result, the IG waves lagged behind the waves. Janssen et al. (2003) stated that the phase shift of bound waves is important since it is a necessary condition for net energy exchange, hence the growth of IG waves. The phase lag between bound IG waves and short-wave groups has been identified in laboratory experiments (De Bakker et al., 2013), and field observations (Masselink, 1995; Inch et al., 2017).

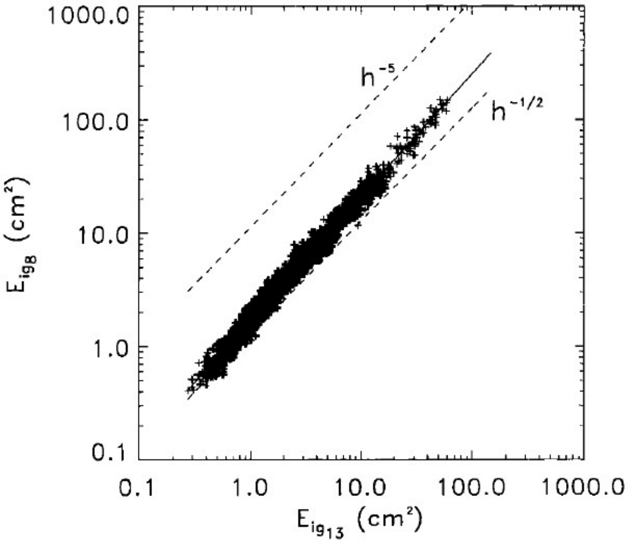

Figure 2.5: IG wave energy observed in 8m depth versus IG wave energy observed in 13m depth at Duck. The solid line indicates a least-squares-fit curve to the logarithm of the data, $E_{ig,8} = 1.7E_{ig,13}^{1.1}$, with correlation coefficient 0.99. The dashed lines indicate the theoretical shallow water dependency between the energies in 8m and 13m water depth for normally incident free waves (energy $\propto h^{-1/2}$) and bound waves (energy $\propto h^{-5}$) (Elgar et al., 1992).

Nevertheless, a complete physical explanation of the phase shift is not fully understood. Contardo et al. (2021) attributed this phase shift to the generation of free IG waves due to depth gradients (Molin, 1982; Mei and Benmoussa, 1984), as short wave groups travel shoreward. However, their conclusion was mainly made based on an analytical model and numerical simulations, the evidence from the field is still absent.

2.2.3 Dissipation

During propagation towards the coast, IG waves can lose a significant fraction of energy. This has been confirmed in many studies, including field observations (e.g., Ruessink, 1998b; De Bakker et al., 2014), laboratory experiments (e.g., Van Dongeren et al., 2007), and numerical experiments(e.g. Ruju et al., 2012).

Bottom Friction

Henderson and Bowen (2002) analyzed field data on a sandy beach with 2m-4m water depth at Duck, North Carolina, USA. An energy balance equation was used to estimate net IG wave forcing and dissipation. IG wave dissipation was found stronger than forcing inside the surf zone. Henderson and Bowen (2002) suggested bottom friction as a primary dissipation mechanism. But later studies showed that bottom friction-induced IG dissipation on sandy beaches is low, it is considered a secondary dissipation mechanism in recent literature (e.g., Van Dongeren et al., 2007; De Bakker et al., 2014). In contrast, the bottom friction coefficient on coral reefs is much larger than on sandy beaches. This mechanism is considered crucial for IG wave dissipation on coral reefs (e.g., Pomeroy et al., 2012).

Energy Transfer

Instead of bottom friction, IG energy dissipation can indirectly occur due to nonlinear triad interactions (Elgar and Guza, 1985). While propagating into shallow waters, IG waves may exchange energy with both short-wave and within IG frequency bands. These energy exchanges occur between three phase-coupled wave frequencies. Specifically, the sum interactions ($f_1 + f_2 = f_3$) transfer energy from spectral peak to its higher harmonics ($f_1 \approx f_2 \approx f_p$, and $f_3 \approx 2f_p$). The appearance of higher harmonics is related to skewed waveshape during shoaling and asymmetric waveshape during breaking. Energy can also be transferred to lower frequencies by difference interactions ($f_1 - f_2 = f_3$).

Two IG dissipation mechanisms for sandy beaches have been suggested. One is the energy transfer from the IG frequency band to the spectral peak or its higher harmonics. The other is the wave interactions within the IG frequency band, which produces higher IG harmonics, allowing IG waves to grow steeper and eventually break. The relative importance of both mechanisms may be related to the beach characteristics.

Ruju et al. (2012) identifies both mechanisms that play a part in IG energy dissipation, using a Reynolds Averaged Navier-Stokes model on 1:20 and 1:30 sloping beaches. They found that in the inner surf zone, IG-IG nonlinear interaction is dominant for IG wave dissipation, whereas in deeper water, nonlinear interactions with SS waves are responsible for the dissipation of IG waves. In contrast, on milder sloping beaches (1:80), De Bakker et al. (2014) used the numerical model SWASH and confirmed that shoreline breaking is the dominant dissipation mechanism for IG waves, while nonlinear energy transfer from IG frequencies to SS frequencies did not play a role.

The slope effect on the roles of these two dissipation mechanisms was later studied in De Bakker et al. (2016), where they conducted numerical simulations using SWASH and studied the nonlinear energy transfer of IG waves. Beach slopes ranging from steep (1:20), moderate (1:50), and mild (1:80) were considered. It was found that wave energy is dominated by IG frequencies close to shore on low-sloping beaches. Here, IG-IG interaction is strong, and higher IG harmonics are generated, which leads to steeper IG waves and eventually wave breaking. A large amount of IG wave energy is dissipated through IG wave breaking, while relatively less IG energy dissipation occurs on steep-sloping beaches, where SS wave energy dominates the wave motion. On steep shores, IG frequencies interact with the spectral peak and transfer to SS frequencies. To conclude, wave breaking was suggested to be the dominant IG wave dissipation mechanism.

Frequency Dependency

Additionally, IG wave dissipation was reported to be frequency-dependent. De Bakker et al. (2014) analyzed two field datasets collected in $\leq$ 2.5m depth on 1:30 and 1:80 sloping beaches in the Netherlands. They showed that IG waves with frequencies high than $\approx$ 0.0167-0.0245 Hz were mainly progressive, indicating that they experience intense dissipation near the shore. On the contrary, IG waves with lower frequencies showed a standing wave pattern, which indicates minor dissipation. The frequency dependency of IG wave dissipation may explain that the bed slope appears steeper for longer IG waves than it does for shorter IG waves.

2.2.4 Reflection

Basic Introduction

Wave reflection may be induced from the variation of the properties of the medium, where waves propagate (Bertin et al., 2018). Ocean currents and water depth variation will cause (partial) wave reflections. Theoretically, the interaction of incident and reflected waves yields a standing wave pattern. For a normally incident monochromatic wave, the resultant surface elevation can be expressed as the superposition of incident wave component η_i and reflected wave component η_r.

$$\eta(x,t) = \eta_i(x,t) + \eta_r(x,t) = a_i \sin(\omega t - kx) + a_r \sin(\omega t + kx). \tag{2.9}$$

Here a_i and a_r are the amplitude of the incident and reflected waves. If a fully reflection occurs, then $a_i = a_r = a$, and

$$\eta(x,t) = 2a \sin(kx) \cos(\omega t). \tag{2.10}$$

This indicates a standing wave pattern, the nodes are at $x = (1/4)\lambda + (n/2)\lambda$, where n is an integer, and λ is the wavelength. The antinodes are at $x = (n/2)\lambda$. In case of a partial reflection, the resultant surface elevation may be written as the sum of a fully standing wave and a progressive wave:

$$\eta(x,t) = (a_i - a_r) \sin(\omega t - kx) + 2a_r \cos(kx) \sin(\omega t). \tag{2.11}$$

Reflection of IG waves

Elgar et al. (1994) studied the reflection of IG waves by analyzing pressure data from bottom-mounted sensors in 13m water depth, 2km offshore of Duck, North Carolina, US. The ratio of seaward to shoreward propagating wave energy R^2 was applied to investigate wave reflection from a sandy beach. R^2 is defined as a function of wave frequency:

$$R^2(f) = \frac{E_{off}(f)}{E_{on}(f)}, \tag{2.12}$$

with

$$E_{on}(f) = \int_{180^\circ}^{360^\circ} S(f,\theta)\mathrm{d}\theta, \tag{2.13a}$$

$$E_{off}(f) = \int_{0^\circ}^{180^\circ} S(f,\theta)\mathrm{d}\theta. \tag{2.13b}$$

Here $S(f,\theta)$ is a frequency-directional spectrum, while 90° and 180° correspond to offshore and onshore propagation, respectively.

Elgar et al. (1994) investigated the variation of R^2 in SS and IG frequency bands. It was shown that SS waves and IG waves have different reflection patterns. The reflection ratio of SS waves was consistent with the hypothesis of Miche (1951):

$$M = \frac{16g^2}{(2\pi)^5}\frac{\tan^5\beta}{H_\infty^2 f^4}. \tag{2.14a}$$

$$R^2 \approx 1, \quad \text{when} \;\; M \geq 1. \tag{2.14b}$$

$$R^2 \approx M, \quad \text{when} \;\; M < 1. \tag{2.14c}$$

In these equations, M is the Miche number, β is the beach slope, H_∞ is the deep water wave height, and f is the deepwater wave frequency.

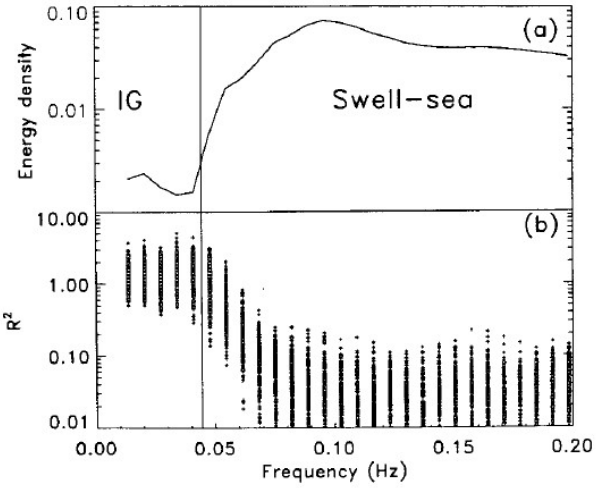

Figure 2.6: (a) Average (over 242 datasets) of normalized frequency spectra and (b) $R^2(f)$ for the 242 datasets. The solid vertical line at $f = 0.044$ Hz indicates the separation of IG from SS frequency bands (Elgar et al., 1994).

However, for IG waves, Elgar et al. (1994) showed that the reflection ratio R^2 is often higher than 1, and reaches 3 when SS waves were most energetic. Figure 2.6 shows the energy density and reflection ratio R^2 for IG and SS waves from 242 datasets of Elgar et al. (1994), different reflection patterns of IG and SS waves can be identified.

Edge Waves

Elgar et al. (1994) suggested that high R^2 for IG waves is due to free IG generation within the surf zone. If all IG energy was generated shoreward of the pressure sensors and either dissipated on the shelf or radiated into the deep sea, then $E_{on}(f) = 0$ and $R^2_{IG} \to \infty$. Additionally, their observations found that onshore propagating bound IG wave energy contributes less than 10% to the total IG wave energy. Therefore, Elgar et al. (1994) suggested that the observed $R^2_{IG} \leq 3$ indicates a significant fraction of IG waves refractively trapped seaward of the array. Herbers et al. (1995) observed broad IG wave spectra in 13m depth at Duck, in contrast to narrow swell spectra (Figure 2.7). This is consistent with the existence of refractively trapped IG waves (edge waves) (Elgar et al., 1994).

As shown above, IG wave reflection may produce refractively trapped wave motion. This motion is also referred to as edge waves and is periodic in alongshore directions. On the contrary, if reflected IG waves can escape to deeper water, they are often called leaky waves.

When IG waves propagate obliquely towards the coast, the water depth varies along the wave crest. Since wave celerity c is determined by the local water depth:

$$c = \sqrt{gh}. \tag{2.15}$$

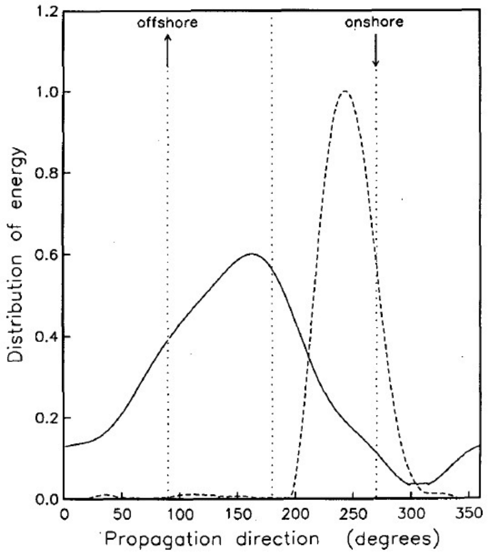

Figure 2.7: Directional distribution of IG (solid line) and swell (dashed line) energy observed at 19:00-21:50 EST 11 October 1990 (Herbers et al., 1995).

Here, h is the water depth. This relation implies that the wave crest travels faster in deeper water, so the incident IG wave crest turns its direction towards the coast. If the IG wave has a

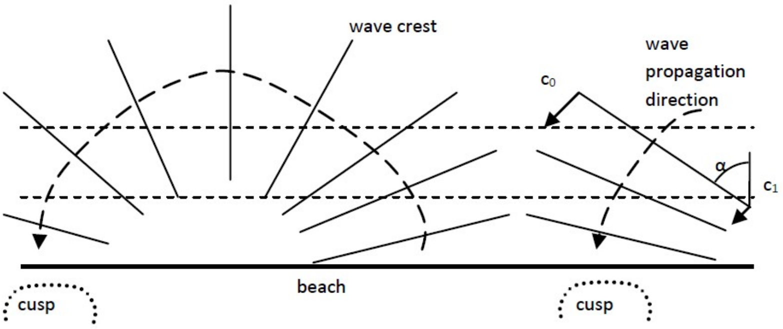

Figure 2.8: Illustration of edge wave development. α represents the incident angle to shore normal, c_0 indicates deepwater wave celerity, and c_1 indicates shallow-water wave celerity. The solid lines are wave crests, and the dashed lines represent depth contours (De Bakker, 2012).

large incident angle, it will reflect at the coast and travel along the coast. See Figure 2.8 for an illustration of edge wave development (De Bakker, 2012).

It is noteworthy that leaky waves and edge waves may exist simultaneously, however, distinguishing them is difficult in field experiments. Moreover, edge waves may be affected by large-scale geographical features. Different features may result in different relative amounts of edge waves. To avoid contamination of edge wave on IG wave reflection estimate, Mahmoudof et al. (2021) suggested only counting shoreward or seaward IG waves within a quadrant perpendicular to the shoreline direction (see Figure 2.9). The accuracy of this conservative setting is not validated yet.

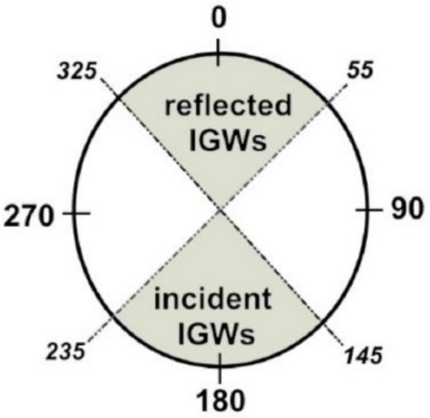

Figure 2.9: The distribution of incident and reflected infragravity wave (IGW) energy in the nautical system according to shoreline direction (Mahmoudof et al., 2021).

2.2.5 Directional Spectra Reconstruction

Basic Procedure of Directional Spectra Reconstruction

A directional spectrum describes the energy spreading of the wave field over both frequencies and directions of propagation. The directional properties of a wave field is formally represented by the directional energy spectrum $E(f,\theta)$ (unit: $\mathrm{N}\cdot\mathrm{m}^{-1}\cdot\mathrm{Hz}^{-1}\cdot\mathrm{rad}^{-1}$), which is a function of frequency f and propagation direction θ. The directional variance spectrum $S(f,\theta)$ (unit: $\mathrm{m}^2\cdot\mathrm{Hz}^{-1}\cdot\mathrm{rad}^{-1}$), is more widely used, and it is proportional to the energy spectrum:

$$S(f,\theta) = E(f,\theta)/\rho g, \tag{2.16}$$

where ρ is the water density (for seawater, ρ is around 1025 $\mathrm{kg/m^3}$) and g is the gravitational acceleration, approximately 9.81 $\mathrm{m/s^2}$. The following decomposition of the directional variance spectrum is often used:

$$S(f,\theta) = E(f)\cdot D(f,\theta). \tag{2.17}$$

Here, $E(f)$ is the classical one-dimensional variance spectrum, which can be estimated by a single record of water surface elevation. It is related to the directional spectrum by:

$$E(f) = \int_0^{2\pi} S(f,\theta)\,\mathrm{d}\theta. \tag{2.18}$$

The directional spreading function (DSF) $D(f,\theta)$ is a function of wave frequency and wave propagating direction. The DSF must suffice two conditions:

$$D(f,\theta) \geq 0,\ \theta \in [0,2\pi]. \tag{2.19}$$

$$\int_0^{2\pi} D(f,\theta)\,\mathrm{d}\theta = 1. \tag{2.20}$$

Assuming an instrument that consists of N sensors, each sensor collects a certain type of wave properties, for example, surface elevation, velocity, or pressure, which are noted as $P_n(t)(n = 1,...,N)$. The relative location of these sensors are expressed as $\boldsymbol{x_n}(n = 1,...,N)$ with respect to an arbitrary point. The measurement duration is T and the sampling time step is Δt. The cross-spectra between two wave signals, say $(P_m; P_n)$, is defined by

$$\Phi_{mn}(f) = \int_{-\infty}^{+\infty} R_{mn}(\tau) \mathrm{e}^{-i2\pi f\tau}\, \mathrm{d}\tau, \tag{2.21}$$

where

$$R_{mn}(\tau) = \lim_{T\to\infty} \frac{1}{T} \int_{0}^{T} P_m(t) \cdot P_n(t+\tau)\, \mathrm{d}t. \tag{2.22}$$

If $m = n$, the $\Phi_{mn}(f)$ is named "auto-spectra". Assume $P_m(f)$ indicates a surface elevation signal, then the auto-spectra $\Phi_{mm}(f)$ is an estimate of the variance spectrum $E(f)$. If $m \neq n$ then $G_{mn}(f)$ is named cross-spectra. The real part of this cross-spectra is called "coincident spectral density functions" or "co-spectra" and noted as $C_{mn}(f)$, while the "quadrature spectral density functions" or "quad-spectra" $Q_{mn}(f)$ denotes the imaginary part of $\Phi_{mn}(f)$.

By measuring three or more wave quantities at a single point or at three or more separated points, it is possible to reconstruct the directional spectrum. If the wave field is considered to be linear and Gaussian, the following equation can relate directional spectrum $S(f,\theta)$ to the cross-spectra $\Phi_{mn}(f)$:

$$\Phi_{mn}(f) = \int_{0}^{2\pi} H_{m,f}^{*} H_{n,f}\, \mathrm{e}^{-i\boldsymbol{k}\cdot(x_n - x_m)} S(f,\theta)\, \mathrm{d}\theta. \ (m = 1, ..., N; m < n) \tag{2.23}$$

In this equation, $\boldsymbol{k}$ is the wavenumber vector $(k\ \cos\theta, k\ \sin\theta)$, $H_m(f,\theta)$ is the transfer function that converts the m^{th} wave properties to surface elevation signal, and "*" denotes the complex conjugate. Equation 2.23 provides the theoretical background of the directional spectra reconstruction methods, as the directional spectrum $S(f,\theta)$ can be obtained from cross spectra $\Phi_{mn}(f)$ among all pairs of measured wave properties.

In practice, reconstructing directional spectra is a challenge. This is because there are infinite unknown parameters in $S(f,\theta)$, which is a continuous function over $[0, 2\pi]$, but only a finite number of equations given by the cross-spectra are available. Numerous directional spectra reconstruction methods have been proposed over the last fifty years, but an all-around and robust method has not been reached. Commonly used reconstruction methods include the maximum likelihood method (MLM) (Capon et al., 1967), iterative maximum likelihood method (IMLM) (Pawka, 1983), Bayesian directional method (BDM) (Hashimoto and Kobune, 1988), the maximum entropy method (MEM) (Lygre and Krogstad, 1986), and extended maximum entropy principle (EMEP) (Hashimoto, 1997). Among these methods, the BDM has been considered to be one of the most powerful approaches (e.g., Benoit et al., 1997; Johnson, 2002), yet it requires at least four wave signals. For wave following buoys (single point measurement that records only three wave signals), the EMEP is a more stable and accurate method. (e.g., Latheef et al., 2017; Lin et al., 2021).

Directional Spectra Reconstruction of IG waves

Reconstructing directional spectra for IG waves may be inaccurate due to the presence of bound IG waves, which can be explained by the second-order wave theory. However, all the abovementioned conventional methods are based on equation 2.23, which follows linear wave theory. This issue was not addressed until recently, when Matsuba et al. (2022) developed a new method for directional spectra reconstruction of IG waves in intermediate (20-30m in their case) water depth. Assuming IG waves are composed of linear (first-order) free IG waves and second-order bound IG waves, they applied weakly nonlinear wave theory of Hasselmann (1962) to account for the contribution of bound IG waves and have shown the superiority of the new method against conventional methods using numerical experiments. Taking second-order waves into consideration gives an updated version of equation 2.23:

$$\begin{aligned}\Phi_{mn}(f) = &\int H^{*}_{m,f} H_{n,f}\, \mathrm{e}^{[ik\cdot(x_n - x_m)]} S(f,\theta) d\theta \\ &+ 2 \iiint H^{(2)*}_{m,f} H^{(2)}_{n,f}\, \mathrm{e}^{[i\Delta\mathbf{k}\cdot(x_n - x_m)]} S\left(f_1,\theta_1\right) S\left(f_2,\theta_2\right) \Omega^2 d f_1 d\theta_1 d\theta_2 .\end{aligned} \tag{2.24}$$

Here, $H^{(2)}_{m/n,f}$ indicates second order transfer functions, h is the still water depth, Ω is the nonlinear coupling coefficient (see Appendix E). According to Hasselmann (1962), a pair of primary waves (with frequencies f_1 and f_2) excites another wave at sub-harmonic frequency $f = |f_2 - f_1|$. For IG frequencies, the first term of equation 2.24 is related to free IG waves (noted as $\Phi^F_{mn}(f)$) and the second term implies the presence of bound IG waves ($\Phi^B_{mn}(f)$).

Note that Hasselmann's theory assumes uniform water depth, thus it is not strictly valid on sloping bottoms. The validity of Hasselmann's theory, hence the applicability of this method, has been confirmed by bispectral analysis (Matsuba et al., 2022). However, Matsuba et al. (2022) concluded that the method might fail to reconstruct directions of free IG waves on steep ($>$ 1/100) and/or shallow ($< 20\ m$) areas. Further validation is needed when applying the new method to other field conditions.

Regarding IG wave estimation and prediction, it is essential to consider the directional distribution of SS waves. Estimating bound IG wave energy (see equation 2.6) requires directional spectra of SS waves (Hasselmann, 1962). Inaccurate estimation of SS directional spreading may result in less reliable IG wave prediction in numerical models such as SWAN (e.g., Reniers et al., 2010).

Moreover, the directional distribution of IG wave energy was found to be dependent on the directional distribution of the concurrent swells. Herbers et al. (1995) observed that broad traveling IG waves often accompany narrow traveling swell waves (see Figure 2.7). When swell waves were traveling upcoast ($90^\circ < \theta < 180^\circ$), IG waves were also propagating predominantly upcoast ($0^\circ < \theta < 180^\circ$). With normally incident swell waves, the IG waves were directed offshore. The directional spectra of IG waves can also be affected by alongshore propagating edge waves (see Section 2.2.4). Therefore, the IG directional wave field prediction can be challenging due to its complex nature.

3 Research Objectives and Research Questions

This study investigates generation, propagation, and directional properties of IG waves in intermediate water depth. The project aims to obtain knowledge of the IG wave energy dependency on the local wave field, and its spatial and temporal variation in intermediate water depth. To this end, field data collected by various instruments implemented in the North Sea were analyzed. The research objective of this study may be fulfilled by answering the following research questions:

1. What offshore parameter does IG energy correlate to the most?
2. How does the IG energy change at different water depths under different wave conditions? And what is the proportion of bound and free IG waves?
3. How to reconstruct the directional spectra of bound and free IG waves, and how do they relate to the directional spectra of SS waves?
4. How do the directional spectra of bound and free IG waves change temporally and spatially?

Only storm conditions will be considered for the last two questions.

4 Methodology

4.1 Field Site

The field experiment was located at the coastal water close to the Sand Engine, Den Haag, the Netherlands, which lies on the southeast edge of the North Sea, see Figure 4.1 (Google, 2022). The coast here is sandy, inlet-free, micro-tidal, and wave-dominated. (Wijnberg, 2002).

Three frames were deployed along the cross-shore direction at the field site from November 2021 to April 2022. The still water depth of the frames was 6.5m, 8.5m, and 13.9m, respectively. Figure 4.2 illustrates the bottom profile and the locations of the frames.

Figure 4.1: Location map of the Dutch coast, the grey arrow points at the location of the studied area, which is shown in the large figure. The blue pin indicates the approximate location of the field experiment (Google, 2022).

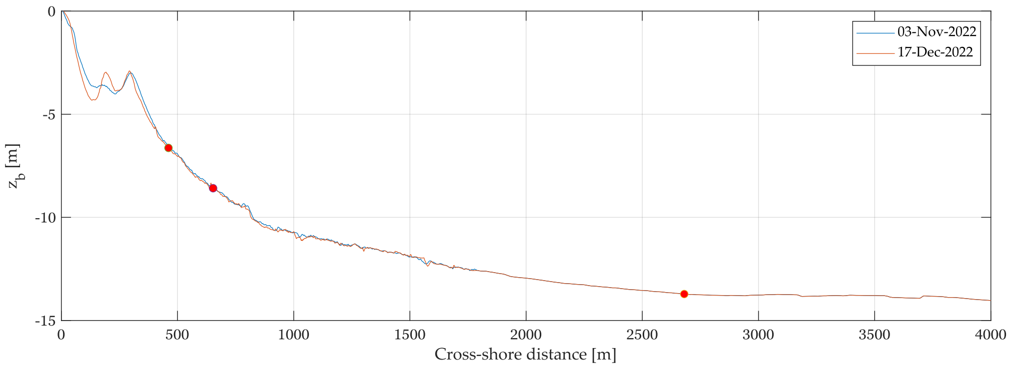

Figure 4.2: The cross-shore bathymetry profile of the study area. The blue line indicates the bathymetry measured on 03 Nov 2021, and the red line indicates the bathymetry measured on 17 Dec 2021. Red dots indicate the location of the instruments, z_b denotes the bed elevation.

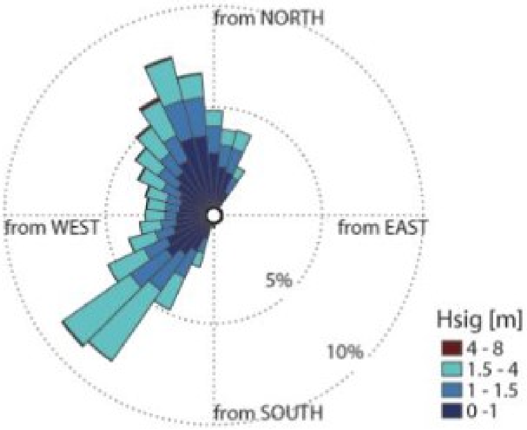

Figure 4.3: The wave rose, illustrating the significant wave height and wave direction in the year 2005-2015, measured in 32 m depth at the Europlatform (Rutten et al., 2017).

The field site is exposed to a bimodal wave climate, with waves arriving from southwest and north-northwest. The wave rose in Figure 4.3 shows the significant wave height and direction in 2005-2015 (Rutten et al., 2017). The annual-averaged significant wave height H_{sig} is 1.3m, with a corresponding peak wave period T_p at 5.7s. The wave condition during spring and summer is relatively low, with H_{sig} at around 1.1m. During autumn and winter, the wave climate is characterized by storms, with H_{sig} up to 5m and T_p up to 9s. The tide is semi-diurnal with a mean tidal range of 1.7m, and the alongshore current can reach 0.5m/s. Moreover, the mean grain size of the sand at the Sand Engine is approximately 280¯m (De Schipper et al., 2016).

4.2 Data Collection

4.2.1 Instrument Configurations

The field experiment used two Nortek Signature 1000 ADCPs, one WorkHorse ADCP, one Sentinel V ADCP, and one Nortek Vector ADV. These instruments were attached to stainless frames

Frame number	Still water depth [m]	Instruments	Instruments used in this study
Frame 1	13.9	Signature ADCP WorkHorse ADCP	Signature ADCP
Frame 2	8.5	Signature ADCP WorkHorse ADCP	Signature ADCP
Frame 3	6.5	Sentinel V ADCP (first period) Nortek Vector ADV (first period) WorkHorse ADCP (second period)	Nortek Vector ADV (first period) WorkHorse ADCP (second period)

Table 4.1: Instruments used in the field experiment.

and were implemented at the prescribed locations. The data was recorded with two successive collection periods: 15 Nov 2021 to 24 Jan 2022, and 24 Jan 2022 to 13 Apr 2022. All the instruments were taken out on 24 Jan 2022 for battery replacement and returned to their previous locations for the second collection period. The ADV was broken after the first collection period and was replaced by the WorkHorse ADCP in the second collection period. In this study, only the data collected from the selected instruments were analyzed, see Table 4.1.

The configuration of the frames was similar. The distance between the ADCPs and the sea bed was 0.63m, which is the height of the pressure sensors and the reference level for the velocity measurements. The pressure sensor and the velocity measurement volume of the ADV were 0.08m and 0.20m above the sea bed, respectively. Figure 4.4 shows one of the frames that attached a Signature ADCP and a WorkHorse ADCP.

ADCP

The Signature ADCPs have five acoustic transducers, four of which are slanted, one is vertical, while the WorkHorse ADCP has only four slanted acoustic transducers. Overviews of the ADCPs are given in Figure 4.5 (Nortek, 2022b) and 4.6 Figure (TRDI, 2007).

Figure 4.4: A frame with a Signature ADCP and a WorkHorse ADCP.

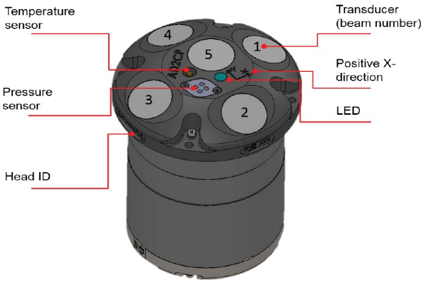

Figure 4.5: Overview of the Signature 1000 ADCP (Nortek, 2022b).

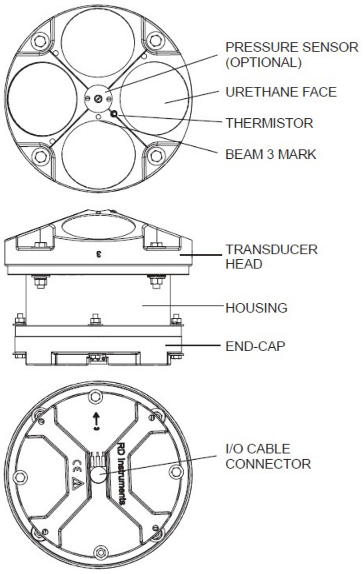

Figure 4.6: Overview of the WorkHorse ADCP (TRDI, 2007).

The ADCP measures water velocity by applying the Doppler effect. The Doppler effect indicates the change in frequency of a wave when a wave source approaches an observer, or when the observer moves relative to the wave source. For example, a sound wave has a higher frequency when it moves to the observer than when it moves away. The ADCP uses the Doppler effect by transmitting a sound pulse and listening for the return pulse. The pulse does not reflect the water itself but small suspended particles in the water. The scattering material passively floats in the water and is assumed to move at the same speed as the water. When the sound pulse hits these particles, part of the acoustic energy is scattered back to the transducer, while the other amount of the acoustic energy travels further and is scattered back later. Measuring the time consumed for the energy to travel two ways, the location of the reflection point can be then obtained.

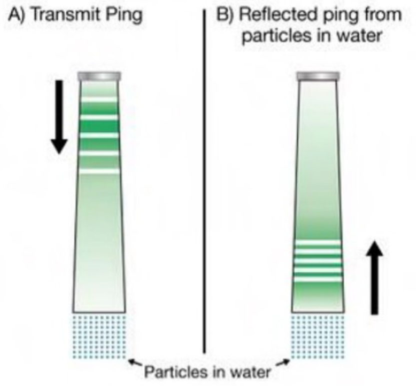

Figure 4.7: Illustration of a pulse transmitted (a) and reflected (b) by particles in the water (Nortek, 2021).

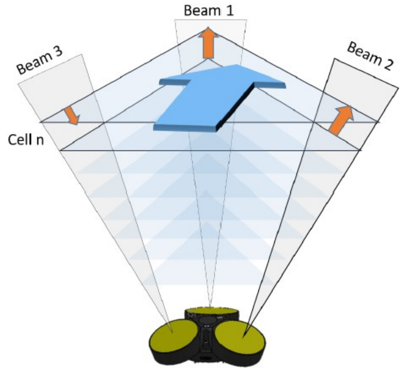

Figure 4.8: Measurement area sectioned into cells of the Signature 55 ADCP (Nortek, 2022a).

ADCP name	Blanking distance [m]	Cell size [m]
WorkHorse	0.74	0.35
Signature (frame 2)	3.0	0.30
Signature (frame 1)	6.0	0.60

Table 4.2: Blanking distance and cell sizes of the ADCPs.

As Figure 4.7 shows, if the distance between the transducer and the particle decrease, the frequency of the reflected pulse (ping) increases (Nortek, 2021). The ADCP relates the change in frequency to a relative velocity of the scattering particle compared to the instrument. By comparing the transmitted wave with the received wave, the current velocity V can be calculated:

$$V = \frac{F_{Doppler}}{F_{source}} \cdot \frac{C}{2}. \tag{4.1}$$

Here, $F_{Doppler}$ is the change in received frequency, known as the Doppler shift, F_{source} is the frequency of the transmitted sound wave, and C is the speed of sound in water.

The ADCP measures the velocity profile through the water column with a series of cells, which defines the depth resolution. Nortek (2022a) illustrated the measurement area sectioned into cells for Signature 55 (three beams), which is comparable with the Signature 1000 (four slanted beams) used in this study (Figure 4.8). The beams measure water velocity in their direction, and each pair of beams (beams 1 & 3, and 2 & 4) measure one vertical and one horizontal velocity. The resultant 3D velocity field is given from the horizontal velocity measured by beams 1 & 3, the horizontal velocity measured by beams 2 & 4, and one of the vertical velocities. The fifth beam is an upright beam, which ensures a well-resolved vertical motion, and is often referred to as an altimeter. The output 3D velocities are obtained by averaging the velocities measured over the area enclosed by the beams in one cell. The cell arrangement of each ADCP used in this study can be seen in table 4.2. The nth cell is centered at a distance equal to: reference level (0.63 m in this case) + blanking distance + (n * cell size).

ADV

The working principle of ADV is similar to the ADCP, which applies Doppler effects for the velocity measurements. The ADV measures velocity by transmitting sound pulses of a specific frequency into the water, The sound wave can be partly reflected towards the instrument, and the reflected signal is then Doppler shifted according to the water velocity. Three receivers are positioned at three beams, which are needed to measure the Doppler shifts and determine the three orthogonal water velocity components. The 3D water velocity in the sampling velocity is calculated based on the orientation of the beams.

The measurement volume of the ADV is defined as the interaction zone of the beam receivers and

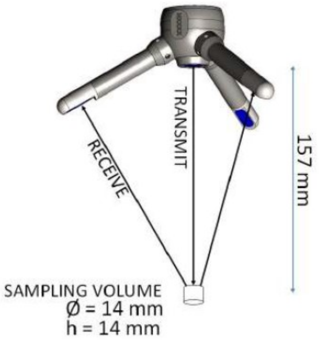

Figure 4.9: ADV beams and their measurement volume (Nortek, 2018).

the central transmitter. For Vector ADV, the measurement volume is 157 mm from the transmitter, with a diameter of 14mm and a height of 14mm (see Figure 4.9). 3D velocities can be obtained from that volume simultaneously.

4.2.2 Obtained Data

Surface elevation (only for ADCP), pressure, and 3D water velocity components (east, north, and up) were recorded from 15 Nov 2021 to 13 Apr 2022, as mentioned earlier. The ADV was broken after the first collection period and was replaced by the WorkHorse ADCP in the second collection period. The Signature ADCP and Nortek ADV were measured continuously with a 4 Hz sampling rate, while the WorkHorse was programmed to record data in 1-hour bursts every 2 hours with a 2 Hz sampling rate.

4.3 Data Analysis

4.3.1 Pre-processing Procedure

Pressure and Surface Elevation

The pre-processing procedure is the same for surface elevation and pressure data; however, an additional process was done first for pressure signals. Raw pressure signals p (unit: dBar) were transformed to pressure head signal H_p (unit: m) by considering air pressure p_{air} and an empirical correction constant d (unit: m):

$$H_p = 10000 \times p_{cor}/(\rho g), \tag{4.2}$$

with

$$p_{cor} = p - p_{air} + d. \tag{4.3}$$

The density ρ for seawater was set to 1025 $\mathrm{kg/m^3}$ and the gravitational acceleration $g = 9.81\ \mathrm{m/s^2}$. The air pressure signal was obtained from KNMI (2022a), which measured daily air pressure signals at an adjacent location to the field site (Hoek van Holland). The correction constant d is an offset that ensures the pressure is zero when the instrument is out of the water. It was set as 9.48m, 9.45m, and 9.45m for frames 1-3, respectively.

The data selection procedure for surface elevation and pressure head signals can then be split into a two-step routine:

1. Examine the signals with the despiking functions of Goring and Nikora (2002). The universal threshold λ_U was empirically determined as 1.25 (See equation 1 in Goring and Nikora, 2002). A data file was regarded as heavily contaminated and discarded if the number of spiky points detected by the functions exceeded 1.5% of the file's total number of data points.
2. For the other data files, the spiky data points were replaced by cubic interpolated data points.

Velocity (ADCP)

The pre-processing procedure of velocity data collected by ADCPs was based on three steps: tilt angle of the instrument, correlation, and despiking threshold:

1. The tilt angle of the ADCP (θ_t) was calculated based on the recorded time series of pitch (θ_p) and roll (θ_r):

   $$\theta_t = \arctan\left[\sqrt{(\tan|\theta_p|)^2 + (\tan|\theta_r|)^2}\right]. \tag{4.4}$$

   A tilted instrument may produce less accurate velocity data since the beams would measure at different depths in one cell (see section 4.2.1). For small tilt angles ($< 10°$), values of horizontal velocities are not significant affected. However, accurate vertical velocity cannot be obtained even if for small amounts of tilt. In this study, vertical velocities were excluded due to highly varied tilt angles throughout the whole data collection period (Figure 4.10). In particular, the horizontal velocities collected by frame 2 in the first collection period were bin-mapped with the help of Ocean Contour software Nortek (2019) since $\theta_t > 10°$.

2. Correlation is a statistical measure of similarities between two consecutive pulses, i.e., how similar the received signal is to itself at a delayed time. A 100% correlation means perfect similarity, while a 0% correlation implies no similarity. The magnitude of the correlation indicates the quality of the velocity data measurement (Nortek, 2022a). A 50% correlation was used to identify low correlation data , which was replaced by cubic interpolated data. A data file was regarded as heavily contaminated and discarded if the number of low correlation points exceeded 5% of the total data points of the file.

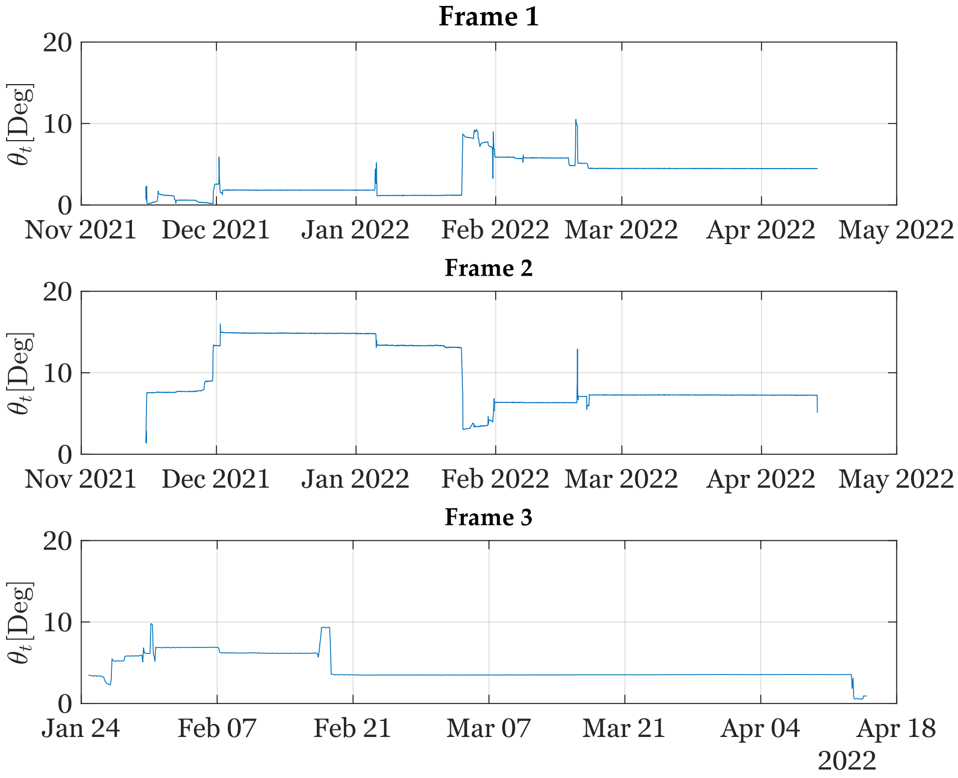

Figure 4.10: Tilt angle of the ADCPs at frames 1-3.

3. Examine the signals with the despiking functions of Goring and Nikora (2002). The criteria here is the same as for pressure and surface elevation signals.

Velocity (ADV)

The pre-processing procedure of velocity data collected by ADV was based on three steps: Signal-to-Noise ratio (SNR), correlation, and despiking threshold:

1. Signal strength (amplitude) measures the magnitude of the acoustic reflection from the water, a weak echo implies noisy velocity data that shows noticeable short-term variability. Signal strength can assess data quality and is often addressed as the Signal-to-Noise ratio. The SNR is a measure of the level of the signal with respect to the background noise level, and is defined as:

$$SNR = 20\log_{10}\frac{Amplitude_{signal}}{Amplitude_{noise}}. \tag{4.5}$$

Following Mori et al. (2007), a 20 dB SNR was used to identify low-quality data, which was replaced by cubic interpolated data. A data file was regarded as heavily contaminated and discarded if the number of low correlation points exceeded 5% of the total data points of the file.

2. The examination of correlation for ADV data is the same as for ADCP data, a higher threshold of 70% was applied, following Mori et al. (2007).
3. Examine the signals with the despiking functions of Goring and Nikora (2002). The criteria are the same as for pressure and surface elevation signals.

Summary

According to different research purposes, the data files were split into 1-hour or 2-hour files, see section 4.3.2 and section 4.3.3. A summary of the original and pre-processed data is given in Table 4.3. The data obtained from three frames show good quality: more than 99% and 96% of the total data files were kept for frames 1 and 2, respectively, and only three hours of data were discarded for frame 3. Only three velocity data cells for Signature ADCPs were used since more velocity components showed no significant improvements in the results of directional spectra reconstruction (see Chapter 5.3.3). For WorkHorse ADCP, the surface elevation and velocity data were unavailable at the time of the thesis due to technical issues.

Instrument name	Collection period	Available data types	Number of original data files	Number of Processed data files (1h)	Number of original data files (2h)	Number of processed data files (2h)
Signature ADCP (frame 1)	First and second	Surface elevation Pressure 3D Velocity components (cell number: 2,5,8)	3572	3536	1786	1768
Signature ADCP (frame 2)	First and second	Surface elevation Pressure 3D Velocity components (cell number 5,7,9)	3572	3457	1786	1727
Nortek ADV (frame 3)	First	Pressure 3D velocity components	1680	1678	840	839
WorkHorse ADCP (frame 3)	Second	Pressure	964	963	-	-

Table 4.3: Summary of the obtained data and practical information about the number of original and processed data files.

4.3.2 1D Spectral Analysis

Wave Parameters

The calculation of various wave parameters was based on 1-hour data blocks (14400 data points). Variance density spectrum was computed using linearly detrended, Hamming-windowed, 50% overlapping segment of 1024 data points, giving a frequency resolution of 0.0039Hz. Significant wave heights (H_{Sig}) for IG (0.005-0.04Hz), SS (0.04-0.33Hz), sea (0.14-0.33Hz) and swell (0.04-0.14Hz) frequency bands (defined as H_{IG}, H_{SS}, H_{Sea} and H_{Swell}) were calculated as shown below:

$$H_{IG} = 4\sqrt{\int_{0.005Hz}^{0.04Hz} E(f)\mathrm{d}f}, \tag{4.6}$$

$$H_{SS} = 4\sqrt{\int_{0.04Hz}^{0.33Hz} E(f)\mathrm{d}f}, \tag{4.7}$$

$$H_{Sea} = 4\sqrt{\int_{0.14Hz}^{0.33Hz} E(f)\mathrm{d}f}, \tag{4.8}$$

$$H_{Swell} = 4\sqrt{\int_{0.04Hz}^{0.14Hz} E(f)\mathrm{d}f}, \tag{4.9}$$

where E is the variance density spectrum.

Pressure head signals were used for IG wave height calculation instead of surface elevation signals. This is because the variance density spectra calculated from surface elevation signals often have unreasonable values, leading to non-physical IG wave heights. See Appendix A for detailed explanations. In case no surface elevation signal is available (frame 3), the variance density spectrum must be corrected due to the depth attenuation of the pressure head signals. The original E should be multiplied by a correction factor K_{lin}, which was determined for frame 3 as:

$$K_{lin} = \min\left\{\left[\frac{\cosh(kh)}{\cosh(kz)}\right]^2, 4\right\}. \tag{4.10}$$

where k is the wavenumber, z is the distance between the pressure sensor and the sea bed, h is the water depth, which can be obtained by:

$$h = z + hp, \tag{4.11}$$

where hp is the value of the averaged pressure head signal. A constant value of 4 was empirically determined in order to prevent overestimated spectrum at high frequencies. See Appendix C for illustrations on the values of K_{lin} and its effect on the wave spectrum.

The lower and higher frequency limit can be chosen according to the frequency bands. Here, the lower limit of the frequency band was set at 0.005 Hz to remove any tidal signal and very low frequency (VLF) motions. To avoid the inclusion of swell energy within the IG frequency band, the upper limit of IG waves was set at 0.04 Hz. The cut-off frequency for sea and swell waves was determined as 0.14 Hz, following Ruessink (1998b). The upper limit of the SS waves was set to 0.33Hz since variance spectra at higher frequencies are wrongly corrected for pressure head signals. See Appendix B for an explanation of the selection of the cut-off frequencies.

Additionally, the peak period T_p was calculated as:

$$T_p = \frac{1}{f_p}. \tag{4.12}$$

Here, f_p is the peak frequency at which the variance spectrum reaches its maximum.

Furthermore, the energy-weighted mean wave angle θ_{mean} was calculated for frame 1 as additional information for offshore wave conditions. It can be simply calculated from the autospectra (C_{uu}, C_{vv}) and cospectrum (C_{uv}) of two horizontal velocity components u and v (Kuik et al., 1988; Herbers et al., 1999). A mean wave angle at frequency f can be estimated with the equation below:

$$\tan[2\theta_{mean}(f)] = \frac{2C_{uv}(f)}{C_{uu}(f) - C_{vv}(f)}. \tag{4.13}$$

A directional spread at f can be written as:

$$\sigma_\theta^2 = \frac{C_{u'v'}(f)}{C_{u'u'} + C_{v'v'}}, \tag{4.14}$$

where u' is the velocity component in the mean direction $\theta_{mean}(f)$, and v' is the velocity component perpendicular to u'. The maximum value of σ_θ is 40.5°, corresponding to an isotropic directional spreading (Kuik et al., 1988).

The Cartesian convention was applied regarding the mean wave angle, i.e., the direction to where the wave points, measured counterclockwise from the East. Considering the along-shore direction of the beach, a wave with a direction of $-26°$ indicates a normal incident wave (see Figure 4.11).

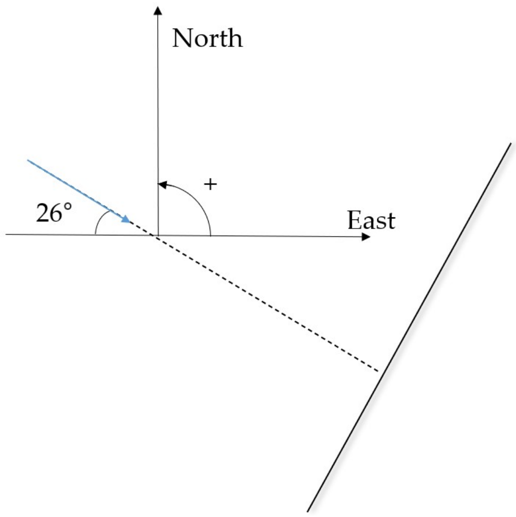

Figure 4.11: Illustration of the Cartesian convention. The thick black line indicates the shoreline and the dashed line indicates the direction of normal incident waves.

Bispectral Analysis

Bispectral analysis was utilized to estimate bound IG wave energy. A bispectrum detects phase coupling between the three frequencies, f_1, f_2, and $f_1 + f_2$. The triad interaction of these frequencies leads to energy exchange from spectral peak to sub- and super-harmonics, which results in a more skewed and asymmetric waveshape (Elgar and Guza, 1985). The bispectrum is expressed as:

$$B_{f_1,f_2} = E[A_{f_1} A_{f_2} A^*_{f_1+f_2}]. \tag{4.15}$$

Here, $E[\ ]$ is the expected value function, A represents the complex Fourier coefficient, and $*$ denotes complex conjugate. The imaginary part of the bispectrum represents energy transfer between the wave triads. Positive value of B_{f_1,f_2} means energy transfer from f_1 and f_2 to $f_3 = f_1 + f_2$, while a negative B_{f_1,f_2} implies energy transfer from f_3 to f_1 and f_2.

The results of the bispectral analysis are sensitive to the noise, thus the bicoherence $b^2_{f_1,f_2}$ is often used to provide normalized measurements of the coupling of the interacting wave components:

$$b^2_{f_1,f_2} = \frac{|B_{f_1,f_2}|^2}{E[|A_{f_1} A_{f_2}|^2] E[|A_{f_1+f_2}|^2]}. \tag{4.16}$$

Additionally, the biphase β_{f_1,f_2} provides a measure of the phase relationship of the interacting wave components. It can be written as (Kim and Powers, 1979):

$$\beta_{f_1,f_2} = \arctan\left[\frac{\mathrm{Im}(B_{f_1,f_2})}{\mathrm{Re}(B_{f_1,f_2})}\right]. \tag{4.17}$$

The stability of the biphase is correlated to bicoherence. Low bicoherence leads to a randomly distributed biphase between π and $-\pi$. If β_{f_1,f_2} is close to 0° (imaginary part close to 0), a skewed waveshape is expected; And if β_{f_1,f_2} is close to -90° (real part close to 0), an asymmetric waveshape is expected.

Bound IG wave height may be estimated with the help of the bispectral analysis. It was assumed that bound IG waves result from the difference in triad interactions between two primary SS wave frequencies f_1 and f_2, while the difference frequency $f = f_2 - f_1$ lies within the IG frequency band. In this case, the fraction of bound wave energy at the frequency f can be obtained by integrating the bicoherence values for all possible primary wave pairs with a frequency difference of f (Herbers et al., 1994):

$$b_{i,f}^2 = \frac{2\int_{f_1} B_{f,f_1}^2 \mathrm{d}f_1}{\int_{f_1} E(f)E(f_1)E(f_2)\mathrm{d}f_1}. \tag{4.18}$$

Integrating $b_{i,f}^2$ over IG frequencies gives the total fraction of bound IG waves:

$$E_{BIG}/E_{TIG} = \alpha_{ii}|b_{ii}|^2. \tag{4.19}$$

with

$$b_{ii}^2 = \frac{2\int_{\Delta f_{min}}^{\Delta f_{max}} \mathrm{d}f \int_{f_1} B_{f,f_1}^2 \mathrm{d}f_1}{\int_{\Delta f_{min}}^{\Delta f_{max}} \mathrm{d}f \int_{f1} E(f_1)E(f_2)\mathrm{d}f_1 \int_{\Delta f_{min}}^{\Delta f_{max}} \mathrm{d}f E(f)}, \tag{4.20}$$

and

$$\alpha_{ii} = \frac{N_2}{N_1^2}, \tag{4.21}$$

in which,

$$N_n = \frac{\int_{\Delta f_{\min}}^{\Delta f_{\max}} \mathrm{d}f \int_{\Delta f}^{\infty} \int_0^{2\pi} \int_0^{2\pi} D^n(f_2, -f_1, \Delta\theta + \pi)\, E(f_1, \theta_1)\, E(f_2, \theta_2)\, \mathrm{d}\theta_1 \mathrm{d}\theta_2 \mathrm{d}f_1}{\int_{\Delta f_{\min}}^{\Delta f_{\max}} \mathrm{d}f \int_{\Delta f}^{\infty} \int_0^{2\pi} \int_0^{2\pi} E(f_1, \theta_1)\, E(f_2, \theta_2)\, \mathrm{d}\theta_1 \mathrm{d}\theta_2 \mathrm{d}f_1}. \tag{4.22}$$

In Herbers et al. (1994), E_{BIG} and E_{TIG} represent the bound and total IG wave energy, respectively. $E(f_i, \theta_i)$indicates directional spectra of SS waves estimated with pressure head signals. Δf_{min} and Δf_{max} are the lower and upper frequency limits of the IG wave. D is the nonlinear interaction coefficient for the pressure head signal. It was assumed that $\alpha_{ii} = 1$ (Herbers et al., 1994). In this way, bound IG energy can be estimated without taking N_n into account, hence only pressure head signal is needed (see Chapter 6.1 for a discussion on the validity of the $\alpha_{ii} = 1$ assumption).

With equation 4.19, the bound IG wave height H_{BIG} can be calculated by:

$$H_{BIG} = 4\sqrt{\int_{0.005Hz}^{0.04Hz} E_{BIG}(f)\mathrm{d}f}, \tag{4.23}$$

and the free IG wave height H_{FIG} can be obtained according to:

$$H_{FIG} = \sqrt{H_{IG}^2 - H_{BIG}^2}. \tag{4.24}$$

The squared ratio of the bound IG wave height over the total wave height can be used to quantify the relative contribution of the bound IG energy to the total IG energy, it is expressed as follows:

$$R_{BIG} = \frac{H_{BIG}^2}{H_{IG}^2}. \tag{4.25}$$

4.3.3 Methods for Directional Spectra Reconstruction

In order to obtain more stable results, the reconstruction of directional spectra was based on 2-hour blocks of data (28800 data points), quadratically detrended, Hanning-windowed, 50% overlapped segment of 1024 data points (surface elevation, pressure head, and various velocity components) were used. The frequency resolution was 0.0039 Hz, and the directional resolution was 5°.

Method Selection

In this study, the new method developed by Matsuba et al. (2022) was used for the data collected from frame 1 to reconstruct directional spectra of IG waves. The calculation procedure can be summarized as below (Matsuba et al., 2022):

1. Compute cross spectra $\Phi_{mn}$for all pairs of wave properties $P_m(t)$ and $P_n(t)$.
2. Reconstruct a directional spectrum of SS waves $S_{SS}(f,\theta)$ using equation 2.23 with a conventional method.
3. Compute Φ_{mn}^B using equation 2.24 based on $S_{SS}(f,\theta)$.
4. Compute Φ_{mn}^F as $\Phi_{mn}^F = \Phi_{mn} - \Phi_{mn}^B$.

5. Reconstruct a directional spectrum of free IG waves $S_{IG}^{F}(f,\theta)$ by replacing Φ_{mn} with Φ_{mn}^{F} in equation 2.23.
6. Reconstruct a directional spectrum of bound IG waves $S_{IG}^{B}(f,\theta)$ following Hasselmann (1962) by adding up all possible couplings between SS components.

In steps 2 and 5, a conventional method may be used; the BDM method was selected in this study. For frames 2 and 3, BDM was directly used to reconstruct directional spectra of IG and SS waves. The new method was not applied at these locations because of the steeper slope and shallower water depth (see Figure 4.2), where Hasselmann's theory fails (Matsuba et al., 2022). See also Chapter 6.2 for an investigation of the validity of the new method at frame 2. A detailed description of the BDM method can be found in Hashimoto and Kobune (1988).

Validation of the new method

Bispectral analysis, following Matsuba et al. (2022), was conducted to check the applicability of their new method. The errors of the new method originate from the deviations of the coupling coefficient Ω and the second order transfer function $H_{m,f}^{(2)}$ between the theoretical solutions of Hasselmann (1962) and the field observations. Thus, the validity of the method can be indirectly examined by evaluating both Ω and $H_{m,f}^{(2)}$.

A cross-bispectrum can be computed as follows:

$$B_{X,Y,Z}\left(f,f_1\right)=\left\langle \frac{\mathrm{d}X_f\mathrm{d}Y_{f_1}\mathrm{d}Z_{f_2}^{*}}{\mathrm{d}f^2}\right\rangle . \tag{4.26}$$

Here, $\mathrm{d}X_f$ is the Fourier amplitude of the f - Hz component of signal X, and $f+f_1=f_2$. f lies within IG frequency band, while f_1 and f_2 are in SS frequency band. Neglecting the linear term of IG waves and second-order SS waves and considering a Gaussian wave field (Matsuba et al., 2022), the cross-bispectrum of (P_m,η,η) can be written as (P_m can be any wave related signal, η is surface elevation signal):

$$2B_{P_m,\eta,\eta}\left(f,f_1\right)=\int_{\theta_1}\int_{\theta_2}\widehat{H}_{n,f}^{(2)}\,\mathrm{e}^{\left(i\widehat{\Delta k}\cdot x_n\right)}S\left(f_1,\theta_1\right)S\left(f_2,\theta_2\right)\widehat{\Omega}\mathrm{d}\theta_1\mathrm{d}\theta_2. \tag{4.27}$$

Note that $\widehat{}$ denotes true values from the field observations. The quantitative examination of Ω and $H_{m,f}^{(2)}$ was done by integrating the cross-bispectra. Let I_B denote true values from the field and I_S the theoretical value from Hasselmann (1962), the following equations arise:

$$I_B=\iint 2B_{P_m,\eta,\eta}\left(f,f_1\right)\mathrm{d}f_1\mathrm{d}f. \tag{4.28}$$

$$I_S = \iiiint H^{(2)}_{m,f} S\left(f_1, \theta_1\right) S\left(f_2, \theta_1\right) \Omega \mathrm{d}\theta_1 \mathrm{d}\theta_2 \mathrm{d}f_1 \mathrm{d}f. \tag{4.29}$$

Small deviation between I_B and I_S indicate small error of Ω and $H^{(2)}_{m,f}$. Therefore, the validity of this method can be examined by comparing I_B and I_S.

5 Results

5.1 Offshore Wave Conditions

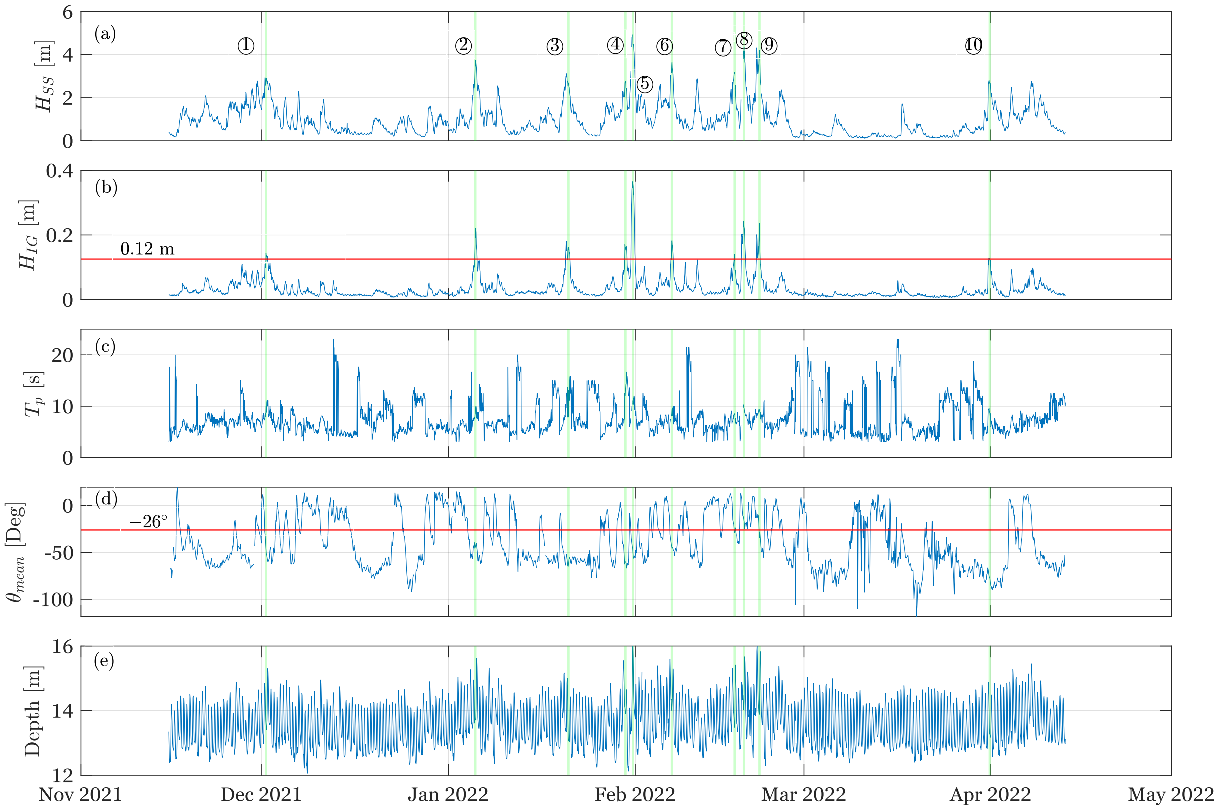

Figure 5.1: Offshore wave conditions (frame 1). (a): Significant wave height of SS waves H_{SS}. (b): Significant wave height of IG waves H_{IG}, the red line indicates $H_{IG} = 0.12$ m. (c): Peak period T_p. (d): Weighted mean wave angle θ_{mean}, the red line indicates the shore-normal direction (-26 °). (e): Water depth. The green lines highlight the events with substantial IG wave height. The circled numbers indicate the selected storms, as shown in Table 5.1.

A summary of the offshore wave conditions, obtained from the data from frame 1, is given in Figure 5.1. Ten storms with substantial IG wave height ($H_{IG} > 0.12$m at frame 1) can be identified throughout the data collection periods. See Table 5.1 for detailed information on these storms. Four of the selected storms were considered highly influential and were named Corrie (31 Jan 2022), Dudley (16 Feb 2022), Eunice (18 Feb 2022), and Franklin (20 Feb 2022) [1]. The maximum

---

[1] For an explanation about the storm naming convention, please see KNMI (2022b).

IG wave height ($H_{IG} = 0.37$m) was observed at 13:00-14:00, 31 Jan 2022 (storm 5), when the SS wave height also reached its highest value ($H_{SS} = 5.04$m).

The IG wave height H_{TIG} among these storms was at least 0.12m, it reached its maximum of 0.37m on 31 Jan 2022, when storm 5 arrived at frame 1 with a very high SS wave height of 5.04m. The bound wave contribution to total IG wave field R_{BIG} during storms varied significantly (0.22 for storm 5 and 0.49 for storm 7). R_{BIG} did not reach its maximum in the most significant storm, indicating SS wave breaking, as will be discussed in section 5.2.4. The peak period T_p of these storm events was usually low ($> 8s$, peak frequency < 0.125 Hz), indicating swell wave dominance. The mean directions θ_{mean} of the storms range between West (storm 8 'Eunice', -14.68°) to North (storm 10, -77.14°), however, most storms were generated from the Northwestern direction (-40 to -60 °). The directional spreading σ_θ of SS waves during these storms were similar, ranging between 21°-27°. Additionally, storm surges can be noticed from Figure 5.1 (e), the magnitude of the surge level was approximately 1-2 m.

Storm numbers	Peak Date	H_{SS} [m]	H_{TIG} [m]	H_{BIG} [m]	H_{FIG} [m]	R_{BIG}	T_p [s]	θ_{mean} [Deg]	σ_θ [Deg]
1	1 Dec 2021	2.86	0.13	0.07	0.11	0.30	9.14	-52.76	26.68
2	5 Jan 2022	3.60	0.19	0.12	0.15	0.39	8.25	-44.44	26.44
3	20 Jan 2022	3.06	0.16	0.09	0.13	0.33	12.19	-53.80	24.64
4	30 Jan 2022	2.71	0.15	0.07	0.13	0.22	12.80	-59.94	22.61
5, 'Corrie'	31 Jan 2022	4.62	0.34	0.18	0.28	0.29	11.13	-46.40	25.26
6	7 Feb 2022	3.53	0.17	0.10	0.13	0.38	9.48	-45.71	24.40
7, 'Dudley'	17 Feb 2022	3.13	0.13	0.09	0.09	0.49	8.26	-25.99	25.57
8, 'Eunice'	19 Feb 2022	4.21	0.22	0.13	0.18	0.32	9.85	-14.68	25.83
9, 'Franklin'	21 Feb 2022	4.02	0.20	0.13	0.15	0.43	9.14	-34.39	26.31
10	31 Mar 2022	2.56	0.12	0.06	0.10	0.24	8.83	-77.14	21.19

Table 5.1: Overview of the selected storms (frame 1).

5.2 IG Wave Variations

5.2.1 IG and SS Variations During Storms

According to Figure 5.1 (a) and (b), it appears that the variation of IG wave height during the field experiment was highly correlated with the SS wave height, indicating the IG motions were mainly locally driven by SS waves. A detailed investigation was conducted to examine the SS and IG wave height variations during storm events.

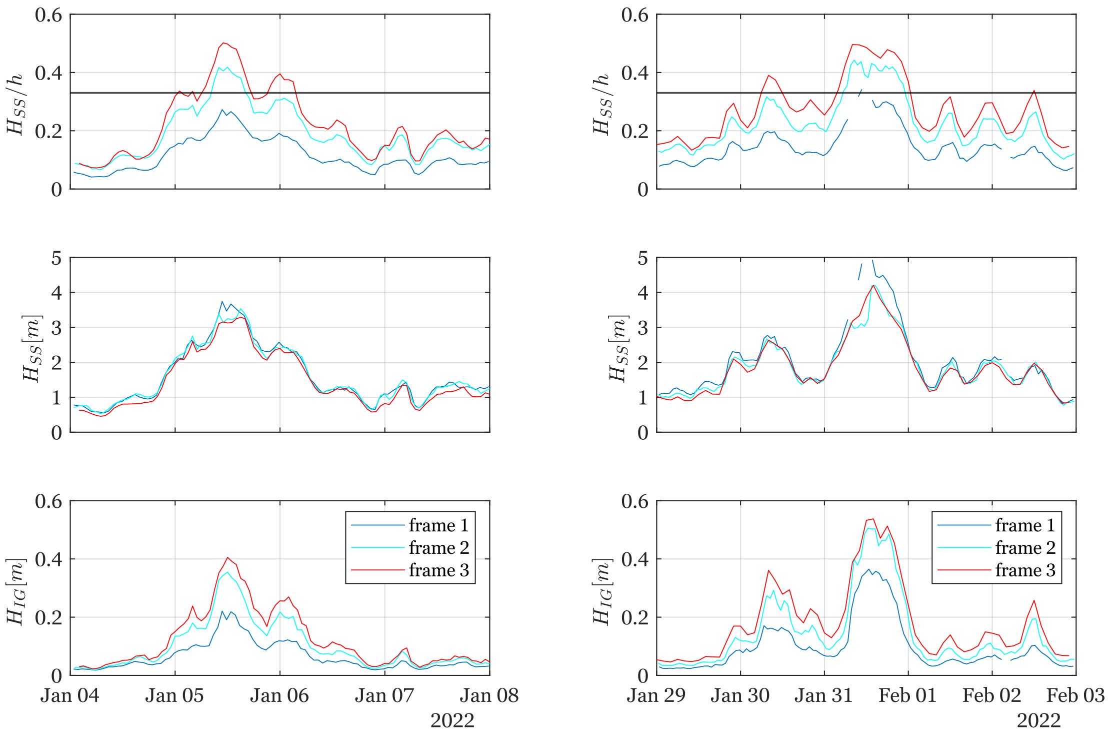

(a) storm 2

(b) storms 4 and 5

Figure 5.2: Illustration of IG and SS wave variations at frame 1 (blue), frame 2 (cyan), and frame 3 (red). Upper panel: Relative wave height. The horizontal black lines indicate a value of 0.33. Middle panel: SS wave height. Lower panel: IG wave height.

Figure 5.2 shows two examples of the variations of SS and IG waves. The relative wave height, defined as the ratio between local SS wave height and the mean water depth (H_{SS}/h), was applied to examine whether the frame was within the surf zone. A value of 0.33 was chosen to indicate the onset of SS breaking, following Van Enckevort and Reincke (1996). During the peaks of the storms, the SS wave heights decreased from frame 1 to frame 3, indicating short wave breaking. An exception occurred on 31 Jan 2022 at frame 2 and frame 3, an increased SS wave height at frame 3 was found, though the relative wave heights for both frames were higher than 0.33. This may be explained by the inaccurate correction factor for pressure head derived spectrum at frame 3, see Appendix A for more information. In contrast to decreasing trend for SS waves during the peaks of the storms, the IG wave shoaling can be clearly identified during the whole period of the storms.

5.2.2 Temporal Variation of IG Waves

From the previous section, it has been shown that the IG wave height correlated with local SS wave height during the storms. To understand the temporal variation of IG waves for all wave conditions, the energy dependence of IG waves was investigated, as illustrated in Figure 5.3. It was found that the IG wave height is indeed correlated with local SS wave height, the correlation coefficient, in this case, is higher than 0.78 for all frames.

However, IG wave height was more strongly correlated to Swell wave height than SS wave height. The higher correlation coefficients between IG wave height and Swell wave height are consistent with previous studies (e.g., Elgar et al., 1992; Ruessink, 1998b), where a lower correlation between sea wave height and IG wave height was also found.

The correlation relation between IG wave height and SS or swell wave height seems not to hold for high IG wave height ($H_{IG} > 0.25$ m for frame 1, $H_{IG} > 0.4$ m for frames 2 and 3, see the upper and the middle panels of Figure 5.3). This was solved by applying $H_{SS}^2 T_p$, which is proportional to the energy flux, following Inch et al. (2017). An even higher correlation was found (see lower panels of Figure 5.3), and the high IG wave heights can be better correlated. Additionally, some data points also indicate sometimes the wave field was characterized by low SS or swell wave height (lower than 1 m) but substantial IG wave height (higher than 0.1 m), see the middle panel in Figure 5.3 (a), for instance. In fact, this is because the cut-off frequency between IG and SS frequencies (0.04 Hz) is too high for these events, so swell energy was included in IG energy (see Appendix B for more information).

For bound and free components of IG waves, their energy dependencies have similar patterns as total IG waves. H_{Swell} always give higher correlation than H_{SS}, and $H_{SS}^2 T_p$ gives the highest correlation. The exception occurs for H_{BIG} at frame 3, possibly due to decreased contribution of bound IG waves because of SS wave breaking, see section 5.2.4. See Appendix D for illustrations of bound and free IG wave height dependencies.

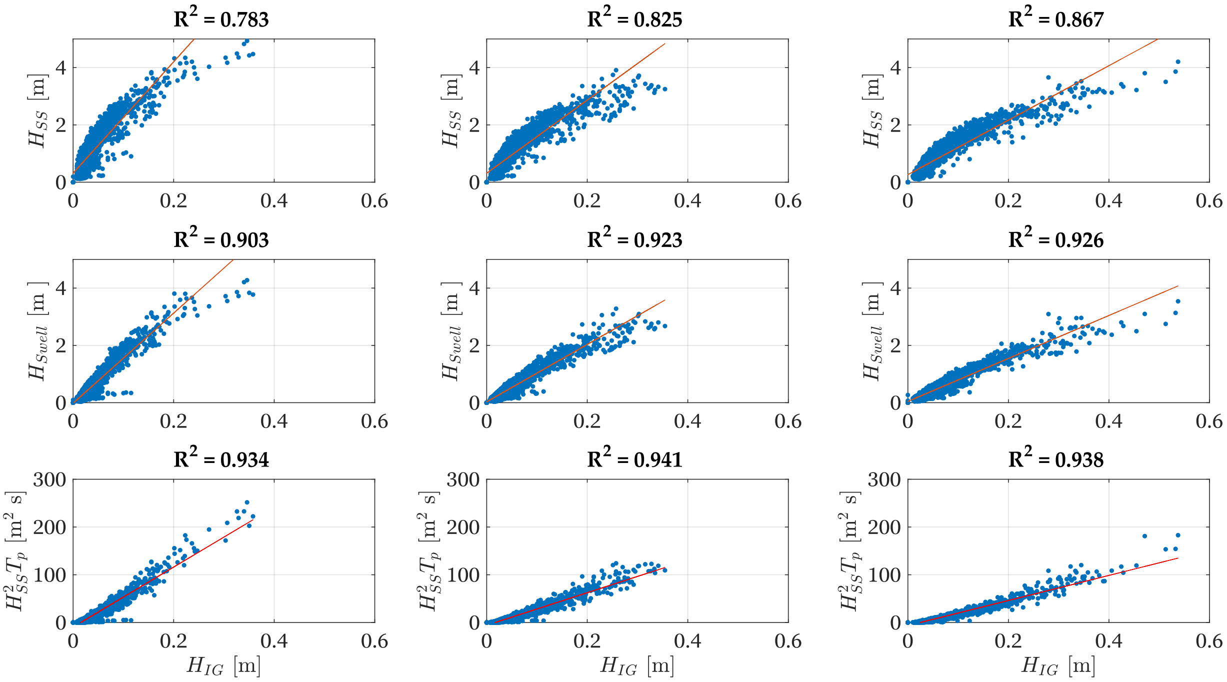

(a) Frame 1 (b) Frame 2 (c) Frame 3

Figure 5.3: IG wave height dependencies at (a) frame 1, (b) frame 2, and (c) frame 3. Upper panel: H_{SS} versus H_{IG}. Middle panel: H_{Swell} versus H_{IG}. Lower panel: $H^2_{SS}T_p$ versus H_{IG}. The red lines indicate best-fit linear regression lines, and the obtained correlation coefficients R^2 are given in the titles of each graph.

It has been shown that both bound and free IG wave heights correlate well with swell wave height (see Appendix D). As introduced in Chapter 2.2.1, Herbers et al. (1995) observed that bound IG waves were quadratically proportional to swell wave energy, while a linear dependence of free IG waves was found. A more detailed investigation was conducted to examine the energy dependencies of bound and free IG waves. Figure 5.4 illustrates that bound and free IG wave energy (represented by wave height square, H^2_{BIG} or H^2_{FIG}) can be associated with swell wave energy (H^2_{Swell}). The red lines in the figure are least-squares-fit curves to the logarithms of the data, and the slope of these lines represents the energy dependencies of the bound or free IG wave energy, as summarized in Table 5.2. Different energy dependencies can be identified. Compared to free IG waves, higher dependence (up to 1.171 at frame 3) is found for bound IG waves, but it is weaker than observed in Herbers et al. (1995), possibly due to SS wave breaking during storms (see next section). For free IG waves, the energy dependency is also weaker (slope less than 1) than that in Herbers et al. (1995), however, the increasing trends of H^2_{FIG} at frames 1 to 3 appear to have higher dependencies as indicated by the best-fit lines. A possible explanation is the contribution of incident free IG waves from nearby coasts, which can be regarded as additional sources to the local free IG wave field (see Chapter 6.3 for a discussion).

Higher dependency is also found at more onshore frames. Compared to frame 1, frames 2 and 3 are more onshore, thus, higher IG energy can be expected because of shoaling. In contrast, the

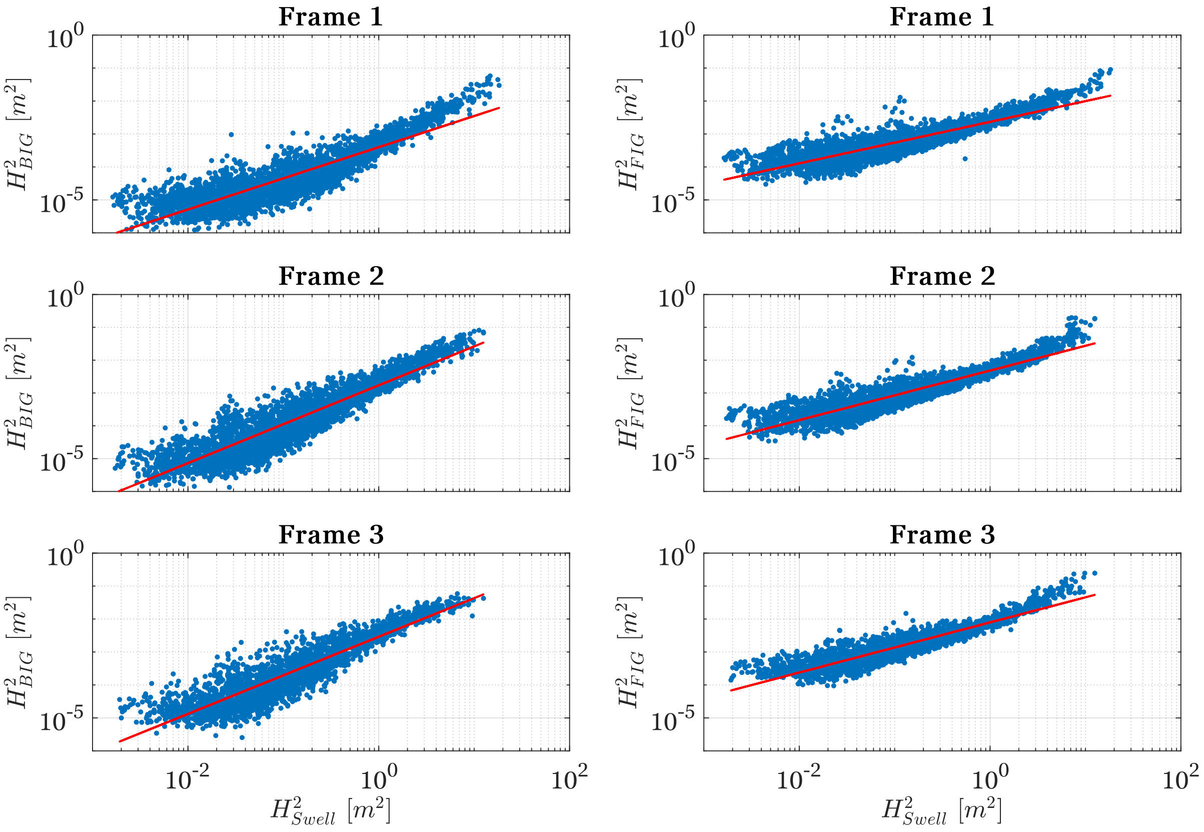

(a)

(b)

Figure 5.4: (a) H^2_{BIG}, and (b) H^2_{FIG} versus H^2_{Swell} at different frames. The red lines are least-squares-fit curves to the logarithms of the data.

amplification of swell wave energy is more constrained by depth-induced breaking. Therefore, higher energy dependency of IG energy may be achieved. For bound IG waves, the decreased slope at frame 3 (1.186 at frame 2, 1.171 at frame 3) may also be explained by the fact that the generation of bound IG waves is constrained by short wave breaking (see next section).

	Bound IG waves	Free IG waves
Frame 1	0.945 (0.929, 0.962)	0.629 (0.619, 0.640)
Frame 2	1.186 (1.169, 1.202)	0.755 (0.744, 0.766)
Frame 3	1.171 (1.150 1.191)	0.761 (0.748, 0.773)

Table 5.2: Slopes of the lines shown in Figure 5.4 (with 95% confidence bounds).

5.2.3 Spatial Variation of IG Waves

The general spatial variability of IG waves was investigated by checking the shoaling pattern between each frame. As introduced in Chapter 2.2.2, if the IG waves consist entirely of bound waves, and these waves were able to reach equilibrium, the wave height ratio between two frames is proportional to $h^{-5/2}$ (Longuet-Higgins and Stewart, 1962). If the IG waves are all free, then the ratio should be $h^{-1/4}$, following Green's Law. In reality, bound and free IG waves can be found in the wave field, therefore, the shoaling pattern is expected to lie between the two theoretical ratios, as mentioned above.

The shoaling patterns of total IG waves between frame 3 to frame 2, and frame 2 to frame 1, are shown in Figure 5.5 (a) and (b). Generally, the data points fall between the two theoretical lines, indicating that both bound and free IG waves contribute to the IG wave field. However, some data points lie outside the theoretical lines.

The interpretation of this issue can be diverse. The estimation of IG wave height may be less accurate if the IG motion is weak (say, less than 0.1m), and the background noise in the signal may affect the resultant wave spectrum, leading to inaccurate results. Additionally, the theoretical solutions assume normal incident shallow water waves, which may deviate from the actual shoaling ratios in the field, where refraction can also play a role. Moreover, the theoretical shoaling ratios were generated using constant still water depth, i.e., 13.9m for frame 1, 8.5m for frame 2, and 6.5m for frame 3. In reality, the water depth changes per data file. Altering the input water level within a reasonable interval, e.g., 1m, does not change the position of the theoretical lines significantly. Therefore, the error introduced by using constant water depth can be neglected.

The above constrictions prevent a clear interpretation of the spatial variation of bound and free components of IG waves, see Figure 5.5 (c) to (e). For bound IG waves, very spread patterns can be identified. However, the patterns follow Green's Law for free waves when $H_{BIG} > 0.1$ m. The shailing of bound IG waves during storms may be hindered by SS wave breaking, hence lead to weaker contribution of bound components to total IG wave field. See section 5.2.4 for more details. For free IG waves, no clear distinction between their shoaling pattern and the shoaling patterns of total IG waves (see Figure 5.5 (a) and (b)). It should be noted that the wave heights of bound IG waves are nearly an order of magnitude smaller than that of free IG waves (compare Figure 5.5 (c) and (e), for instance). Therefore, the similar shoaling patterns of free and total IG waves might be explained by the less important role played by bound IG waves. Apart from the discussed constrictions of the theoretical solutions, the local free IG wave field may also be influenced by edge waves and free IG waves from other coasts, leading to deviation from Green's law.

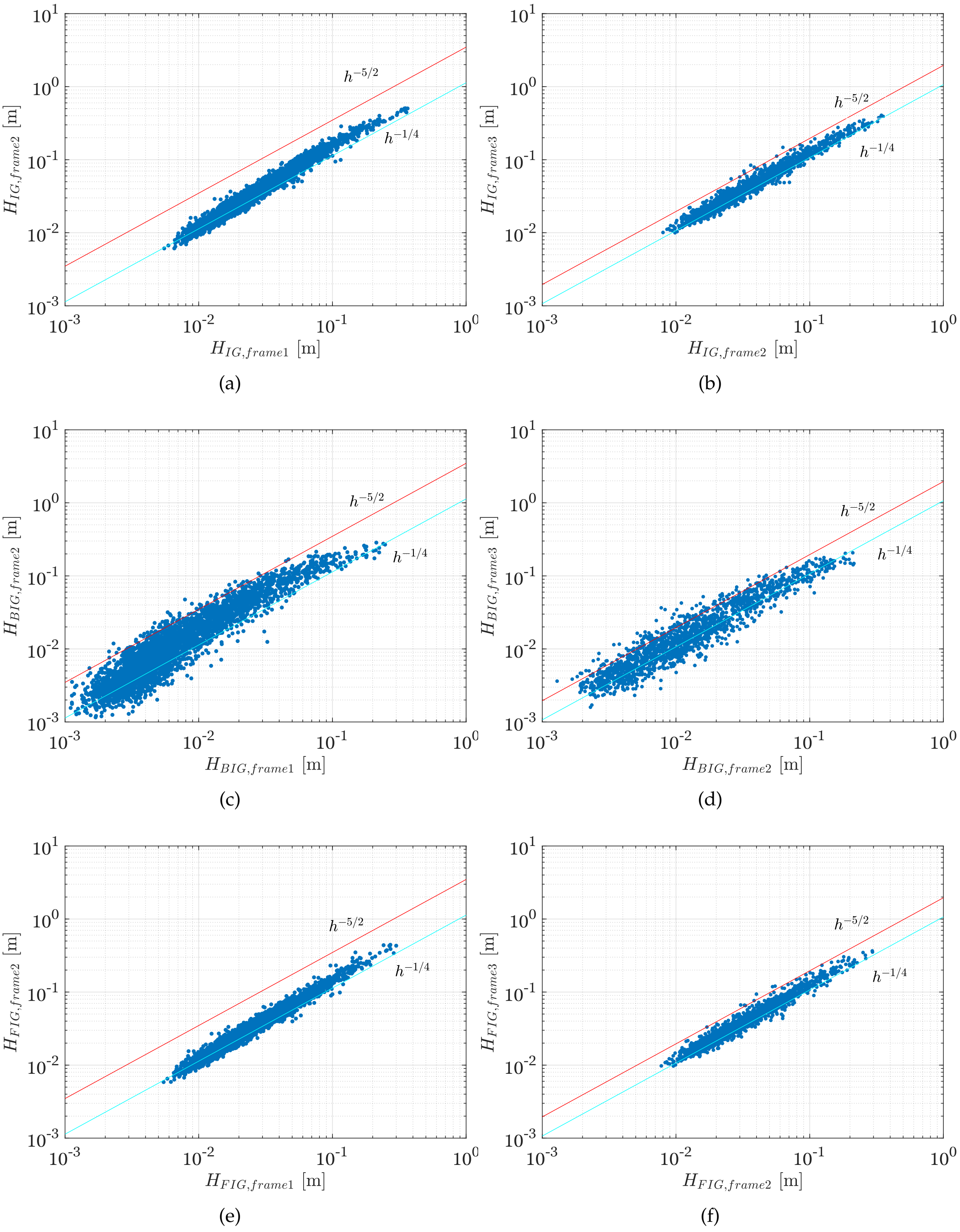

(a) (b)

(c) (d)

(e) (f)

Figure 5.5: shoaling pattern of IG waves. (a): IG wave height observed at frame 3 versus IG wave height observed at frame 2. (b): IG wave height observed at frame 2 versus IG wave height observed at frame 1. (c) and (d): similar figures as in (a) and (b), but with bound IG wave heights. (e) and (f): similar figures as in (a) and (b), but with free IG waves. The cyan line indicates the growth rate of IG amplitude according to Green's Law ($h^{-1/4}$), and the red line indicates the growth rate of IG amplitude according to the shallow water equilibrium solution of ($h^{-5/2}$, according to Longuet-Higgins and Stewart, 1962).

5.2.4 Relative Contribution of Bound IG Waves

As analyzed in the previous section, bound IG wave energy correlates well with short wave energy. In other words, higher bound IG wave height can be expected during storms. This seems to imply a higher relative contribution of bound IG waves to the total IG wave field when short wave energy is more significant, as found in Herbers et al. (1995). However, this is not the case here. Figure 5.6 demonstrates the variation of the relative contribution of bound IG waves R_{BIG} (defined in equation 4.25) as SS wave energy (represented by H_{SS}^2) varies at frames 1 to 3. The colors indicate the relative wave height (H_{SS}/h), which represents the intensity of the SS wave field, a value of 0.33 was used in section 5.2.1 to indicate the onset of SS wave breaking. The values R_{BIG} first increase as H_{SS} increases, along with the growth of H_{SS}/h. The highest values of R_{BIG} at frames 1, 2, and 3 were in the range of 0.7-0.8 (0.71, 0.75, and 0.76, respectively), while H_{SS}/h was around 0.2-0.25, well below 0.33. The increasing trend of R_{BIG} terminates as H_{SS}/h reaches around 0.33 (yellow color), the values of R_{BIG} then tend to decrease (down to 0.1-0.5) with increasing H_{SS}/h (up to 0.5).

To summarize, the trend of R_{BIG} is related to two factors, one is the short wave energy H_{SS}^2, which measures the intensity of the storm; the other one is the relative wave height H_{SS}/h, which indicates the intensity of SS wave field. A sufficiently high value (> 0.33) of H_{SS}/h means more intense SS wave breaking. A higher value of H_{SS}^2 leads to higher R_{BIG}, and the increasing trend of R_{BIG} stops until H_{SS}/h reaches the threshold value of around 0.33. Less bound IG waves can be generated from short wave groups. Therefore, the relative contribution of bound IG waves tends to decrease during intense storms, where the group structure of SS waves was deconstructed due to wave breaking.

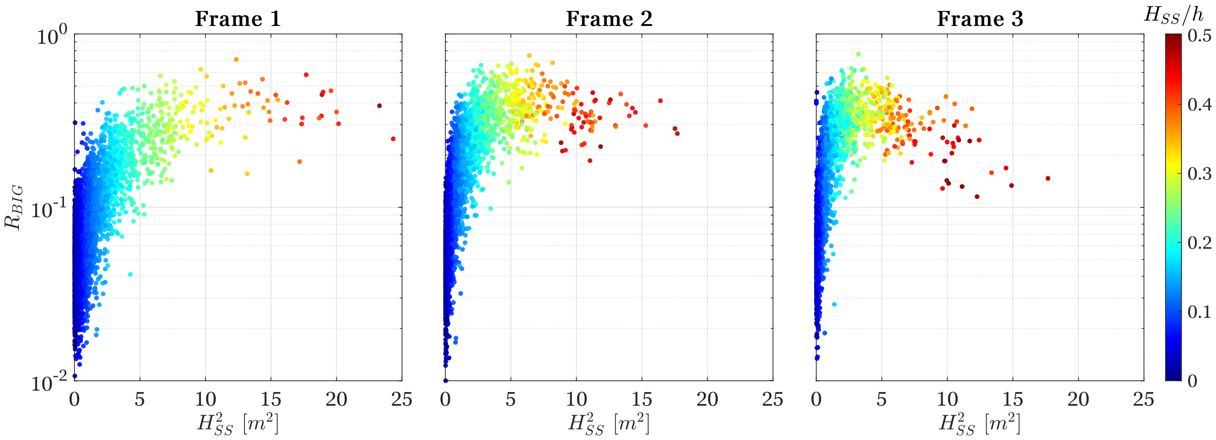

Figure 5.6: R_{BIG} versus H_{SS}^2 at frames 1, 2, and 3. The colors show the relative wave height H_{SS}/h at different frames.

A detailed example of the temporal variation of the relative contribution of bound IG waves is shown in Figure 5.7, which illustrates the time series of bound IG wave height H_{BIG}, total IG wave height H_{TIG} and the relative contribution of bound IG energy R_{BIG} from 29 Jan 2022 to 3 Feb 2022. Although total IG wave heights at different frames show a clear amplification trend throughout this period, and the bound IG wave heights also follow this trend in general, the bound IG wave heights do not demonstrate amplification around the peak of storm 5 on 31 Jan 2022. In fact, R_{BIG} decreased from around 0.5 at frame 1 to less than 0.2 at frame 3 on 31 Jan 2022. This decreasing trend can be related to SS wave breaking, see also Figure 5.2 (b), the relative wave heights H_{SS}/h were below 0.33 during the peak of storm 4 (30 Jan 2022) at frame 3, and during storm 5 (31 Jan 2022) at frames 2 and 3. The group structure of the SS waves during peaks of the storms was destroyed, hence less bound IG waves could be generated, leading to reduced values of R_{BIG} at frames 2 and 3.

It can be concluded that bound IG energy is correlated with total IG energy, hence also the short wave energy (see also section 5.2.2), but the contribution of bound IG waves tends to decrease during intense storms, where the group structure of SS waves was deconstructed due to wave breaking.

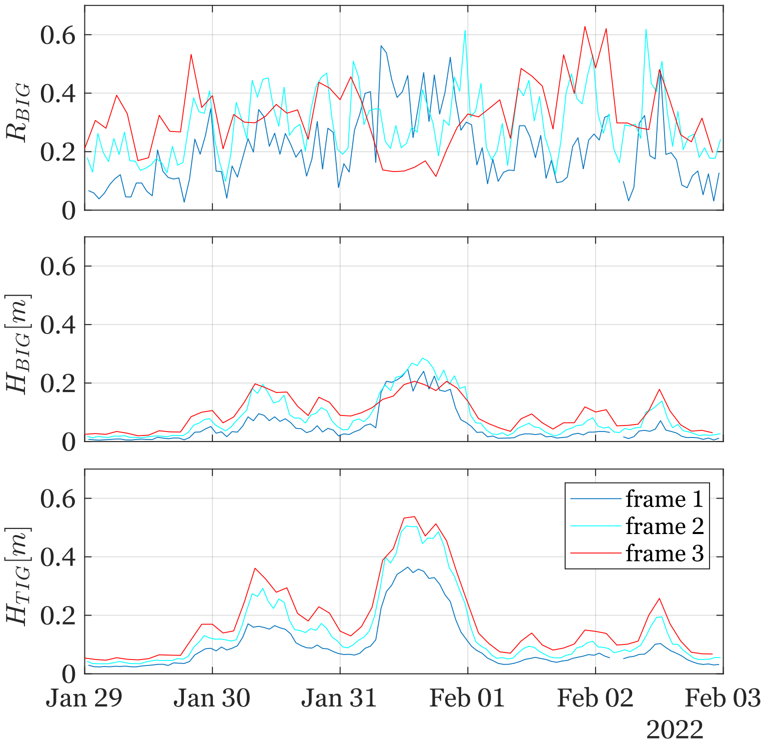

Figure 5.7: Illustration of bound and total IG wave variation in storms at frame 1(blue), frame 2 (cyan), and frame 3 (red). Upper panel: relative contribution of bound IG energy to total IG energy R_{BIG} (see equation 4.25. Middle panel: bound IG wave height. Lower panel: total IG wave height.

5.3 Directional Properties of IG and SS Wave Field

5.3.1 Validation of the New Method

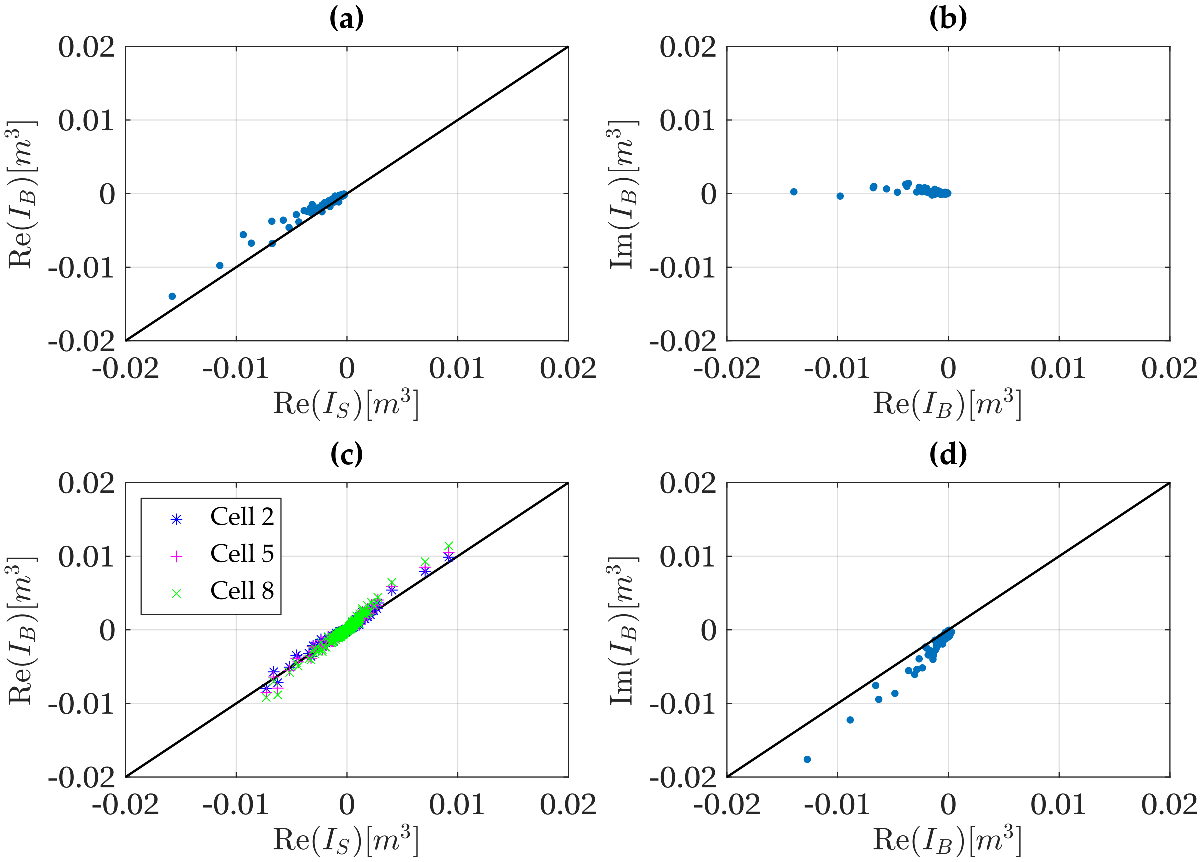

Figure 5.8: Results of cross-bispectral analysis for 158 stormy events (frame 1). (a), (b): Evaluation of pressure head signal with $B_{p,\eta,\eta}$. (a): $\mathrm{Re}(I_S)$ versus $\mathrm{Re}(I_B)$. (b): $\mathrm{Re}(I_B)$ versus $\mathrm{Im}(I_B)$. (c): Evaluation of velocity signals at different velocity cells with $B_{u,\eta,\eta}$, $\mathrm{Re}(I_S)$ versus $\mathrm{Re}(I_B)$. Blue asterisk: cell no. 2, magenta plus sign: cell no. 5, green cross: cell no. 8. (d): Evaluation of surface elevation signal with $B_{\eta,\eta,\eta}$, $\mathrm{Re}(I_S)$ versus $\mathrm{Re}(I_B)$.

As introduced in Chapter 4.3.3, the validity of the method proposed in Matsuba et al. (2022) must be examined before analyzing data at frame 1. Figures 5.8 (a), (b) show the results of $B_{p,\eta,\eta}(f, f_1)$ to investigate the applicability of using the pressure signal. In general, the theoretical I_S (note that I_S is a real number) correlates well with the observed I_B. The slight underestimation of $\mathrm{Re}(I_B)$ at large values can be attributed to the overestimation of nonlinear interaction coefficient Ω, and may be explained by the argument of I_B, i.e., $\mathrm{Re}(I_B)$ versus $\mathrm{Im}(I_B)$ shown in Figure 5.8 (b). Theoretically, the argument of $B_{p,\eta,\eta}(f, f_1)$ is $\pm\pi$, hence the argument of $\mathrm{Re}(I_B)$ is expected to be $\pm\pi$ as well. The deviations in Figure 5.8 (b) are mostly small, indicating that the bound IG waves are delayed, compared with the equilibrium solution of Hasselmann (1962). The phase lag shown here has been identified in previous studies (see Chapter 2.2.2). Good agreement between observation and theory was also found for velocity signals at different positions, see Figure 5.8 (c).

The evaluation of $B_{\eta,\eta,\eta}(f, f_1)$ shows an overestimation of $\mathrm{Re}(I_B)$, which indicates that the surface elevation signal should not be included for directional spectra reconstruction of IG waves, see Figure 5.8 (d). The source of errors, in this case, appears to be related to the wrongly measured low-frequency surface elevation signals (see Appendix A for more information).

To conclude, the new method of Matsuba et al. (2022) can be applied at frame 1, though surface elevation signal should not be used for directional spectra reconstruction of IG waves. Moreover, Matsuba et al. (2022) suggested that their method is applicable in intermediate waters ($h = 20 - 25$m, in their cases). The results analyzed above have broadened this method's applicability to shallower water ($h = 13.9$m at frame 1).

5.3.2 Artifact Caused by the BDM Method

SS wave spectra for different frames were reconstructed using the BDM method. A ubiquitous feature of the results is that a small amount of energy was assigned to the opposite direction of the dominant wave angle. This phenomenon lacked a physical explanation and was regarded as an artifact. To eliminate the artifact, only half (180°) of the reconstructed SS spectra were preserved, the central directions of the spectra are the directional bins where the energy is the highest.

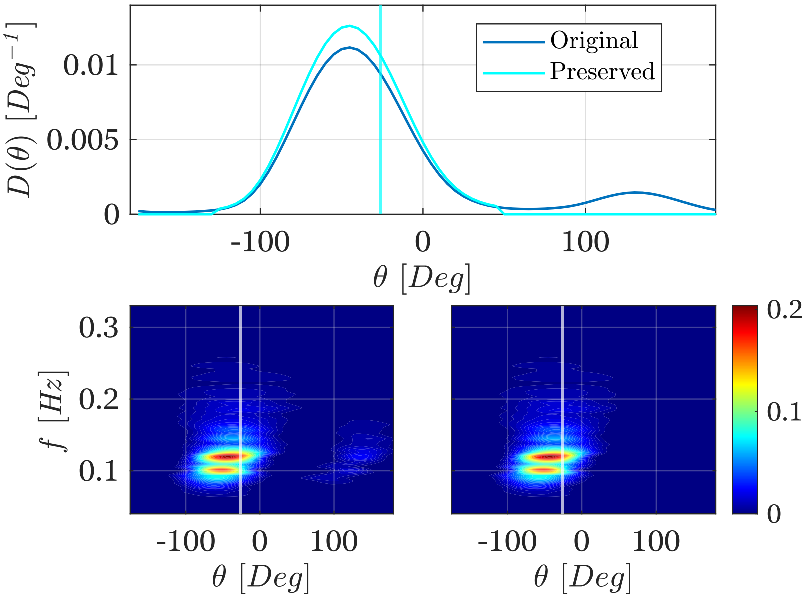

Figure 5.9: Artifact caused by the BDM method (frame 1). Upper panel: Directional spreading functions of the original SS wave spectra (with artifact, blue) and the preserved SS wave spectra (without artifact, cyan), lower left: directional spectrum of the original SS waves, lower right: directional spectrum of the preserved SS waves. Vertical lines indicate the shore-normal direction. Time of observation: 12:00-14:00, 31 Jan 2022.

5.3.3 Sensitivity Test

Surface elevation or pressure head and velocity signals were applied to reconstruct directional spectra. As introduced in Table 4.3, for ADCPs, there were two velocity components (East and North) in each velocity cell, and multiple velocity cells were available. To reduce the time consumed in directional spectra reconstruction, a sensitivity test was done to examine the number of velocity components required to obtain stable results.

Figure 5.10 shows an example of this issue: the reconstructed directional spectrum of SS, free and bound IG waves during the peak of storm 2 on 5 Jan 2022. If only one velocity cell was used (three wave signals in total), the directional spectrum of SS waves is not accurate since the resultant spectrum at high frequencies ($f > 0.13$ Hz) is evenly distributed over the directional bins. This problem was solved when two or more velocity cells were applied. Increasing the number of velocity cells to four does not significantly improve the reconstructed SS wave spectra.

For free IG waves, a similar conclusion can be drawn. Though four velocity cells (case 4) appear to give more distinct results, the directional distribution of free IG waves shows similar characters for cases 3 and 4. For bound IG waves, no apparent differences were found for cases 2 to 4.

From the analysis above, it is concluded that using three velocity cells gives sufficiently stable and accurate results for directional spectra reconstruction.

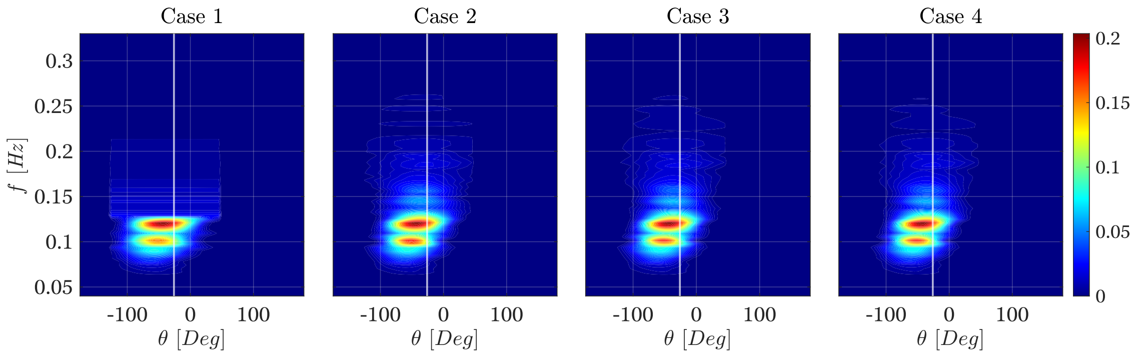

(a) Directional spectrum of SS waves

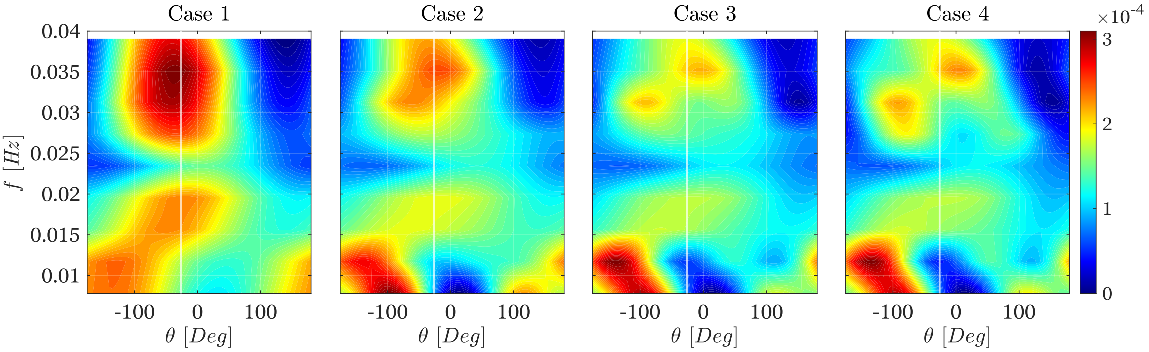

(b) Directional spectrum of free IG waves

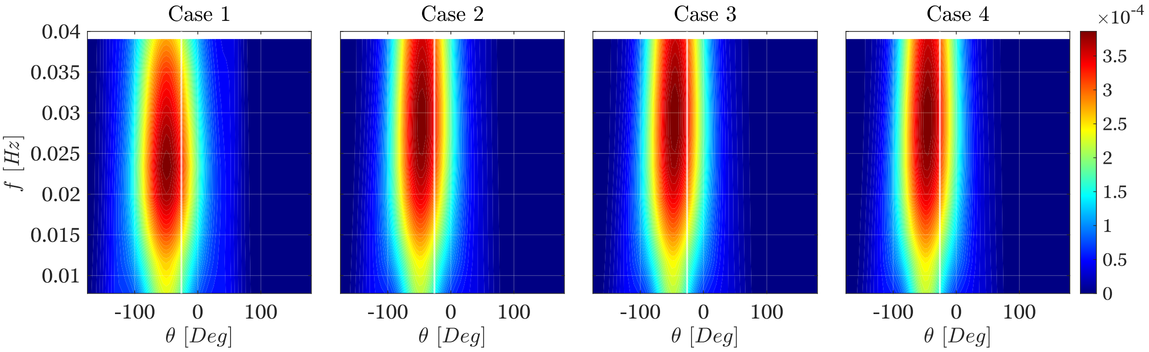

(c) Directional spectrum of bound IG waves

Figure 5.10: Directional spectrum of SS (a), free IG (b), and bound IG (c) waves (frame 1). Unit: [m^2/Hz/Deg]. Case 1: one velocity cell applied. Case 2: two velocity cells applied. Case 3: three velocity cells applied. Case 4: four velocity cells applied. Vertical lines indicate the shore-normal direction. Time of observation: 10:00-12:00, 5 Jan 2022.

5.3.4 Directional Properties of IG and SS Wave Field During Storms

Directional spectra of IG and SS waves during peaks of ten selected storms throughout the data collection periods at frame 1 were reconstructed. See Table 5.1 for an overview of these storms.

Figure 5.11 shows the directional spreading functions $D(\theta)$ of different waves, and reconstructed wave spectra of SS, bound IG, and free IG waves. The reconstructed directional spectra of bound IG waves are closely related to the directional spectra of SS waves. They always have the same peak direction, while bound IG waves have a larger directional spreading than SS waves. This phenomenon is expected since the directional spectra of bound IG waves were obtained according to Hasselmann (1962) in the method of Matsuba et al. (2022).

The conventional methods assume a free (first-order) propagating wave field, hence cannot distinguish bound (second-order) IG waves from the total IG wave field. The use of the new method provides an estimation of the bound IG wave spectra, making a more precise reconstruction of free IG waves possible. Since the theory of Hasselmann (1962) is implemented in the new method, the direction and frequency distributions of bound IG waves are determined by the directional spectra of SS waves. Narrower frequency distribution of the SS variance spectrum leads to lower frequency peaks of bound IG waves; a narrower directional distribution of SS directional spectrum determines a narrower bound IG wave spectrum over the directional domain. In addition, the reconstructed directional spectra of total IG wave of the new method always show narrower directional distribution, compared to that of BDM. Thus, the conventional method yields underestimated bound IG waves, compared to the new method.

With the help of the new method developed in Matsuba et al. (2022), Figure 5.11 shows the very first illustration of the 2D free IG wave field in the North Sea. No previous study has observed such highly varying free IG waves off the Dutch coast. The attempt to simply link the directional properties of SS waves to that of free IG waves was not successful. The reconstructed directional spectra of free IG waves are very diverse, showing the complex nature of the free IG wave field. The broad directional distribution of free IG waves is found for all the storms, which is consistent with previous studies (Herbers et al., 1995). However, the peak direction of the free IG waves varies dramatically. The obtained directional spectra of free IG waves may be categorized as follows:

1. Storms 1 and 2: SS waves came from the Northwest, while low frequency (0.01-0.02 Hz) free IG waves traveled from alongshore, mostly seaward. Seaward propagating free IG waves are often assumed in the literature, and have been observed (e.g., Herbers et al., 1995; Matsuba et al., 2022). However, shoreward propagating components can be identified for higher IG frequencies during storm 2. These IG waves may be related to low-frequency swells, which follow the direction of SS waves.
2. Storms 4 and 5: Incident free IG waves along with SS wave direction can be identified, with possible low-frequency swells traveling in the same direction. These free IG waves

may travel from distant coasts, where storms made their landfalls (Rijnsdorp et al., 2021). Since the North Sea is relatively small, it is possible that one storm affects different coasts (e.g., UK and Danish coasts), and reflected free IG waves are recorded off the Dutch coasts. Furthermore, reflective free IG waves are found (storm 4), in the opposite direction of the incident free IG waves.

3. Storms 3, 6, 7, 8, 9: Multiple free IG energy lumps reside at different locations in the frequency-direction domain. The directional spreading functions of free IG waves in these storms show multiple peaks (e.g., storm 7), or nearly evenly distributed patterns (e.g., storm 6).
4. Storm 10: Isotropic distribution of free IG waves. The IG wave height, in this case, was the lowest among all the selected storms.

Two phenomena may be considered to explain the directional properties of the free IG waves,. First, the directional spectra of free IG waves may be influenced by refractively trapped IG waves, i.e., edge waves, see Chapter 2.2.4, which have complex patterns that can be controlled by coastal topography and engineering structures. Second, free IG waves generated at other coasts in the North Sea may play an important role, as suggested in Rijnsdorp et al. (2021). These free IG waves from remote sources may (partly) explain the incident free IG waves in this study. The origin(s) of these incident IG waves are surmised and discussed in Chapter 6.3.

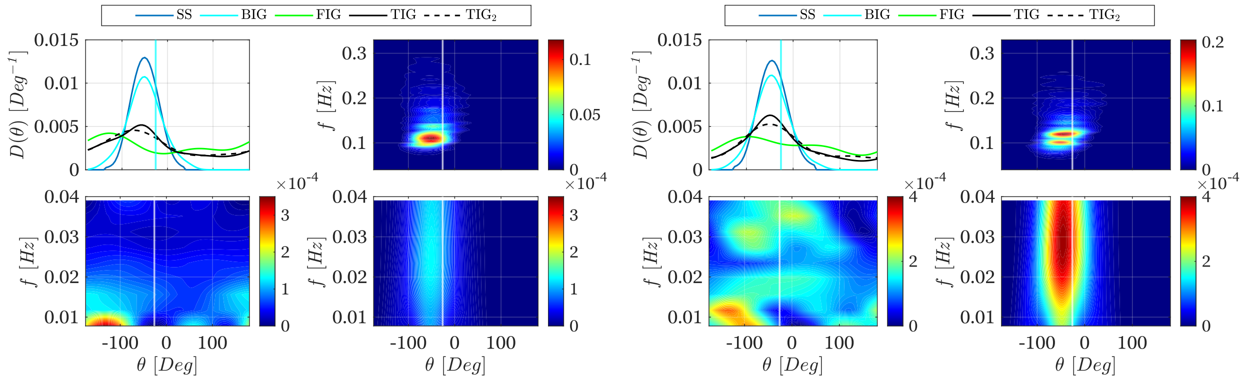

(a) storm 1, 1 Dec 2021. $H_{SS} = 2.86$ m, $H_{FIG} = 0.11$ m, $H_{BIG} = 0.07$ m.

(b) storm 2, 5 Jan 2022. $H_{SS} = 3.60$ m, $H_{FIG} = 0.15$ m, $H_{BIG} = 0.12$ m.

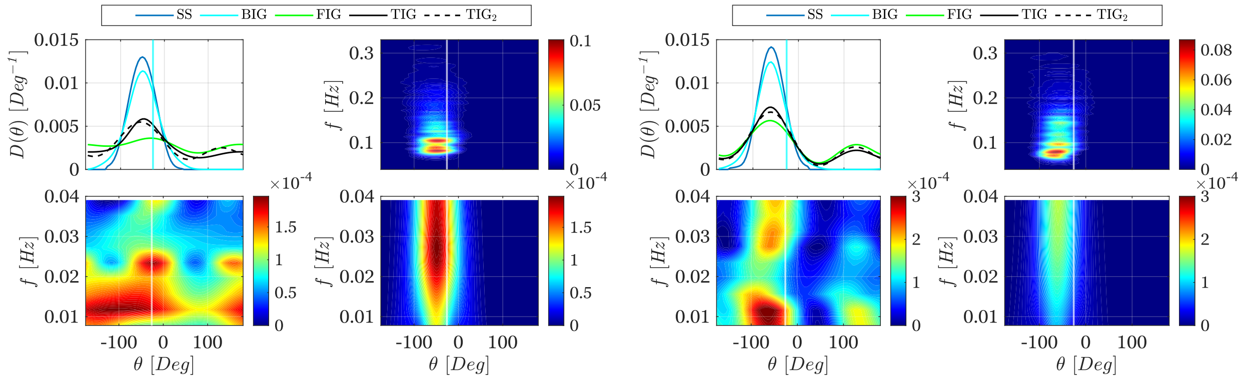

(c) storm 3, 20 Jan 2022. $H_{SS} = 3.06$ m, $H_{FIG} = 0.13$ m, $H_{BIG} = 0.09$ m.

(d) storm 4, 30 Jan 2022. $H_{SS} = 2.71$ m, $H_{FIG} = 0.13$ m, $H_{BIG} = 0.07$ m.

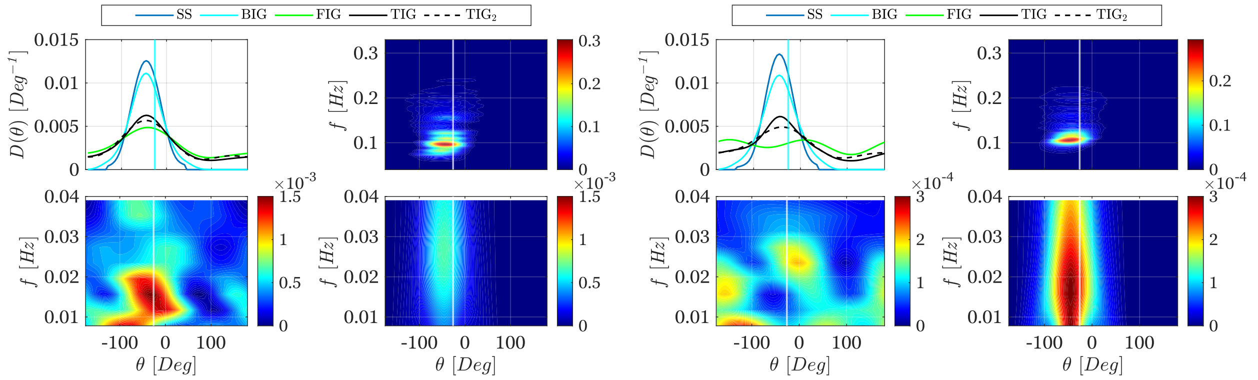

(e) storm 5, 31 Jan 2022. $H_{SS} = 4.62$ m, $H_{FIG} = 0.28$ m, $H_{BIG} = 0.18$ m.

(f) storm 6, 7 Feb 2022. $H_{SS} = 3.53$ m, $H_{FIG} = 0.13$ m, $H_{BIG} = 0.10$ m.

Figure 5.11: (Continue on next page)

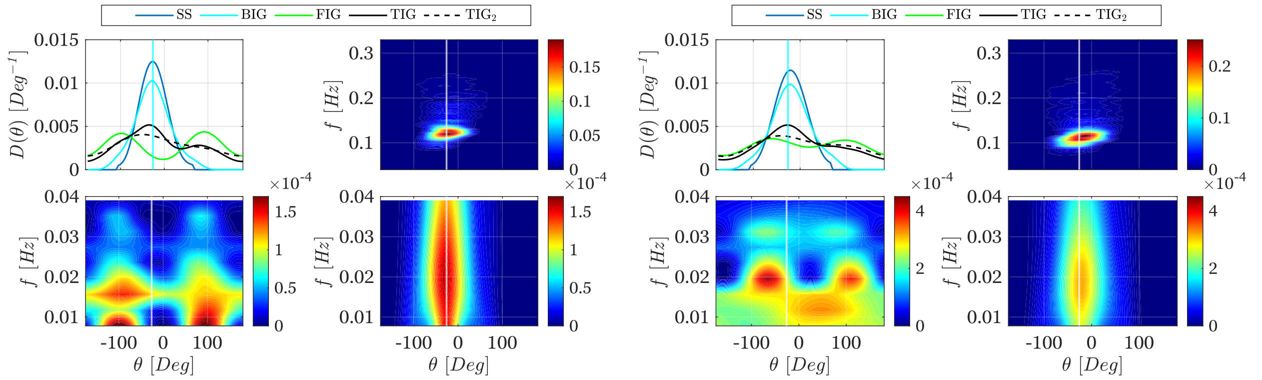

(g) storm 7, 17 Feb 2022. $H_{SS} = 3.13$ m, $H_{FIG} = 0.09$ m, $H_{BIG} = 0.09$ m.

(h) storm 8, 19 Feb 2022. $H_{SS} = 4.21$ m, $H_{FIG} = 0.18$ m, $H_{BIG} = 0.13$ m.

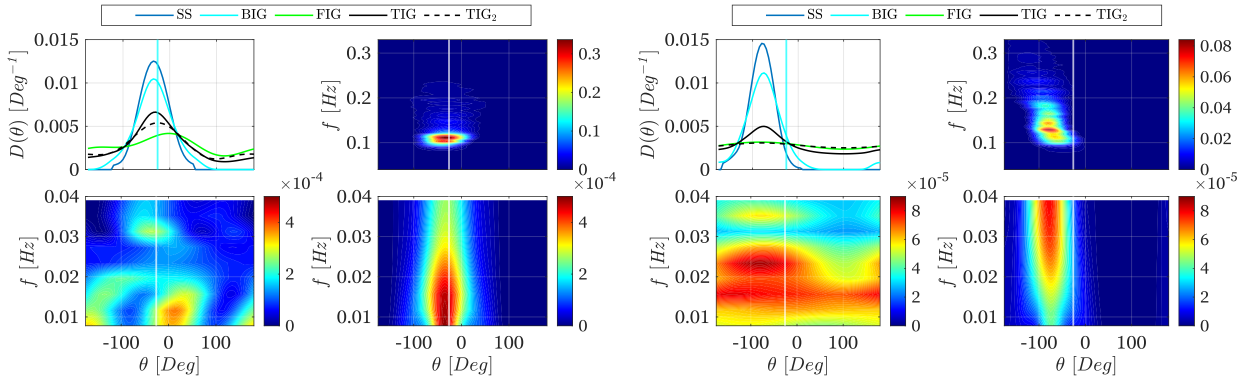

(i) storm 9, 21 Feb 2022. $H_{SS} = 4.02$ m, $H_{FIG} = 0.15$ m, $H_{BIG} = 0.13$ m.

(j) storm 10, 31 March 2022. $H_{SS} = 2.56$ m, $H_{FIG} = 0.10$ m, $H_{BIG} = 0.06$ m.

Figure 5.11: Directional properties of SS and IG wave during selected the peak of the storms (frame 1). (a)-(j): storm 1-10, the date of the storms are given in the caption of each figure. First row, first column: directional spreading functions of SS waves (solid blue), bound IG waves (BIG, solid cyan), free IG waves (FIG, solid green), total IG waves reconstructed by the new method (Matsuba et al., 2022, TIG, solid black), total IG waves reconstructed by the BDM method (TIG$_2$, dashed black). First row, second column: directional spectrum of SS waves. Second row, first column: directional spectrum of free IG waves. Second row, second column: directional spectrum of bound IG waves. Vertical lines indicate the shore-normal direction.

5.3.5 Frequency Distribution of Free IG waves

The directional properties of bound and free IG waves have been analyzed in the last section. Here, the frequency distribution of free IG waves during storms is discussed, and the empirical model of free IG waves suggested in Ardhuin et al. (2014) is applied for comparison. The empirical model defines a universal spectral shape and isotropic directional distribution, which have been applied in numerical studies as a source term of free IG waves to numerical models (e.g., Rawat et al., 2014; Rijnsdorp et al., 2021; Zheng et al., 2021):

$$E_{FIG} = 1.2\alpha_1^2 \frac{kg^2}{c_g\omega}\left(\frac{1}{4}H_{SS}T_{m0,-2}^2\right)^2 \frac{1}{\Delta_f}\min(1, 0.015/f)^{\beta}, \tag{5.1}$$

where α_1 is a dimensional tuning factor, a wide range of α_1 ($4.0 - 8.1 \times 10^{-4}\ \mathrm{s}^{-1}$) was applied in Ardhuin et al. (2014). c_g is the group velocity, and $T_{m0,-2}$ is the mean wave period. This equation can be split into two parts: $1.2\alpha_1^2 \frac{kg^2}{c_g\omega}\left(\frac{1}{4}H_{SS}T_{m0,-2}^2\right)^2$ determines the magnitude of each frequency components, and $\frac{1}{\Delta_f}\min(1, 0.015/f)^{\beta}$ represents the shape of the frequency distribution. It should be noted that $\frac{kg^2}{c_g\omega}$ in equation 5.1 is frequent-dependent, but it does not significantly differ within IG frequencies (Matsuba et al., 2022). Here, Δ_f was determined such that the integral of $\frac{1}{\Delta_f}\min(1, 0.015/f)^{\beta}$ is 1. The value of β defines the rate of decrease of free IG energy from high frequencies to low frequencies, it was set to -1.5 in Ardhuin et al. (2014).

At first, the magnitude of the observed free IG waves was analyzed. Again, 158 2-hour data segments from stormy days ($H_{SS} > 2.5$ m) collected at frame 1 were utilized (see Chapter 4.3.3). Figure 5.12 compares the magnitude of observed and empirical free IG wave variance E_{FIG}, the value of α_1 was set to $11 \times 10^{-4}\ \mathrm{s}^{-1}$ to give reasonable agreement between two variables. This shows the validity of the formation of equation 5.1, though limited, since the tuning factor α_1 must be assigned first. Moreover, the more significant deviation between observation and the empirical equation can be found as free IG energy increases, especially during peaks of the storms (red diamonds indicate the peaks of the 10 selected storms). This implies the empirical model of Ardhuin et al. (2014) may overestimate/underestimate the free IG energy observed in the field. The accuracy of the empirical model can then be investigated by examining the ratio r between $E_{FIG,Observations}$ and $E_{FIG,Ardhuin}$: it was found that the mean value of r is around 0.86, which means a general overestimation of the empirical model. Moreover, the maximum value $r_{max} = 1.76$, and the standard deviation $\sigma_r = 0.23$, indicating the highly varying relation between the observed and the empirical values. In addition, to get the best fits for the data points with significant deviations in Fig 5.12, α_1 must be varied significantly as well($8 - 14 \times 10^{-4}\ \mathrm{s}^{-1}$).

Next, the spectral shape of free IG waves is analyzed. Frequency distributions of free IG waves at peaks of the 10 selected storms are normalized and plotted in Figure 5.13. The normalized term $\frac{1}{\Delta_f}\min(1, 0.015/f)^{\beta}$ in equation 5.1 was added for comparison. Highly varying frequency distributions of free IG waves are found for these storms, and the empirical spectral shape of

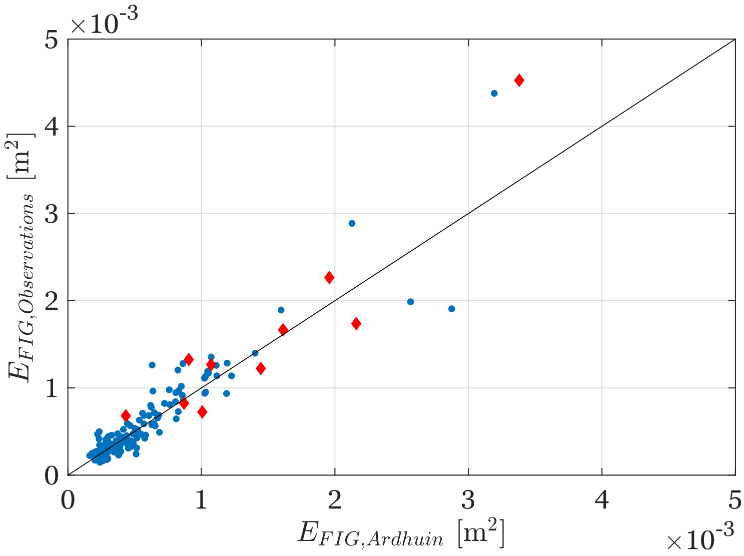

Figure 5.12: Magnitude of observed (based on Matsuba et al., 2022) and empirical (based on Ardhuin et al., 2014) free IG wave variance E_{FIG}, for 158 stormy events (frame 1). Red diamonds indicate the peaks of the 10 selected storms.

Ardhuin et al. (2014) seems unable to model any of these individual storms. However, the mean frequency distribution of the observed storms shows a similar trend to the empirical distribution. Still, the empirical formula overestimates the IG energy distribution at low IG frequencies ($0.005 - 0.02$ Hz), while underestimating it at high IG frequencies ($0.02 - 0.04$ Hz). Interestingly, this issue may be solved by simply modifying the value of β in equation 5.1, a good fit between the observed mean and the empirical formula was found by altering β to -0.9. It may be concluded that the empirical formula of Ardhuin et al. (2014) can reveal the collective nature of the spectral shape of free IG waves during storms, though relevant parameter(s) used in equation 5.1 must be calibrated.

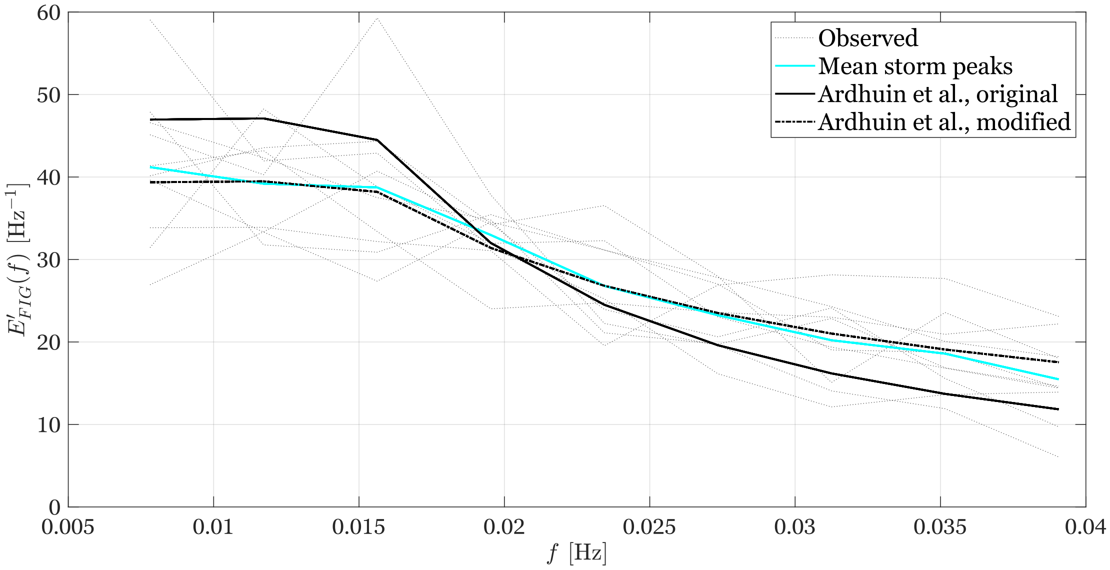

Figure 5.13: Normalized frequency distributions of free IG waves (frame 1). Dotted black lines correspond to the peaks of the 10 selected storms, and the solid cyan line indicates their mean. The solid black line indicates the frequency distribution proposed in Ardhuin et al. (2014), $\beta = -1.5$, and the dash-dotted black line is the modified frequency distribution based on Ardhuin et al. (2014), $\beta = -0.9$.

5.3.6 Temporal Variation of the Directional Spectra

In this section, the temporal variation of the directional spectra during the storm is examined. The largest storm (storm 5, see Table 5.1) occurred on 31 Jan 2022. It started in the early morning, reached its peak at noon, and ceased in the early morning on 1 Feb 2022. Five data files were selected; their information can be seen in Table 5.3. The mean direction of SS waves during the storm changed significantly. Starting from West (-13.86°), the storm changed its mean direction to Northwest (-45.71°) at its peak, and varied slightly until the storm ended.

As can be seen from Figure 5.14, the normalized reconstructed directional spectra of free IG waves show clear peaks during the storm (storm 3,4,5), while nearly isotropic directional distribution can be found for calm conditions (Cases 1 and 5). As the storm evolved, the peak direction of the free IG waves was altering as well. In case 2, free IG waves show its peak at around 10°, while SS waves were traveling from the other side of the shore-normal direction. The directions of free IG and SS waves coincided in case 3. As for case 4, multiple free IG wave energy lumps can be observed, ranging from $0° - 180°$.

Figures 5.15 and 5.16 further confirm the conclusion above. Storms 4, 5, 7, 8, and 9 have distinguishable directional peaks of free IG waves, and $H_{SS} > 2$m seems to be able to serve as an indicator. However, no clear evidence indicates any relationship between the direction of SS and free IG waves. Furthermore, no clear free IG peaks can be found for other selected storms, since the directioanl spectra of free IG waves of these storms were nearly evenly distributed even during their peaks (see Figure 5.11).

Case number	Time of Observation	H_{SS} [m]	H_{TIG} [m]	H_{BIG} [m]	H_{FIG} [m]	θ_{mean} [Deg]	σ_{θ} [Deg]
1	04:00-06:00 31 Jan 2022	2.50	0.08	0.05	0.06	-13.86	23.93
2	10:00-12:00 31 Jan 2022	4.01	0.24	0.16	0.18	-34.35	25.40
3	14:00-16:00 31 Jan 2022	4.62	0.34	0.18	0.28	-45.71	24.40
4	18:00-20:00 31 Jan 2022	3.78	0.24	0.15	0.20	-55.72	26.11
5	02:00-04:00 1 Feb 2022	2.01	0.07	0.02	0.06	-47.61	30.19

Table 5.3: Overview of the selected events during storm 5 (frame 1).

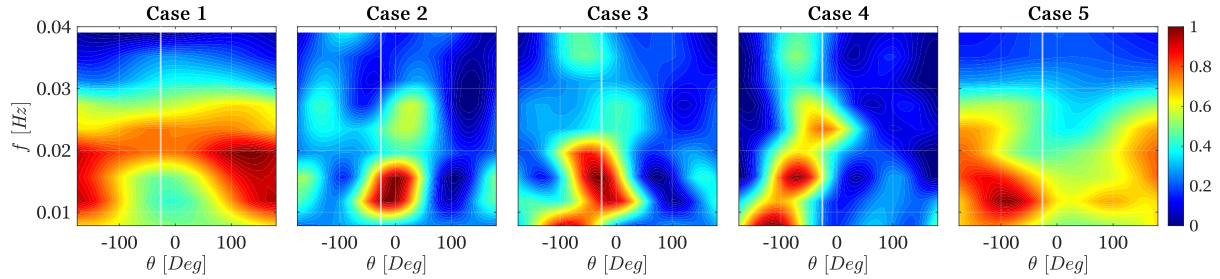

(a) Normalized directional spectra of free IG waves.

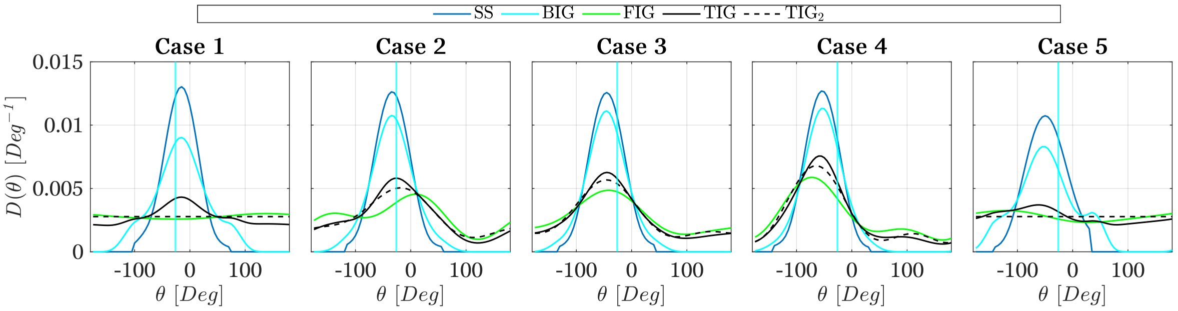

(b) Directional spreading functions.

Figure 5.14: Time variation of the directional spectra (frame 1). (a): Normalized directional spectra of free IG waves; each spectrum is normalized by its maximum value. Vertical lines indicate the shore-normal direction. (b): Directional spreading functions of SS waves (solid blue), bound IG waves (BIG, solid cyan), free IG waves (FIG, solid green), total IG waves reconstructed by the new method (Matsuba et al., 2022, TIG, solid black), total IG waves reconstructed by the BDM method (TIG$_2$, dashed black). Information of cases 1-5 is given in Table 5.3.

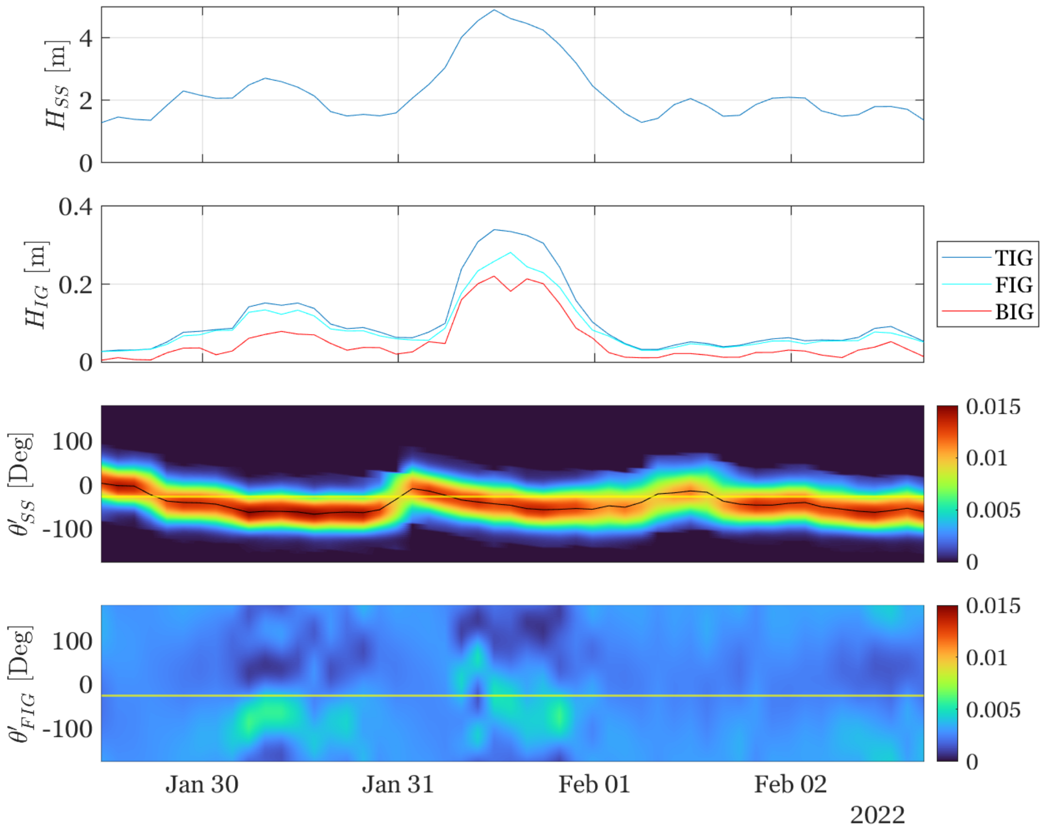

Figure 5.15: From top to bottom: temporal variation of SS wave height H_{SS}, IG wave height H_{IG} (TIG, total IG waves; FIG, free IG waves; BIG, bound IG waves), directional spreading function for SS waves θ'_{SS}, and free IG waves θ'_{FIG}, from 30 Jan 2022 to 2 Feb 2022 (frame 1). Storm 4 occurred on 30 Jan 2022, and storm 5 occurred on 31 Jan 2022.

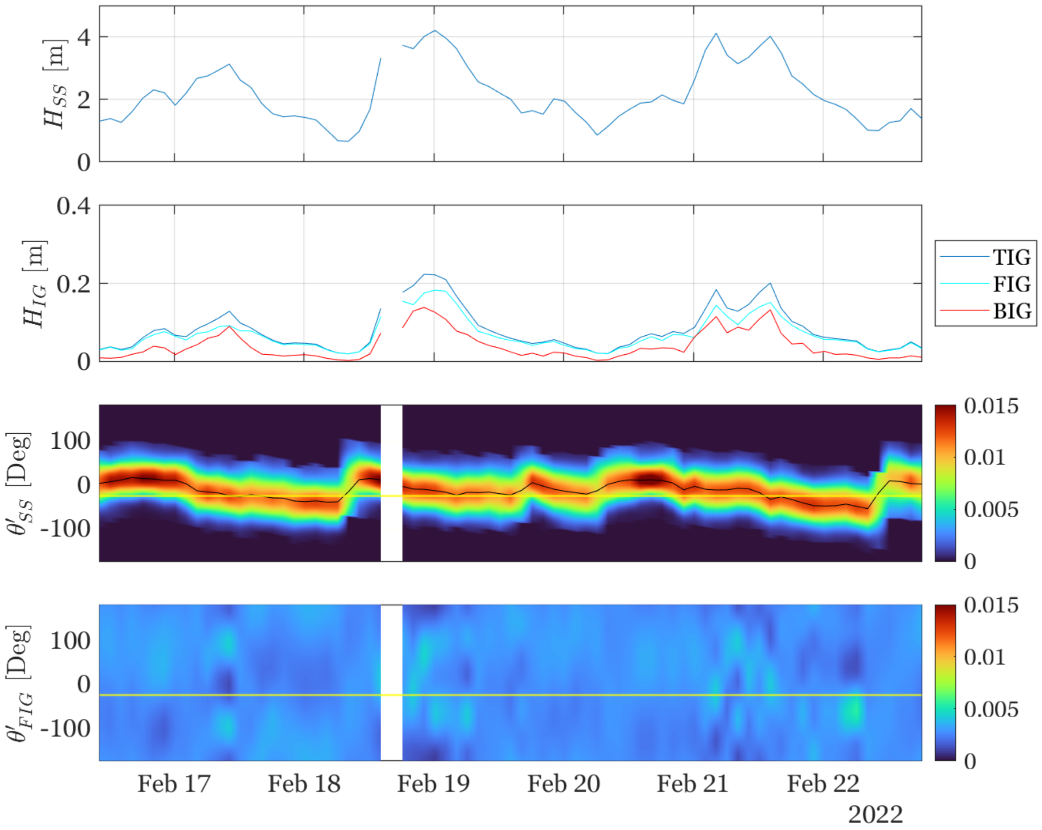

Figure 5.16: From top to bottom: temporal variation of SS wave height H_{SS}, IG wave height H_{IG} (TIG, total IG waves; FIG, free IG waves; BIG, bound IG waves), directional spreading function for SS waves θ'_{SS}, and free IG waves θ'_{FIG}, from 17 Feb 2022 to 22 Feb 2022 (frame 1). The omitted data indicates discarded data file. Storms 7, 8, and 9 occurred on 17, 19, and 21 Feb 2022, respectively.

5.3.7 Spatial Variation of the Directional Spectra

The spatial variation of the IG and SS wave field was examined by reconstructing the directional spectra of total IG and SS waves for frames 1 and 2.

An example is given for storm 2 on 5 Jan 2022, see Figure 5.17. Here, the directional spectra of total IG and SS waves are reconstructed using the method of Matsuba et al. (2022) and the BDM method for frames 1 and 2, respectively. An overview of the wave conditions at both frames is given in Table 5.4.

SS wave breaking can be identified by the decreased H_{SS} and increased H_{SS}/h at frame 2. This also results in decreased R_{BIG}, but bound IG wave shoaling was still significant in this case.

The influence of free IG waves is visible when comparing the directional spectra of total IG waves in Figures 5.17. Note the differences in the color bars. Broader directional spreading of total IG waves can be found, compared to that of bound IG waves at frame 1 (see storm 2 in Figure 5.11). Low frequency $f < 0.15$ Hz free IG waves are presented in around $-130°$ direction at frame 1, while they disappear at frame 2 (note the different scales of the two figures).

Narrower SS waves were found at frame 2, leading to narrower directional distribution of bound IG waves and stronger nonlinear interaction between SS waves. More contribution of bound IG waves can be expected at frame 2 (Compare the directional spreading function TIG_2 at frames 1 and 2), though SS waves were breaking during the peak of storm 2 (see Figure 5.2).

Frame	H_{SS} [m]	H_{TIG} [m]	H_{BIG} [m]	H_{FIG} [m]	R_{BIG}	H_{SS}/h
1	3.60	0.19	0.12	0.15	0.39	0.26
2	3.36	0.33	0.18	0.28	0.30	0.39

Table 5.4: Overview of the wave conditions at frames 1 and 2.

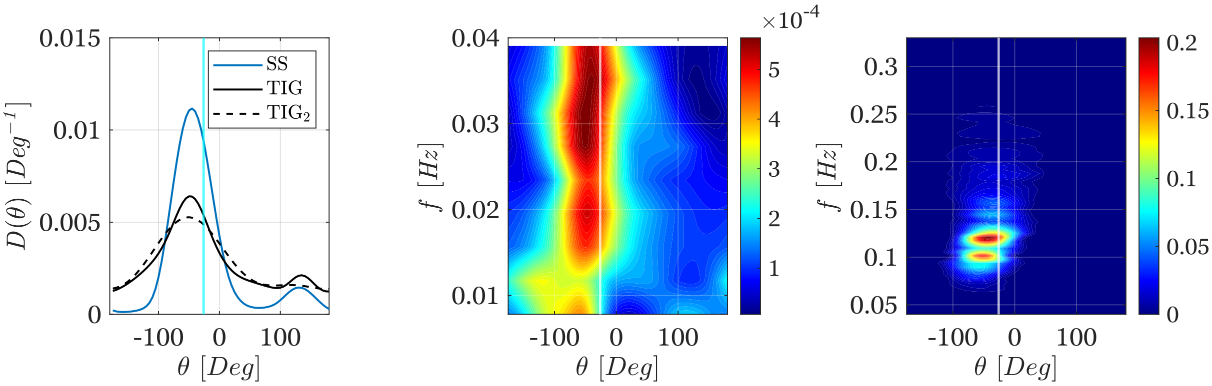

(a) Frame 1

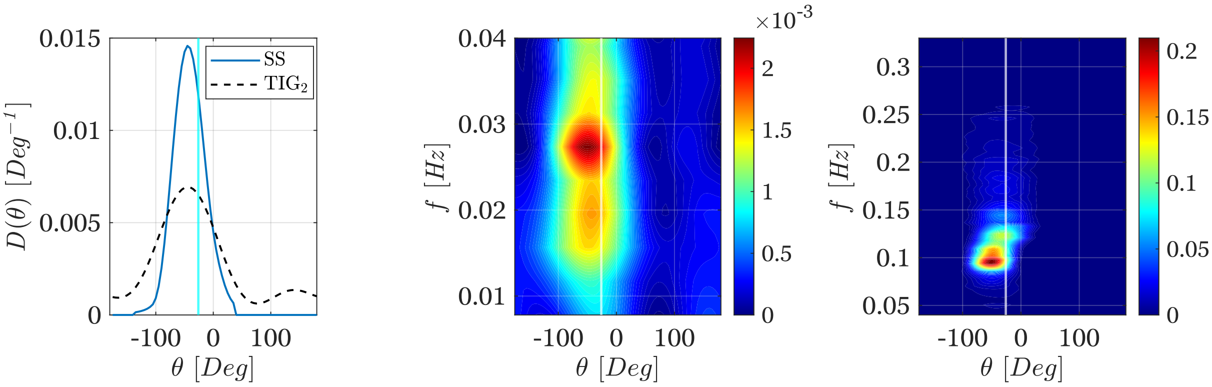

(b) Frame 2

Figure 5.17: Spatial variation of directional spectra of SS and IG waves at (a): frame 1, and (b): frame 2. Left panel: directional spreading functions of SS waves (solid blue), total IG waves reconstructed by the new method (Matsuba et al., 2022, TIG, solid black), total IG waves reconstructed by the BDM method (TIG$_2$, dashed black). Middle panel: directional spectra of total IG waves. Right panel: directional spectra of SS waves. Vertical lines indicate the shore-normal direction. Time of observation: 10:00-12:00, 5 Jan 2022.

6 Discussion

6.1 Bound IG Wave Height Estimation with Bispectral Analysis

As introduced in Chapter 4.3.2, it is possible to estimate bound IG wave height with bispectral analysis using only pressure head signal (see equations 4.18 - 4.23). The bound IG wave height is proportional to the bicoherence (see equation 4.19). This method is based on the assumption that $\alpha_{ii} = 1$ (see equation 4.21), as introduced in Herbers et al. (1994). Many researchers have applied this simple method to calculate bound IG wave height (e.g., Herbers et al., 1995; Ruessink, 1998a; Mendes et al., 2020; Mahmoudof and Siadatmousavi, 2020; Mahmoudof et al., 2021). Moreover, de Wit et al. (2020) adjusted this method to estimate bound wave height for super harmonics.

According to Herbers et al. (1994), the estimated bound IG wave height has a negative bias of less than 40% due to this assumption, since $\alpha_{ii} > 1$ in the field. The bias is owing to variations of the nonlinear interaction coefficient over wave triads (Ruessink, 1998a). Nevertheless, the bias was considered low, and the estimated bound IG wave height reasonably measures the bound IG energy contribution.

To further examine the validity of the assumption of $\alpha_{ii} = 1$, a detailed examination was conducted using the data set described in Chapter 4.2. A total of 158 2-hour data segments collected from stormy days ($H_{SS} > 2.5m$) at frame 1 were used to check the bias caused by the assumption of $\alpha_{ii} = 1$. There are two approaches to mimic the calculation as was done in Herbers et al. (1994). First, the pressure head signal can be used without linear correction and was assumed to be collected on the sea bed, the pressure head derived spectrum was noted as $S_p(f,\theta)$. Second, the surface elevation signal can be used to obtain the directional spectrum of SS waves $S(f,\theta)$, and this spectrum needs to be converted according to linear theory:

$$S_c(f,\theta) = S(f,\theta)\left(\frac{1}{\cosh(kh)}\right)^2. \tag{6.1}$$

The converted spectrum $S_c(f,\theta)$ can also be used as a pressure head derived directional spectrum.

The nonlinear interaction coefficients for different signals are summarized in Appendix E. Since the pressure head derived nonlinear interaction coefficient (D in equation 4.22) was used in Herbers et al. (1994), the same interaction coefficient was selected for this investigation (see equation

E.5).

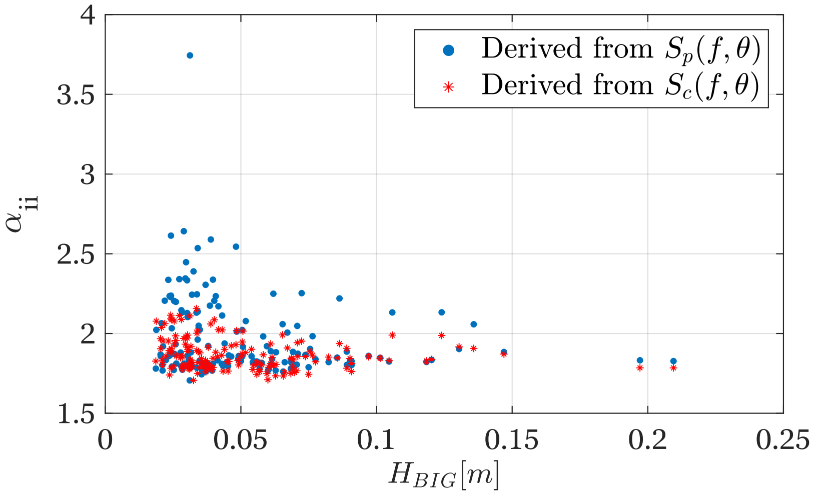

Figure 6.1: α_{ii} versus bound IG wave height estimated by bispectral analysis. Blue dots indicate α_{ii} calculated with pressure head derived SS wave spectra, and red asterisks indicate α_{ii} calculated with surface elevation derived SS wave spectra using linear corrections.

As can be seen in Figure 6.1, the results for both approaches indicate α_{ii} is constantly higher than 1.7, which is much higher than the values suggested in Herbers et al. (1994). The mean values of αii derived from $S_p(f,\theta)$ and $S_c(f,\theta)$ were approximately 1.8 and 2, respectively. In addition, the values of α_{ii} derived from $S_p(f,\theta)$ appear to be less stable, compared to those derived from $S_c(f,\theta)$. The higher values (> 2) of α_{ii} often occur for the first approach and when the bound IG wave height is relatively low. The second approach, on the other hand, gives generally lower values of α_{ii}.

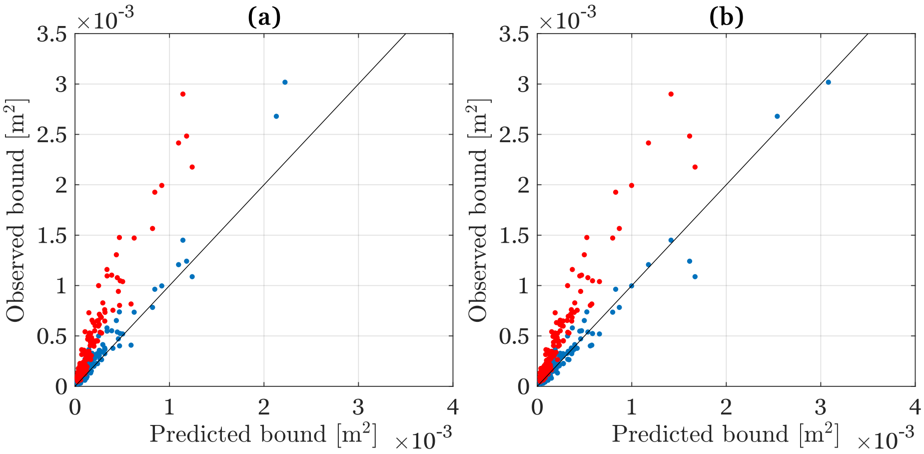

Figure 6.2: Predicted (equation 2.6) versus observed (bispectral analysis) frequency-integrated bound IG energy. (a): Predicted values derived from $S_p(f,\theta)$. (b) Predicted values derived from $S_c(f,\theta)$. Blue dots: actual results. Red dots: modified results, observed values are multiplied by a factor of 2.

	r_{max}	r_{min}	$\overline{r}$	σ_r
$S_p(f,\theta)$	2.59	0.53	1.31	0.4
$S_c(f,\theta)$	2.37	0.50	1.11	0.33

Table 6.1: Statistics of r.

The above analysis suggests a correction factor of around 2 be applied to α_{ii}. Interestingly, comparisons between predicted and observed bound IG energy does not show the observed bound IG energy is underestimated by a factor of 2 (see Figure 6.2). The original predicted and the observed bound IG energy agrees well. Additionally, comparing Figures 6.2 (a), (b) suggest that $S_c(f,\theta)$ leads to a better fit to the observed bound IG energy. The predicted bound IG energy derived from $S_c(f,\theta)$ seems more appropriate to apply. This is confirmed by analyzing the ratio r = observed value/ predicted value, as summarized in Table 6.1. The maximum, minimum, mean, and standard deviation of r are given for the case of $S_p(f,\theta)$ and $S_c(f,\theta)$. r for the case of $S_c(f,\theta)$ is less scattered and has a lower mean value, implying less deviation between the observed and predicted values.

The analysis according to Figures 6.1 and 6.2 implies contradictory conclusions, the former draws the necessity to apply a correction factor to α_{ii}, while the latter indicates no such need. This issue may suggest that the assumption of α_{ii} in Herbers et al. (1994) is oversimplified, as the value of α is highly related to the interaction coefficient Ω, which depends on the directional distribution of SS waves. On the other hand, the directional distribution of SS waves also determines the predicted bound IG energy through equation 2.6. Confusingly, bound IG energy derived from Hasselmann (1962) (equation 2.6) can be substituted to N_2 (equation 4.22), which is a part of the formulation of α_{ii}. Therefore, although equation 4.19 has been widely used with $\alpha_{ii} = 1$ to calculate the 'observed' bound IG energy, the assumption of $\alpha_{ii} = 1$ is partly proposed based on predicted bound IG energy derived from Hasselmann (1962). It is still not fully understood why α_{ii} in our case is higher than that of in Herbers et al. (1994). More investigations on the theoretical basis of the assumption of $\alpha_{ii} = 1$ are desired.

6.2 Directional Spectra Reconstruction of IG Waves with Conventional Methods

For directional spectra reconstruction of IG waves at frames 2 and 3, the conventional BDM method was utilized. It was suggested in Matsuba et al. (2022) that their new method is not applicable in shallow waters ($h < 10$m), as Hasselmann's theory does not hold in such conditions. This is confirmed by conducting the same validation procedure, as presented in Chapter 5.3.1. For frame 2 (water depth around 8.5m), a total of 153 2-hour data segments from stormy days ($H_{SS} > 2$m) were chosen to examine the applicability of the method of Matsuba et al. (2022). Figure 6.3 shows that I_B and I_S only show reasonable agreement when their magnitudes are relatively low. Comparing Figure 5.8 and Figure 6.3 confirms that the method of Matsuba et al.

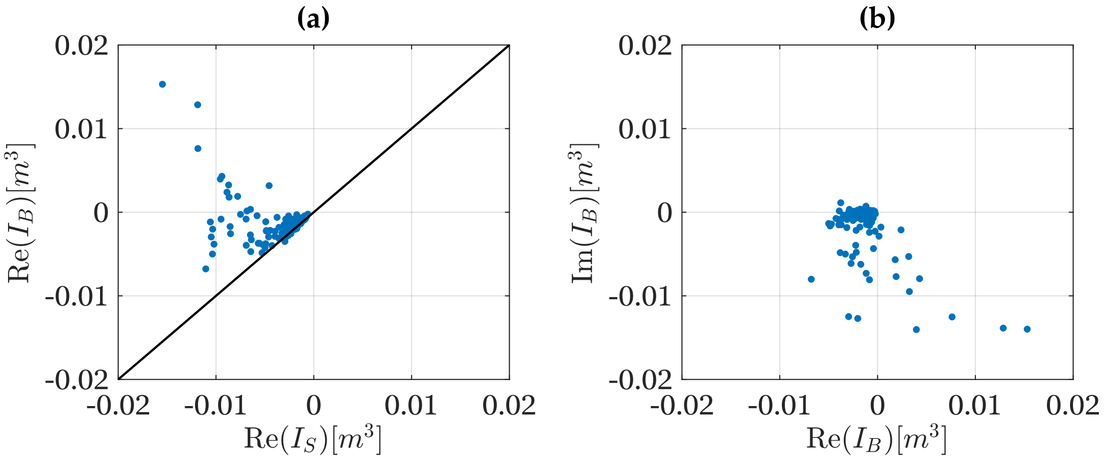

Figure 6.3: Results of cross-bispectral analysis for 153 stormy events (frame 2). (a), (b): Evaluation of pressure head signal with $B_{p,\eta,\eta}$. (a): $\mathrm{Re}(I_S)$ versus $\mathrm{Re}(I_B)$. (b): $\mathrm{Re}(I_B)$ versus $\mathrm{Im}(I_B)$.

(2022) can not be applied if the water depth is too shallow ($h < 10$m) or the bottom is too steep (e.g., $> 1/100$ at frame 2).

Though the directional spectra of free or bound IG waves cannot be obtained at shallow frames 2 and 3, bound and free IG waves behave similarly in shallow water. van Essen et al. (2013) states that the velocity difference between bound and free IG waves approaches zero as water depth decreases, hence motivating their use of the conventional method to reconstruct directional spectra of IG waves. This is true, however, for directional spectra reconstruction methods, wave velocity is not the fundamental factor to be considered in shallow water ($h < 10$m), first-order and second-order transfer functions get close (Matsuba et al., 2022), thus, bound IG waves should behave as if they were free. Therefore, conventional methods can be applied to reconstruct the directional spectra of IG waves in shallow waters, since the transfer functions for first-order (free) and second-order (bound) IG waves are close to each other.

6.3 Diverse Pattern of Free IG Waves

The diverse pattern of the reconstructed directional spectra of free IG waves, as presented in Chapter 5.3.4, is not easy to explain. Seaward propagating free IG waves, as observed in previous literature (Herbers et al., 1995), do not dominate the directional spectra in most of the storms in this study (see Figure 5.11). Besides the influence of edge waves, the directional spectra of the local free IG wave field may be affected by free IG waves from other coasts (Rijnsdorp et al., 2021).

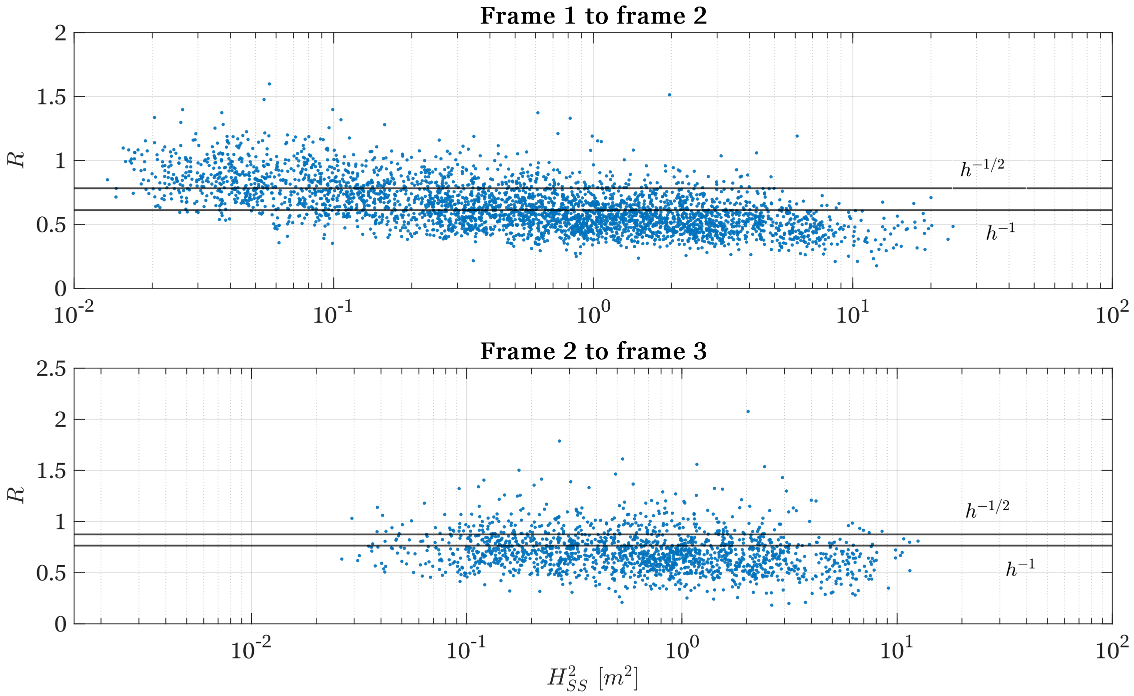

Figure 6.4: The ratio R of free IG wave energy (represented by H_{FIG}^2) at different frames, versus SS wave energy (represented by H_{SS}^2). The theoretical lines are for leaky waves ($h^{-1/2}$) and edge waves (h^{-1}), respectively.

6.3.1 Edge Waves and Leaky Waves

The energy of non-breaking free waves propagating perpendicular to a gently sloping beach with no alongshore variation should be proportional to $h^{-1/2}$, according to Eckart (1951). In contrast, the integrated edge wave energy decays away from the coast, following h^{-1}. Figure 6.4 shows that the ratio R of free IG wave energy at different frames are only weakly dependent on SS wave energy. For frame 1 to frame 2, $h^{-1/2} = 0.78$, and $h^{-1} = 0.62$. The observed values of R vary dramatically between 0.2 and 1.6. However, R decreases as H_{SS}^2 increases, this indicates that more free waves were trapped during storms (Herbers et al., 1995). For frame 2 to frame 3, $h^{-1/2} = 0.87$, and $h^{-1} = 0.76$. No clear trend of R can be found here, possibly due to the comparable contribution of leaky and edge waves between frames 2 and 3. The theoretical lines presented here appear unable to indicate the dominance of leaky or edge waves, possibly due to their oversimplified assumptions. Alongshore measurements should be conducted to understand edge and leaky wave distributions fully. Moreover, incident free IG waves from other coasts might also 'contaminate' the patterns shown in Figure 6.4, see next section.

6.3.2 Free IG Waves from Remote Sources

It should be noted that the North Sea is relatively small compared to the Atlantic Ocean or the Pacific Ocean, where many previous observations were conducted (e.g., Herbers et al., 1995). Rijnsdorp et al. (2021) has numerically shown that a significant part of the IG waves can be attributed to free IG waves originating from nearby shorelines. When a storm hit the Dutch coast, likely, other coasts around the North Sea were also experiencing storms. Thus, the local free IG wave field can be influenced by incident free IG waves that radiate away from other coasts, leading to highly varying directional spectra. Figure 6.5 shows the spatial distribution of significant wave height H_{SS} (obtained from the global ECMWF ERA5 reanalysis, see Hersbach et al., 2020) over the North Sea during the peaks of 8 selected storms (as introduced in Table 5.1). These data were available every 1 hour with a 0.5° resolution. The spatial distributions of H_{SS} during storms show varying characteristics of different storms. It appears that when the storm spreads over the whole North Sea, e.g., storm 2, 3, 6, and 9 (see Figure 6.5 (a), (b), (e), and (h)), the corresponding reconstructed directional spectra of free IG waves have very broad distribution or multiple energy lumps (see Figure 5.11 (b), (c), (f), and (i)). Apparent incident free IG waves observed in Figure 5.11 (d) and (e) correspond to Figure 6.5 (c) and (d). Here, the storms only hit one side of the North Sea basin, while the other side remained calm. Additionally, storms 7 and 8 (see Figure 6.5 (f) and (g)) attacked mostly the Dutch/German coasts, while the free IG wave field at frame 1 showed two directional peaks (see Figure 5.11 (g) and (h)).

The attempt to link the spatial distribution of H_{SS} in the North Sea and the reconstructed directional spectra of free IG wave off the Dutch coast is still tentative, and no concrete conclusion should be made here. Therefore, numerical investigations similar to Rijnsdorp et al. (2021) are recommended to help further clarify the relationship between local and regional free IG wave fields.

6.3.3 Inspirations for Numerical Modelling

As introduced in Chapter 1.2.2, most numerical models only consider bound IG waves at the offshore boundary. The energy and directional properties of free IG waves are neglected. Take the location of frame 1 as a possible offshore boundary, it has been found that free IG waves always dominate the total IG wave field during storms (see Table 5.1). Therefore the energy of free IG energy should be taken into account when determining such an offshore boundary. For directional properties of IG waves, it is easy to determine the directional spectra of bound IG waves if the directional spectra of SS waves are available. However, the directional spectra of free IG waves are highly varying. It is unclear yet how to apply a local directional boundary for free IG waves, considering the possible contribution of free IG waves from other coasts. A provisional approach is to apply the empirical model of Ardhuin et al. (2014), and an isotropic directional distribution of free IG waves may be used, if no observation data is available.

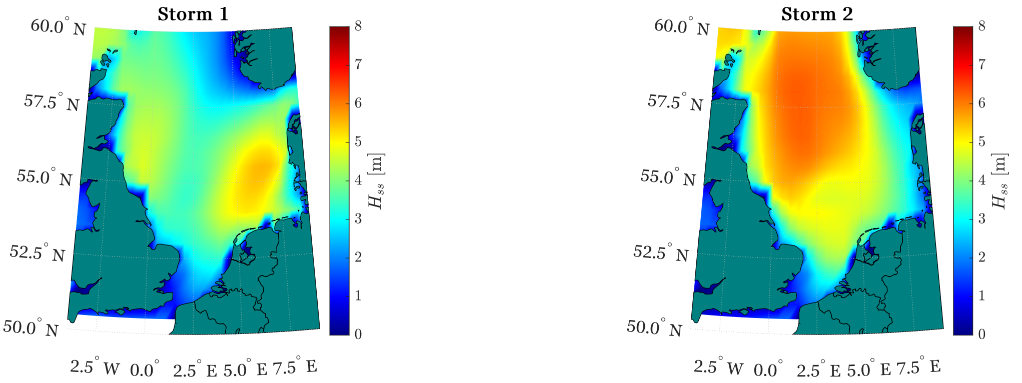

(a) storm 1, 1 Dec 2021.

(b) storm 2, 5 Jan 2022.

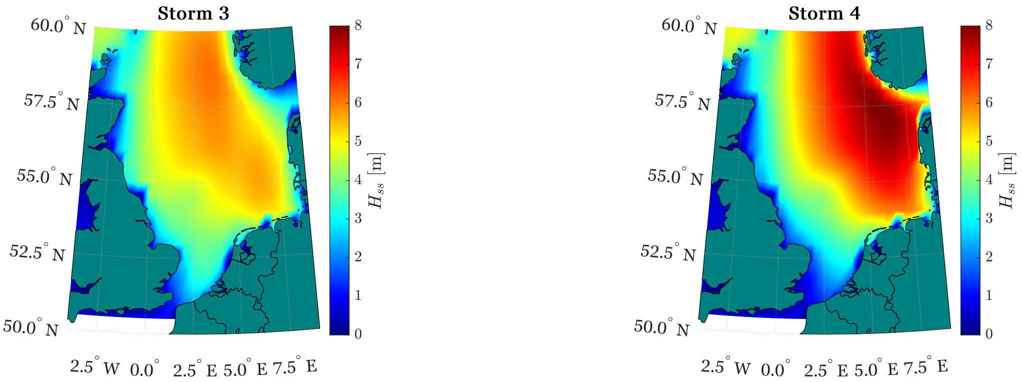

(c) storm 3, 20 Jan 2022.

(d) storm 4, 30 Jan 2022.

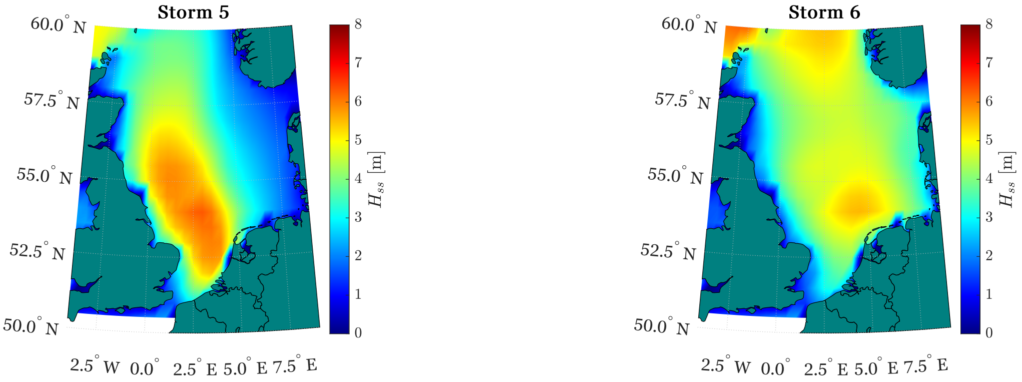

(e) storm 5, 31 Jan 2022.

(f) storm 6, 7 Feb 2022.

Figure 6.5: (Continue on next page)

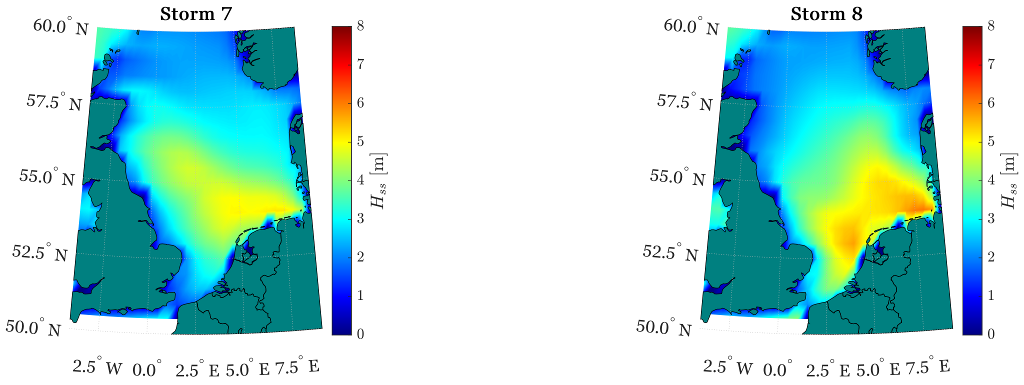

(g) storm 7, 17 Feb 2022.

(h) storm 8, 19 Feb 2022.

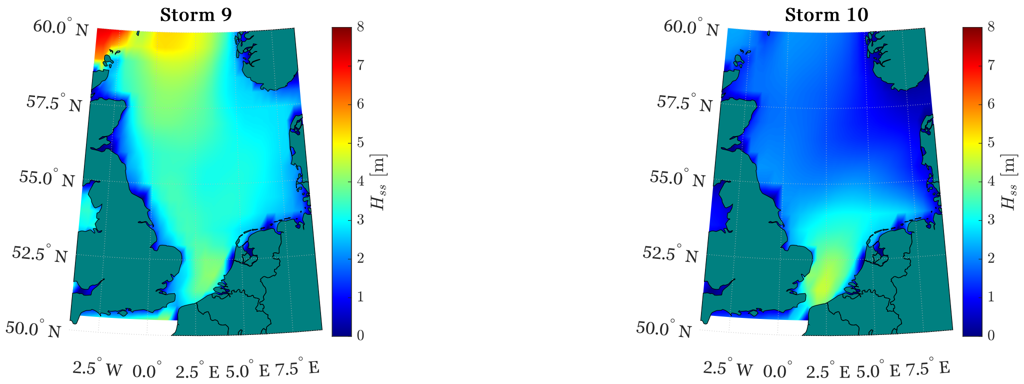

(i) storm 9, 21 Feb 2022.

(j) storm 10, 31 March 2022.

Figure 6.5: Spatial distribution of H_{SS} over the North Sea during the selected storms.

7 Conclusions and Recommendations for Future Research

7.1 Conclusions

This study investigated the temporal and spatial variation of IG waves in the North Sea in intermediate water depth ($\sim$ 6-14 m). IG energy correlation, shoaling, relative contribution of bound components, and directional properties were analyzed using field data collected off the Dutch coast. The research questions for this thesis, given in Chapter 3, are repeated and discussed here.

1. *What offshore parameter does IG energy correlate to the most?*

   In general, IG wave height H_{IG} is highly correlated with SS wave height H_{SS}, since all the events with high IG wave heights (say, $H_{IG} > 0.12$m) were storms. A higher correlation was found between H_{IG} and swell wave height H_{Swell}, while the highest correlation was found between H_{IG} and $H_{SS}T_p^2$, which is proportional to offshore energy flux, as described in Inch et al. (2017). The use of $H_{SS}T_p^2$ gives a good measure of H_{IG}, especially when H_{IG} is high. This study have confirmed that $H_{SS}T_p^2$ provides a very high correlation (R^2 up to 0.94) of H_{IG} in intermediate water depth. Both bound and free IG wave energy correlates well with swell energy, while free IG waves show a weaker dependency than bound IG waves.

2. *How does the IG energy change at different water depths under different wave conditions? And what is the proportion of bound and free IG waves?*

   The IG waves observed in the field consisted of bound and free components. Higher total IG energy can be expected during more intense storms at shallower locations, and the growth rate of total IG wave heights lies between the shallow water equilibrium solution (Longuet-Higgins and Stewart, 1962) for bound waves and the Green's Law for free waves.

   The relative contribution of bound IG wave energy is correlated with SS wave energy (R_{BIG} up to 0.76), provided that storms were not intense enough to induce SS wave breaking. During intense storms, the group structure of SS waves may be deconstructed due to breaking, hence the relative contribution of bound IG waves decreases.

3. *How to reconstruct the directional spectra of bound and free IG waves, and how do they relate to the directional spectra of SS waves?*

To reconstruct directional spectra of free and bound IG waves (at frame 1, the most offshore location in this field experiment) separately, cross-bispectral analysis was conducted to show the validity of the new method of Matsuba et al. (2022). The applicability of this new method was then broaden to shallower water depths, compared to the water depths suggested in Matsuba et al. (2022).

It was shown that bound IG waves have a broader directional distribution than the SS waves, and the peak directions of bound IG and SS waves are always the same. Free IG waves, on the other hand, have shown diverse directional properties during different storms. A clear relation of the directional properties between free IG and SS waves is absent, which may indicate that edge waves and incident free IG waves originating from remote coasts can highly influence the directional spectra of the observed free IG wave field.

4. *How do the directional spectra of bound and free IG waves change temporally and spatially?*

   During calm conditions, bound IG waves contributed insignificantly to the total IG wave field, and nearly evenly distributed free IG waves were often found. As storms reached their peaks, both IG and SS wave heights increased, and free IG waves may show their peak(s).

   Narrower directional spreading of SS waves was observed at shallower frames, indicating more contribution of bound IG waves.

7.2 Recommendations for Future Research

The diverse directional properties of free IG waves show uncertainties as it may be influenced by multiple factors, including edge waves and incident free IG waves. To confirm the observed directional spectra of free IG waves, detailed numerical experiments are recommended since numerical modeling is not influenced by possible poor-quality field data. Furthermore, alongshore observations at the field location are desired to examine the complex pattern of edge waves, which adjacent structures may influence (e.g., the breakwater at De Pier Hoek van Holland, Southeast of the field location).

A Unrealistic Estimation of Surface Elevation Derived Spectra at Low Frequencies

For Signature ADCPs attached at frames 1 and 2, Acoustic Surface Tracking (AST, see Nortek (2022a) for more information) signals were used as surface elevation signals. The advantage of this is that the AST signal gives a direct record of the surface elevation, hence no depth attenuation should be considered. Therefore, the AST derived spectra are helpful when calculating wave energy at high SS frequencies, particularly in deep water. Despite this advantage, it was found that the AST derived spectra often had non-physical values at IG frequencies, leading to wrong IG wave height calculation.

Taking pressure head derived IG wave heights as reference values, Figure A.1 demonstrated that the AST derived IG wave heights were constantly overestimated. The overestimation seems more severe during storms, as the IG wave motions were intense, so more errors may be introduced. Figure A.2 shows an example of a wrongly estimated AST spectrum at low frequencies.

The reason for this issue is not fully understood, a close look at the time series of the AST signals might be helpful, especially during storms. As shown in Figure A.3, the original AST signal drops between 11:14-11:16 on 21 Feb 2022, which is non-physical. The middle and lower panel of Figure A.3 confirmed that the signal drop was considered IG motion instead of SS motion.

Therefore, an unreasonable high value of the IG wave height was obtained. Although the drop showed above partly explains the overestimated IG wave heights, the AST signals do not always have apparent drops throughout the field experiment. Further investigation on the quality of the AST signals is required.

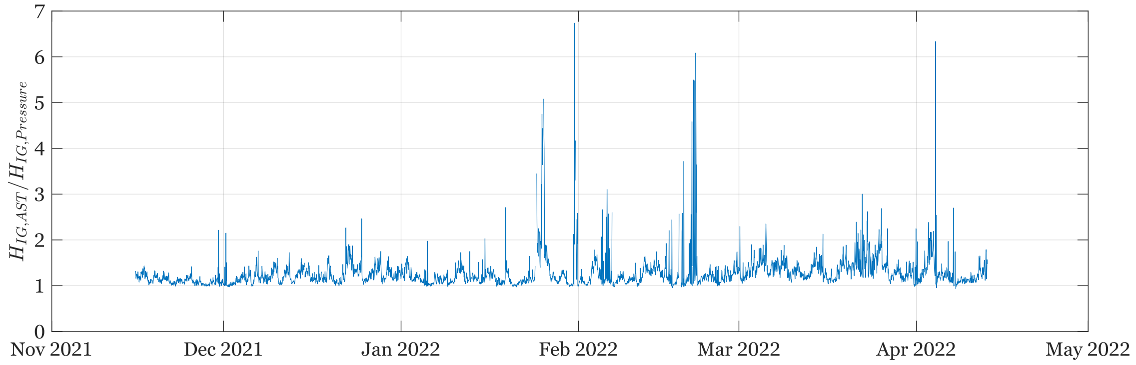

Figure A.1: Ratio between AST derived IG wave height and pressure head derived IG wave height (frame 1).

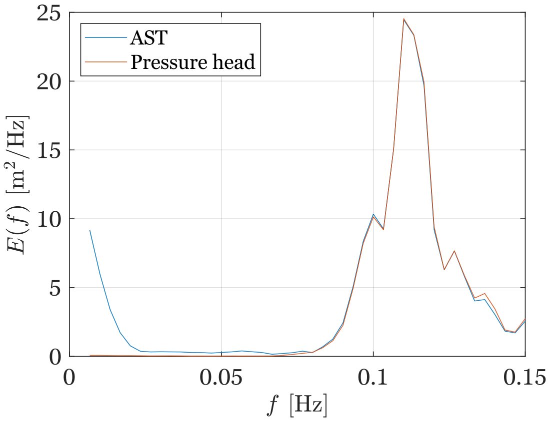

Figure A.2: Variance density spectrum E (frame 1), derived from AST signal (blue) and pressure head signal (red), at 11:00-12:00, 21 Feb 2022.

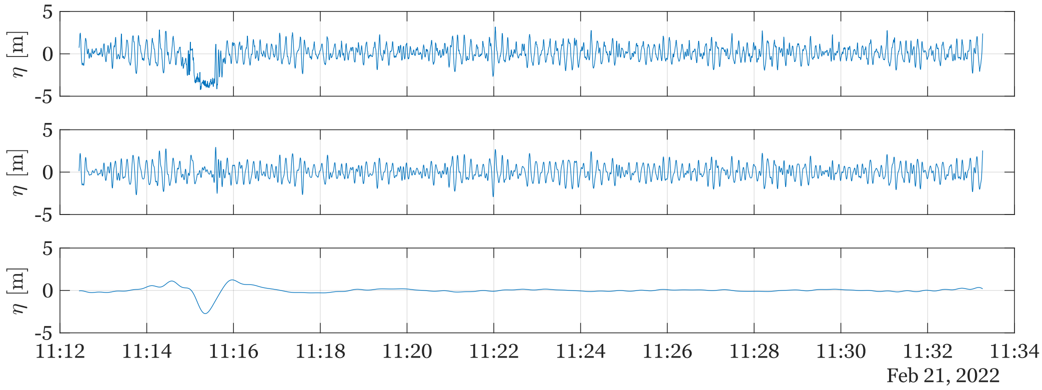

Figure A.3: Surface elevation signals η (frame 1) at 11:12-11:33 21 Feb 2022. Upper panel: AST signal. Middle panel: SS band-filtered AST signal. Lower panel: IG band-filtered AST signal.

B Cut-off Frequencies for IG Wave Height Calculation

The cut-off frequencies used in this study were determined as: 0.005Hz for the lowest IG frequency, 0.04Hz for the highest IG frequency, 0.14Hz for the highest swell frequency, and 0.33Hz for the highest SS frequency.

The above choices have been motivated in Chapter 4.3.2. A major concern was whether the 0.04 Hz cut-off is sufficiently low, so no swell energy can be included in the calculation of IG wave height. It was checked that during storms ($H_{SS} > 2.5m$), the 0.04 Hz cut-off does not lead to an overestimation of IG wave height. For example, see Figure B.2 (a). However, it may be invalid in calm or moderate wave conditions. Figure B.1 shows the pressure head derived variance density spectra throughout the two collection periods for frame 1. Continuous vertical lines through the frequency bins indicate high IG energy events that correspond to storm conditions. In contrast, some spectra included swell energy into IG frequencies, e.g., see the spectra circled by light blue ellipses in Figure B.1. Fortunately, these events only occurred occasionally, and the wave conditions were mostly calm. See Figure B.2 (b), for instance. To eliminate the influence of swell energy thoroughly, more sophisticated method may be need to determine the cut-off frequency, e.g., the empirical method of Oh et al. (2020). Since no significant error was introduced in the IG wave height calculation, the 0.04 Hz cut-off was applied for all the data.

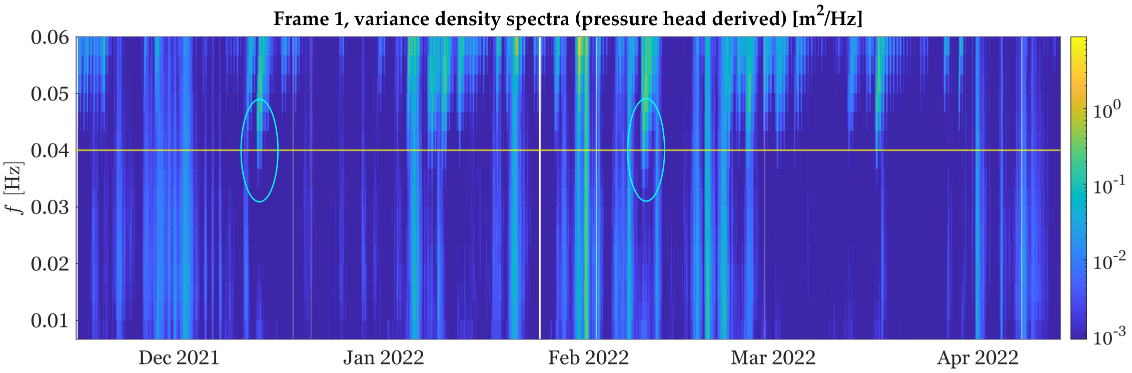

Figure B.1: Variance density spectra calculated from pressure head signals, the frequency range is 0.005-0.06 Hz. Data were collected from frame 1. The yellow line indicates the IG frequency cut-off, and the white vertical lines indicate no data available. Light blue ellipses highlight the spectra that include swell energy into IG frequencies.

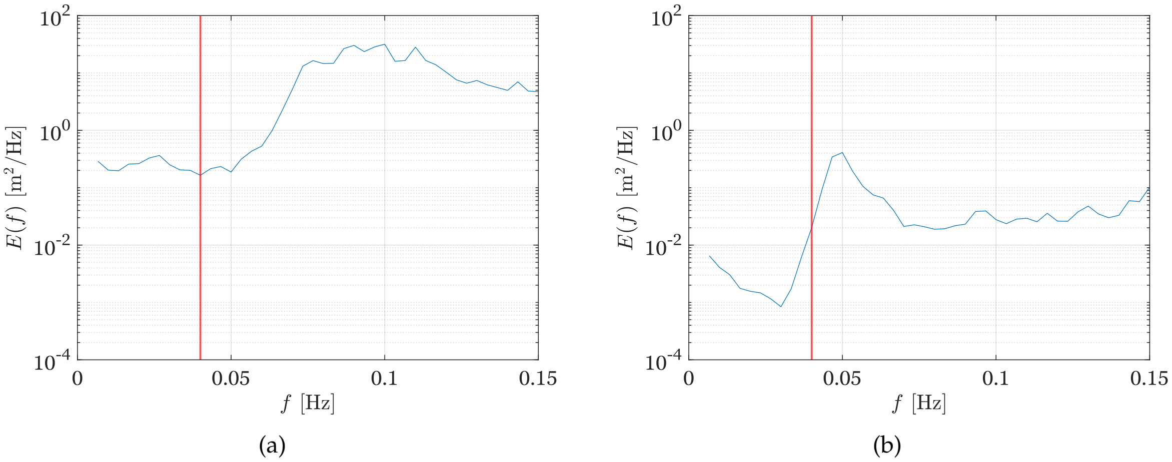

Figure B.2: Variance density spectra E, derived from pressure head signals. Red vertical lines indicate 0.04 Hz cut-off. (a): Spectrum at 13:00-14:00, 31 Jan 2022 ($H_{SS} = 5.04$ m, $H_{IG} = 0.37$ m). (b): Spectrum at 13:00-14:00, 9 Feb 2022 ($H_{SS} = 0.66$ m, $H_{IG} = 0.04$ m).

C Linear Correction Factor for Pressure Head Derived Spectrum

In this appendix, an illustration of the linear correction factor K_{lin} for frame 3 is given. Note the differences of the spectrum at high SS frequencies ($f > 0.2$ Hz).

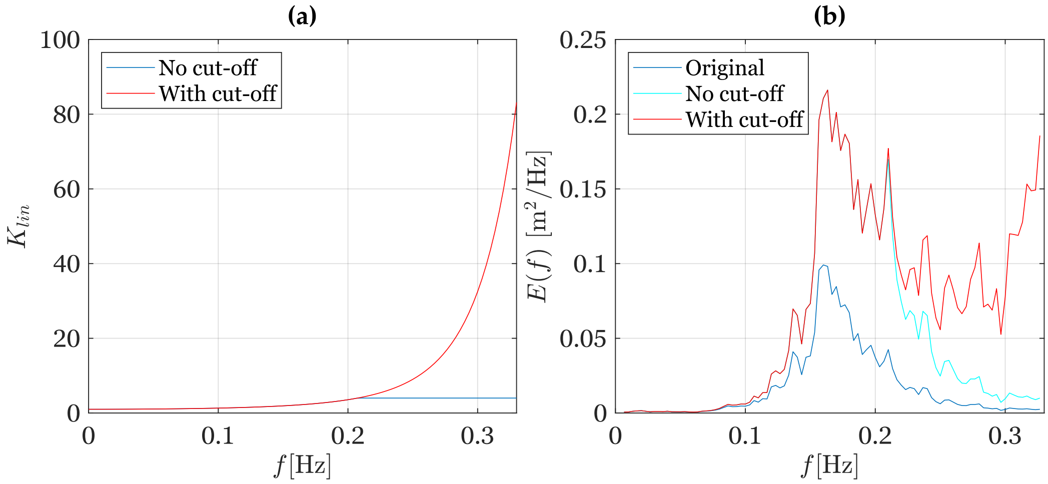

Figure C.1: Illustration of the linear correction factor K_{lin} and its influence on wave spectrum. (a): the linear correction factor K_{lin}, blue line: K_{lin} without a cut-off value of 4, red line: K_{lin} with a cut-off value of 4. (b): the corresponding energy density spectrum $E(f)$. Blue line: pressure head derived spectrum without linear correction, cyan line: spectrum after applying K_{lin} without a cut-off value of 4, red line: spectrum after applying K_{lin} with a cut-off value of 4. Time of observation: 00:00-01:00 30 Dec 2021. Mean water depth: 6.55 m.

D Dependencies of Bound and Free IG Waves

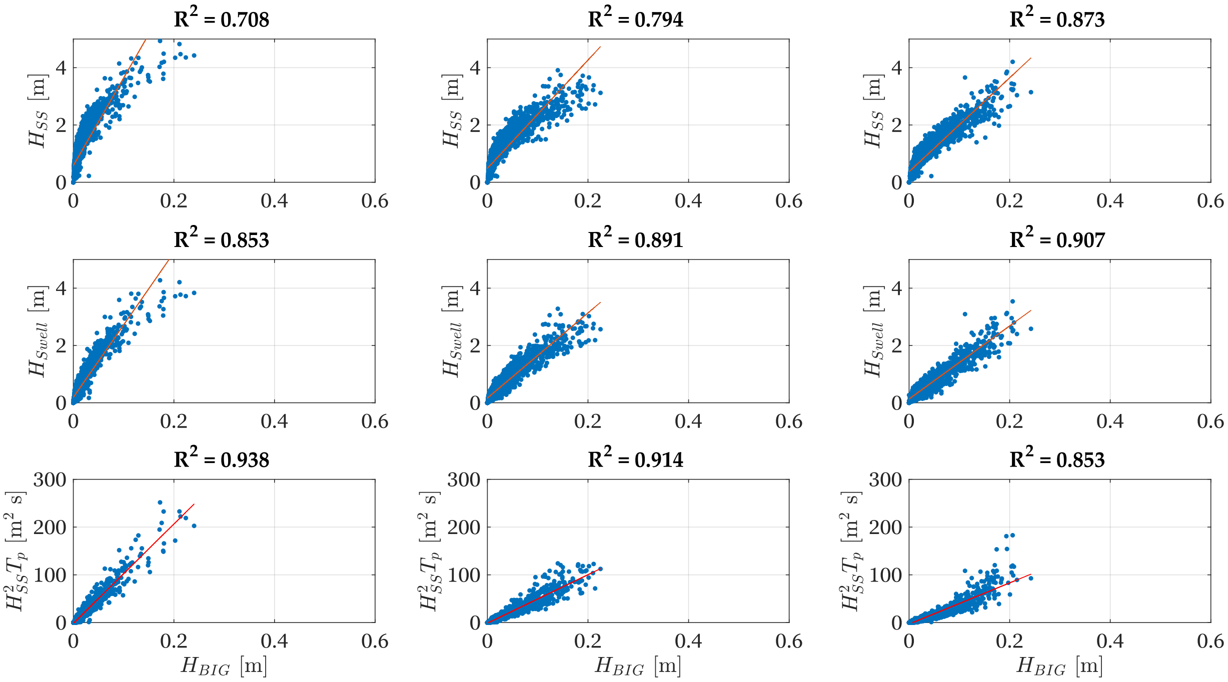

(a) Frame 1 (b) Frame 2 (c) Frame 3

Figure D.1: Bound IG wave height dependencies at (a) frame 1, (b) frame 2, and (c) frame 3. Upper panel: H_{SS} versus H_{BIG}. Middle panel: H_{Swell} versus H_{BIG}. Lower panel: $H_{SS}^2 T_p$ versus H_{BIG}. The red lines indicate best-fit linear regression lines, and the obtained correlation coefficients R^2 are given in the titles of each graph.

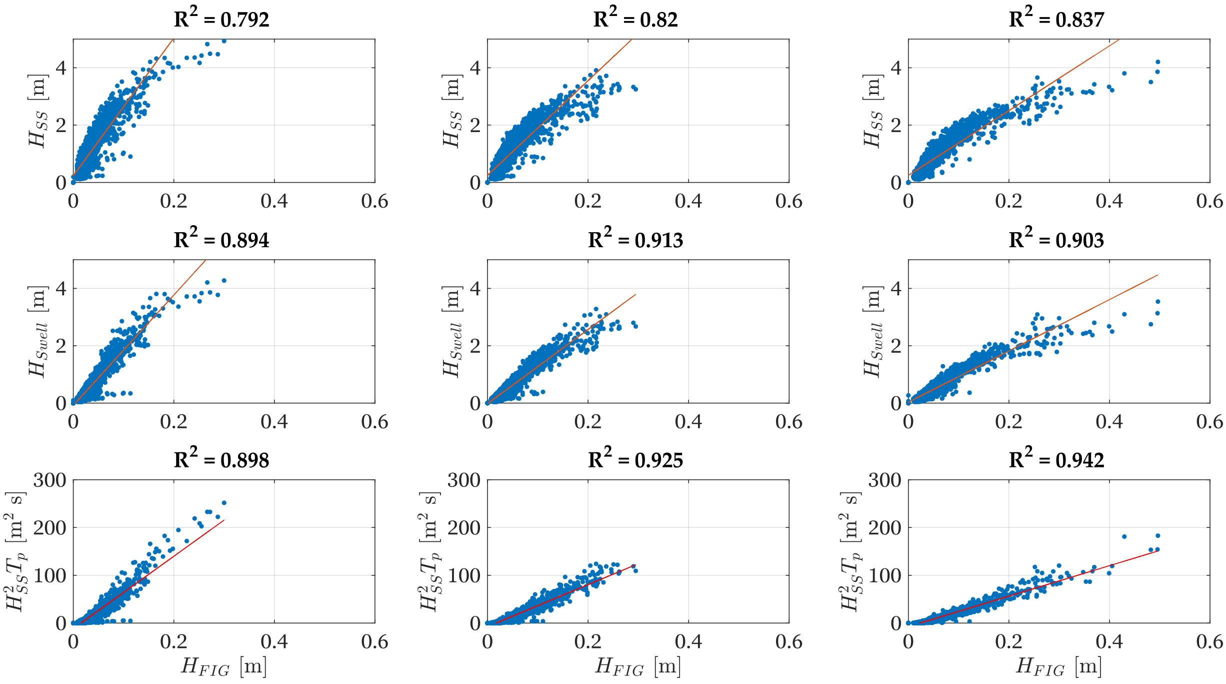

(a) Frame 1 (b) Frame 2 (c) Frame 3

Figure D.2: Free IG wave height dependencies at (a) frame 1, (b) frame 2, and (c) frame 3. Upper panel: H_{SS} versus H_{FIG}. Middle panel: H_{Swell} versus H_{FIG}. Lower panel: $H^2_{SS}T_p$ versus H_{FIG}. The red lines indicate best-fit linear regression lines, and the obtained correlation coefficients R^2 are given in the titles of each graph.

E Nonlinear Interaction Coefficients

In this appendix, some of the nonlinear interaction coefficients used in the directional spectra reconstruction method of Matsuba et al. (2022) are given. [1]

Defining $A(f)$ as an amplitude of the $f-$ Hz component of surface elevation, and $P(f)$ as an amplitude of the $f-$ Hz component of pressure head. The bound wave amplitude of the $f-$ Hz component $A_{bound}(f)$ $(f = f_2 - f_1)$ of surface elevation is given by:

$$A_{bound}(f) = A(f_1)A(f_2)\Omega_\eta. \tag{E.1}$$

The bound wave amplitude of the $f-$ Hz component $P_{bound}(f)$ $(f = f_2 - f_1)$ of surface elevation is given by:

$$P_{bound}(f) = P(f_1)P(f_2)\Omega_p. \tag{E.2}$$

The nonlinear interaction coefficients are used to obtain an amplitude of the bound components excited by f_1 -Hz and f_2 -Hz components. For the former case, the nonlinear interaction coefficient Ω_η can be written as:

$$\Omega_\eta = -\frac{gk_1k_2\cos\Delta\theta}{2\omega_1\omega_2} - \frac{\omega_1\omega_2}{2g} + \frac{(\omega_1^2+\omega_2^2)}{2g} + \Gamma_\eta, \tag{E.3}$$

and

$$\begin{aligned}\Gamma_\eta = &-\frac{g\omega}{\left[g\Delta k\tanh(\Delta kh) - \omega^2\right]\omega_1\omega_2}\left\{\omega\left[\left(\frac{\omega_1\omega_2}{g}\right)^2 + k_1k_2\cos\Delta\theta\right]\right.\\ &\left.-\frac{1}{2}\left[\frac{\omega_1k_2^2}{\cosh^2(k_2h)} - \frac{\omega_2k_1^2}{\cosh^2(k_1h)}\right]\right\}.\end{aligned} \tag{E.4}$$

where h is the mean water depth, k_i and ω_i represent the wave number and angular frequency of a wave component (f_i, θ_i), and $\omega_i = gk_i\tanh(k_ih)$. Δk is the difference wavenumber $\boldsymbol{k_2} - \boldsymbol{k_1}$,

---

[1] For more detailed information regarding the nonlinear interaction coefficients, please see the MATLAB codes available on `https://figshare.com/articles/dataset/Dataset_for_Reconstruction_of_Directional_Spectra_of_Infragravity_Waves/17157902`.

with $|\Delta k| = \sqrt{k_1^2 - k_2^2 - 2k_1k_2\cos\Delta\theta}$ and $\Delta\theta = \theta_2 - \theta_2$.

For the latter case, assuming the distance between the pressure sensor and the sea bed is zero, the nonlinear interaction coefficient Ω_p can be written as:

$$\Omega_p = -\frac{gk_1k_2\cos\Delta\theta}{2\omega_1\omega_2} + \Gamma_p, \tag{E.5}$$

and

$$\begin{aligned}\Gamma_p = -&\frac{g\omega\cosh(k_1h)\cosh(k_1h)}{\left[g\Delta k\tanh(\Delta kh) - \omega^2\right]\omega_1\omega_2\cosh(\Delta kh)}\left\{\omega\left[\left(\frac{\omega_1\omega_2}{g}\right)^2 + k_1k_2\cos\Delta\theta\right]\right.\\ &\left.-\frac{1}{2}\left[\frac{\omega_1k_2^2}{\cosh^2(k_2h)} - \frac{\omega_2k_1^2}{\cosh^2(k_1h)}\right]\right\}.\end{aligned} \tag{E.6}$$

Moreover, according to linear wave theory, if the pressure sensor locates on the sea bed, $A(f) = P(f)\cosh(kh)$. If $P(f)$ is derived from $A(f_1)$ and $A(f_2)$:

$$P_{bound}(f) = P(f_1)P(f_2)\Omega_{\eta p}, \tag{E.7}$$

the corresponding nonlinear interaction coefficient $\Omega_{\eta p}$ can be expressed as:

$$\Omega_{\eta p} = \frac{\Omega_p}{\cosh(k_1h)\cosh(k_2h)}. \tag{E.8}$$

F Transfer Functions

In this appendix, the transfer functions used for directional spectra reconstruction are summarized (see equations 2.23 and 2.24) [1].

F.1 First-order Transfer Functions

For velocity signal (x axis) u:

$$H^{(1)}_{u,f}(\theta) = \frac{\omega \cosh\left[k(z+l_n)\right]}{\sinh\left(kh\right)} \cos\left(\theta\right). \tag{F.1}$$

For velocity signal (y axis) v:

$$H^{(1)}_{v,f}(\theta) = \frac{\omega \cosh\left[k(z+l_n)\right]}{\sinh\left(kh\right)} \sin\left(\theta\right). \tag{F.2}$$

For pressure head signal p:

$$H^{(1)}_{p,f}(\theta) = \rho g \frac{\cosh\left(kz\right)}{\cosh\left(kh\right)}. \tag{F.3}$$

Note that z is the distacne between the instrument and the sea bed, h is the water depth, and l_n is the distance between the instrument and the velocity cells.

F.2 Second-order Transfer Functions

For velocity signal (x axis, East direction) u:

$$H^{(2)}_{u,f}(f_1, \theta_1, \theta_2) = \frac{g \Delta k \cosh[\Delta k\left(z_0 + l_n\right)]}{\omega \cosh(\Delta k h)} \frac{\Gamma}{\Omega} \cos\left(\theta_b\right). \tag{F.4}$$

---

[1] Expressions of the transfer functions for more types of wave-related signals can be found in the supporting information S1 of Matsuba et al. (2022)

For velocity signal (y axis, North direction) v:

$$H^{(2)}_{v,f}(f_1,\theta_1,\theta_2) = \frac{g\Delta k \cosh[\Delta k\,(z_0+l_n)]}{\omega\cosh(\Delta k h)}\,\frac{\Gamma}{\Omega}\sin(\theta_b)\,. \tag{F.5}$$

For pressure head signal p:

$$\begin{split} H^{(2)}_{p,f}(f_1,\theta_1,\theta_2) = \tfrac{\rho g}{\Omega}\Big\{-\tfrac{g k_1 k_2}{2\omega_1\omega_2\cosh(k_1 h)\cosh(k_2 h)}\,[\cos(\Delta\theta)\cosh[k_1\,(z_0+l_n)]\cosh[k_2\,(z_0+l_n)\,] \\ +\sinh[k_1\,(z_0+l_n)]\sinh[k_2\,(z_0+l_n)]] + \tfrac{\cosh[\Delta k(z_0+l_n)]}{\cosh(\Delta k h)}\Gamma\Big\}\,. \end{split} \tag{F.6}$$

θ_b is the direction of the second order (bound) wave.

Bibliography

Ardhuin, F., Rawat, A., and Aucan, J. (2014). A numerical model for free infragravity waves: Definition and validation at regional and global scales. *Ocean Modelling*, 77:20–32.

Baldock, T. (2012). Dissipation of incident forced long waves in the surf zone—implications for the concept of "bound" wave release at short wave breaking. *Coastal Engineering*, 60:276–285.

Baldock, T., Huntley, D., Bird, P., O'hare, T., and Bullock, G. (2000). Breakpoint generated surf beat induced by bichromatic wave groups. *Coastal Engineering*, 39(2-4):213–242.

Battjes, J., Bakkenes, H., Janssen, T., and van Dongeren, A. R. (2004). Shoaling of subharmonic gravity waves. *Journal of Geophysical Research: Oceans*, 109(C2).

Benoit, M., Frigaard, P., and Schäffer, H. (1997). Analyzing multidirectional wave spectra: a tentative classification of available methods. In *Proceedings of the 1997 IAHR conference, San Francisco*, pages 131–158.

Bertin, X., De Bakker, A., Van Dongeren, A., Coco, G., André, G., Ardhuin, F., Bonneton, P., Bouchette, F., Castelle, B., Crawford, W. C., et al. (2018). Infragravity waves: From driving mechanisms to impacts. *Earth-Science Reviews*, 177:774–799.

Capon, J., Greenfield, R. J., and Kolker, R. J. (1967). Multidimensional maximum-likelihood processing of a large aperture seismic array. *Proceedings of the IEEE*, 55(2):192–211.

Contardo, S., Lowe, R. J., Hansen, J. E., Rijnsdorp, D. P., Dufois, F., and Symonds, G. (2021). Free and forced components of shoaling long waves in the absence of short-wave breaking. *Journal of Physical Oceanography*, 51(5):1465–1487.

Contardo, S. and Symonds, G. (2013). Infragravity response to variable wave forcing in the nearshore. *Journal of Geophysical Research: Oceans*, 118(12):7095–7106.

De Bakker, A. (2012). Infragravity waves-propagation, dissipation and sediment transport in the inner surf zone of a low sloping beach. Master's thesis, Utrecht University.

De Bakker, A., Herbers, T., Smit, P., Tissier, M., and Ruessink, B. (2015). Nonlinear infragravity–wave interactions on a gently sloping laboratory beach. *Journal of Physical Oceanography*, 45(2):589–605.

De Bakker, A., Tissier, M., Marieu, V., Sénéchal, N., Ruju, A., Lara, J., and Ruessink, B. (2013). Infragravity wave propagation and dissipation on a low-sloping laboratory beach. In *Proceedings of the Conference on Coastal Dynamics*, pages 443–452.

De Bakker, A., Tissier, M., and Ruessink, B. (2014). Shoreline dissipation of infragravity waves. *Continental Shelf Research*, 72:73–82.

De Bakker, A., Tissier, M., and Ruessink, B. (2016). Beach steepness effects on nonlinear infragravity-wave interactions: A numerical study. *Journal of Geophysical Research: Oceans*, 121(1):554–570.

De Schipper, M. A., de Vries, S., Ruessink, G., de Zeeuw, R. C., Rutten, J., van Gelder-Maas, C., and Stive, M. J. (2016). Initial spreading of a mega feeder nourishment: Observations of the sand engine pilot project. *Coastal Engineering*, 111:23–38.

de Wit, F., Tissier, M., and Reniers, A. (2020). The relationship between sea-swell bound wave height and wave shape. *Journal of Marine Science and Engineering*, 8(9):643.

Dong, G., Ma, X., Perlin, M., Ma, Y., Yu, B., and Wang, G. (2009). Experimental study of long wave generation on sloping bottoms. *Coastal Engineering*, 56(1):82–89.

Eckart, C. (1951). Surface waves on water of variable depth. *Wave report nr. 100, SIO reference 51-12*.

Elgar, S. and Guza, R. (1985). Observations of bispectra of shoaling surface gravity waves. *Journal of Fluid Mechanics*, 161:425–448.

Elgar, S., Herbers, T., Okihiro, M., Oltman-Shay, J., and Guza, R. (1992). Observations of infragravity waves. *Journal of Geophysical Research: Oceans*, 97(C10):15573–15577.

Elgar, S., Herbers, T. H. C., and Guza, R. T. (1994). Reflection of ocean surface gravity waves from a natural beach. *Journal of Physical Oceanography*, 24(7):1503 – 1511.

Fiedler, J. W., Brodie, K. L., McNinch, J. E., and Guza, R. T. (2015). Observations of runup and energy flux on a low-slope beach with high-energy, long-period ocean swell. *Geophysical Research Letters*, 42(22):9933–9941.

Fiedler, J. W., Smit, P. B., Brodie, K. L., McNinch, J., and Guza, R. T. (2018). Numerical modeling of wave runup on steep and mildly sloping natural beaches. *Coastal Engineering*, 131:106–113.

Google (2022). Google Earth image. Retrieved March 22, 2022, from `https://earth.google.com`.

Goring, D. G. and Nikora, V. I. (2002). Despiking acoustic doppler velocimeter data. *Journal of hydraulic engineering*, 128(1):117–126.

Guza, R. and Feddersen, F. (2012). Effect of wave frequency and directional spread on shoreline runup. *Geophysical Research Letters*, 39(11).

Hashimoto, N. (1997). Analysis of the directional wave spectrum from field data. In *Advances in coastal and ocean engineering*, pages 103–143. World Scientific.

Hashimoto, N. and Kobune, K. (1988). Estimation of directional spectrum through a bayesian approach. *Coastal Engineering in Japan*, 31(2):183–198.

Hasselmann, K. (1962). On the non-linear energy transfer in a gravity-wave spectrum part 1. general theory. *Journal of Fluid Mechanics*, 12(4):481–500.

Henderson, S. M. and Bowen, A. (2002). Observations of surf beat forcing and dissipation. *Journal of Geophysical Research: Oceans*, 107(C11):14–1.

Herbers, T., Elgar, S., and Guza, R. (1999). Directional spreading of waves in the nearshore. *Journal of Geophysical Research: Oceans*, 104(C4):7683–7693.

Herbers, T. H. C., Elgar, S., and Guza, R. T. (1994). Infragravity-frequency (0.005–0.05 hz) motions on the shelf. part i: Forced waves. *Journal of Physical Oceanography*, 24(5):917 – 927.

Herbers, T. H. C., Elgar, S., Guza, R. T., and O'Reilly, W. C. (1995). Infragravity-frequency (0.005–0.05 hz) motions on the shelf. part ii: Free waves. *Journal of Physical Oceanography*, 25(6):1063 – 1079.

Hersbach, H., Bell, B., Berrisford, P., Hirahara, S., Horányi, A., Muñoz-Sabater, J., Nicolas, J., Peubey, C., Radu, R., Schepers, D., et al. (2020). The era5 global reanalysis. *Quarterly Journal of the Royal Meteorological Society*, 146(730):1999–2049.

Inch, K., Davidson, M., Masselink, G., and Russell, P. (2017). Observations of nearshore infragravity wave dynamics under high energy swell and wind-wave conditions. *Continental Shelf Research*, 138:19–31.

Janssen, T., Battjes, J., and Van Dongeren, A. (2003). Long waves induced by short-wave groups over a sloping bottom. *Journal of Geophysical Research: Oceans*, 108(C8).

Johnson, D. (2002). Diwasp, a directional wave spectra toolbox for matlab®: User manual. *Center for Water Research, University of Western Australia*, pages 1–23.

Kim, Y. C. and Powers, E. J. (1979). Digital bispectral analysis and its applications to nonlinear wave interactions. *IEEE transactions on plasma science*, 7(2):120–131.

KNMI (2022a). Koninklijk Nederlands Meteorologisch Instituut, daily weather data in the Netherlands. `https://www.knmi.nl/nederland-nu/klimatologie/daggegevens`.

KNMI (2022b). Koninklijk Nederlands Meteorologisch Instituut, explanation about naming storms. `https://www.knmi.nl/kennis-en-datacentrum/uitleg/naamgeving-van-stormen`.

Kuik, A. J., van Vledder, G. P., and Holthuijsen, L. H. (1988). A method for the routine analysis of pitch-and-roll buoy wave data. *Journal of Physical Oceanography*, 18(7):1020 – 1034.

Lashley, C. H., Bertin, X., Roelvink, D., and Arnaud, G. (2019). Contribution of infragravity waves to run-up and overwash in the pertuis breton embayment (france). *Journal of Marine Science and Engineering*, 7(7).

Latheef, M., Swan, C., and Spinneken, J. (2017). A laboratory study of nonlinear changes in the directionality of extreme seas. *Proceedings of the Royal Society A: Mathematical, Physical and Engineering Sciences*, 473(2199):20160290.

Lin, Z., Adcock, T., and McAllister, M. (2021). Estimating ocean wave directional spreading using wave following buoys: a comparison of experimental buoy and gauge data. *Journal of Ocean Engineering and Marine Energy*.

Longuet-Higgins, M. S. and Stewart, R. (1962). Radiation stress and mass transport in gravity waves, with application to 'surf beats'. *Journal of Fluid Mechanics*, 13(4):481–504.

Lygre, A. and Krogstad, H. E. (1986). Maximum entropy estimation of the directional distribution in ocean wave spectra. *Journal of Physical Oceanography*, 16(12):2052–2060.

Mahmoudof, S. M., Azizpour, J., and Eyhavand-Koohzadi, A. (2021). Observation of infragravity wave processes near the coastal cliffs of Chabahar (Gulf of Oman). *Estuarine, Coastal and Shelf Science*, 251:107226.

Mahmoudof, S. M. and Siadatmousavi, S. M. (2020). Bound infragravity wave observations at the nowshahr beaches, southern caspian sea. *Applied Ocean Research*, 98:102122.

Masselink, G. (1995). Group bound long waves as a source of infragravity energy in the surf zone. *Continental Shelf Research*, 15(13):1525–1547.

Matsuba, Y., Roelvink, D., Reniers, A. J. H. M., Rijnsdorp, D. P., and Shimozono, T. (2022). Reconstruction of directional spectra of infragravity waves. *Journal of Geophysical Research: Oceans*, 127(7):e2021JC018273.

Matsuba, Y., Shimozono, T., and Sato, S. (2020). Wave-breaking modulation by infragravity waves during an extreme typhoon. *PloS one*, 15(4):e0231242.

Mei, C. C. and Benmoussa, C. (1984). Long waves induced by short-wave groups over an uneven bottom. *Journal of Fluid Mechanics*, 139:219–235.

Mendes, D., Pires-Silva, A. A., Pinto, J. P., and Fortunato, A. B. (2020). Bound and free infragravity wave energy over a bar. *Ocean Engineering*, 201:107128.

Miche, M. (1951). Le pouvoir réfléchissant des ouvrages maritimes exposés à l'action de la houle. *Annales de Ponts et Chaussées, 121 (285-319).*

Molin, B. (1982). On the generation of long-period second-order free-waves due to changes in the bottom profile. *Papers of Ship Research Institute (Tokyo).*

Mori, N., Suzuki, T., and Kakuno, S. (2007). Noise of acoustic doppler velocimeter data in bubbly flows. *Journal of engineering mechanics*, 133(1):122–125.

Munk, W. (1949). Surf beats. *EOS, Transactions American Geophysical Union*, 30(6):849–854.

Nortek (2018). *The comprehensive manual for Velocimeters*. Nortek AS.

Nortek (2019). *Ocean Contour software users guide*. Ocean Illumination Ltd.

Nortek (2021). *The comprehensive manual for ADCPs*. Nortek AS.

Nortek (2022a). *Principles of operation*. Nortek AS.

Nortek (2022b). *Signature operations*. Nortek AS.

Oh, J.-E., Jeong, W.-M., Chang, Y. S., and Oh, S.-H. (2020). On the separation period discriminating gravity and infragravity waves off gyeongpo beach, korea. *Journal of Marine Science and Engineering*, 8(3):167.

Pawka, S. S. (1983). Island shadows in wave directional spectra. *Journal of Geophysical Research*, 88(C4):2579.

Pomeroy, A., Lowe, R., Symonds, G., Van Dongeren, A., and Moore, C. (2012). The dynamics of infragravity wave transformation over a fringing reef. *Journal of Geophysical Research: Oceans*, 117(C11).

Rawat, A., Ardhuin, F., Ballu, V., Crawford, W., Corela, C., and Aucan, J. (2014). Infragravity waves across the oceans. *Geophysical Research Letters*, 41(22):7957–7963.

Reniers, A., Groenewegen, M., Ewans, K., Masterton, S., Stelling, G., and Meek, J. (2010). Estimation of infragravity waves at intermediate water depth. *Coastal Engineering*, 57(1):52–61.

Reniers, A. J., Naporowski, R., Tissier, M. F., de Schipper, M. A., Akrish, G., and Rijnsdorp, D. P. (2021). North sea infragravity wave observations. *Journal of Marine Science and Engineering*, 9(2):141.

Rijnsdorp, D. P., Reniers, A. J., and Zijlema, M. (2021). Free infragravity waves in the north sea. *Journal of Geophysical Research: Oceans*, 126(8):e2021JC017368.

Ruessink, B. (1998a). Bound and free infragravity waves in the nearshore zone under breaking and nonbreaking conditions. *Journal of Geophysical Research: Oceans*, 103(C6):12795–12805.

Ruessink, B. (1998b). The temporal and spatial variability of infragravity energy in a barred nearshore zone. *Continental Shelf Research*, 18(6):585–605.

Ruju, A., Lara, J. L., and Losada, I. J. (2012). Radiation stress and low-frequency energy balance within the surf zone: A numerical approach. *Coastal engineering*, 68:44–55.

Rutten, J., Dubarbier, B., Price, T., Castelle, B., and Ruessink, G. (2017). Crescentic bar patterns along curved coasts: Observations and modelling. *Proceedings of Coastal Dynamics 2017*, pages 1832–1842.

Sand, S. E. (1982). Long waves in directional seas. *Coastal Engineering*, 6:195–208.

Symonds, G., Huntley, D. A., and Bowen, A. J. (1982). Two-dimensional surf beat: Long wave generation by a time-varying breakpoint. *Journal of Geophysical Research: Oceans*, 87(C1):492–498.

TRDI (2007). *WorkHorse Technical Manual*. Teledyne RD Instruments.

Van Dongeren, A., Battjes, J., Janssen, T., Van Noorloos, J., Steenhauer, K., Steenbergen, G., and Reniers, A. (2007). Shoaling and shoreline dissipation of low-frequency waves. *Journal of Geophysical Research: Oceans*, 112(C2).

Van Dongeren, A., De Jong, M., Van der Lem, C., Van Deyzen, A., and Den Bieman, J. (2016). Review of long wave dynamics over reefs and into ports with implication for port operations. *Journal of Marine Science and Engineering*, 4(1):12.

Van Dongeren, A., Reniers, A., Battjes, J., and Svendsen, I. (2003). Numerical modeling of infragravity wave response during delilah. *Journal of Geophysical Research: Oceans*, 108(C9).

Van Enckevort, I. and Reincke, E. (1996). *Longshore currents in the intertidal zone of Terschelling*. Utrechts Univ., Fac. of Geographical Sciences, Department of Physical Geography.

van Essen, S., van der Hout, A., Huijsmans, R., and Waals, O. (2013). Evaluation of directional analysis methods for low-frequency waves to predict lngc motion response in nearshore areas. In *International Conference on Offshore Mechanics and Arctic Engineering*, volume 55317, page V001T01A015. American Society of Mechanical Engineers.

Vrećica, T., Soffer, R., and Toledo, Y. (2019). Infragravity wave generation by wind gusts. *Geophysical Research Letters*, 46(16):9728–9738.

Waals, O. J. (2009). The effect of wave directionality on low frequency motions and mooring forces. In *International Conference on Offshore Mechanics and Arctic Engineering*, volume 43444, pages 289–298.

Webb, S. C., Zhang, X., and Crawford, W. (1991). Infragravity waves in the deep ocean. *Journal of Geophysical Research: Oceans*, 96(C2):2723–2736.

Wijnberg, K. M. (2002). Environmental controls on decadal morphologic behaviour of the holland coast. *Marine Geology*, 189(3-4):227–247.

Zheng, Z., Ma, X., Ma, Y., Huang, X., and Dong, G. (2021). Modeling of coastal infragravity waves using the spectral model WAVEWATCH III. *Coastal Engineering*, 170:104016.